Surfaces with Patterned Wettability: Design and Applications

by

Sai Pradeep Reddy Kobaku

A dissertation submitted in partial fulfillment
of the requirements for the degree of
Doctor of Philosophy
(Macromolecular Science and Engineering)
in the University of Michigan
2015

Doctoral Committee:

Associate Professor Anish Tuteja, Chair
Associate Professor Nicholas Kotov
Associate Professor Joerg Lahann
Associate Professor Pramod Sangi Reddy

© Sai Pradeep Reddy Kobaku

2015

To My Parents

ACKNOWLEDGEMENTS

The work in this dissertation wouldn't have been possible without the help and support of a number of people. I have been very fortunate to have Professor Anish Tuteja as my research advisor. I am grateful for his invaluable guidance and secured funding to make this work possible. He has taught me to be an independent thinker and has given me the freedom to explore, diversify and develop my own individuality during the course of this work. I am also very thankful to him for taking out time to discuss my career goals time to time and appropriately advising me at various stages. I will always remember the discussions and his valuable suggestions regarding career pathways and life in general.

I also would like to thank other members of my PhD committee: Prof. Nicholas Kotov, Prof. Joerg Lahann and Prof. Pramod Reddy. I am honored by the opportunity to conduct my research under the guidance of such brilliant people. Prof. Kotov's comments and suggestions on my work, particularly on particle fabrication methodology has been of a great help. Prof. Lahann's expertise made him a valuable resource for my PhD work, especially for the work on multiphasic particles. His comments during prelims and data meeting presentations have helped me improve my thesis. Also, from the collaboration projects with Prof. Reddy's group, I have learnt a lot of new concepts particularly in the field of heat transfer. I also would like to thank Prof. Reddy for the discussion regarding

my future career opportunities. I also would like to thank Prof. Richard Robertson, Prof. Amit Misra and Prof. Richard Laine for their helpful career advice and suggestions in general.

I would especially like to thank each and every one of my labmates for their tremendous help, and more importantly for their friendships. I would like to first thank Dr. Arun Kota, currently an assistant professor at Colorado State University. He has been of a great mentor and friend to me, and I cannot thank him enough for all the help and guidance he has given me both at work as well as outside. I also would like to thank Dr. Duck Hyun Lee for being a resourceful mentor in nanofabrication techniques and a great friend all through my journey as a PhD student. I also cherished the company of my fellow graduate students Gibum Kwon and Kevin Golovin. I would definitely miss our conference trips. I also thank all my lab mates Raghu, Chao, Philip, Matt, Ethan, Sarah, Ahmet, Inseong, Catherine for all their help with my research and for making our lab a comfortable and joyful place to work.

The administrative staff connected to Macromolecular Science and Engineering Program, Materials Science and Engineering Department and Biointerfaces Institute have ensured that I was never worried about anything not connected to research. I would like to especially thank Nonna Hamilton and Lisa Moran for going far above and beyond their office duties to help me whenever I needed them.

Coming to my friends and family, I would like to first thank my fiancée, Deeksha. My journey with her started about the same time I started my PhD. Since then, she has been the central part of almost every memorable event and every travel within the US. I can’t thank her enough for all her love and support and for making my PhD years go so

easy. I also would like to thank my friends and colleagues that shared many good times during my stay at Ann Arbor: GK, Raghu, Vaibhav, Adi, Apoorv, Viswanath, Sumanth, Sanket, Perwez, Ravi, Ashwin, Priyanka, Kunal and many others. I also thank many other high school and undergraduate friends for staying connected with me.

Finally and most importantly, this thesis would not have been possible without the love and support of my family. First, I would like to thank my parents, Subhashini and Poli Reddy, to whom this thesis is dedicated, for every sacrifice they have done for my education and for all their prayers and unconditional love. I also thank my younger brother, Sandeep Kobaku, for always making himself available whenever I need him and for his admiration and belief in whatever I do. I also would like to thank my extended family members Bhagawathi, Divya, Divija, Srinivasulu Reddy and many others for their unconditional support and love.

TABLE OF CONTENTS

LIST OF FIGURES

Figure

LIST OF TABLES

Table

ABSTRACT

Surfaces with patterned wettability have well-defined domains containing both wettable and non-wettable regions. One of the key features of the surfaces with patterned wettability is their ability to localize wetting of liquids preferentially within the patterned wettable regions. This ability of the patterned surfaces has been widely explored as a simple route to pattern both liquids, as well as, solids for various applications such as microfluidics, electronic and optical devices, surfaces with enhanced heat transfer properties, etc. However, most of the patterned surfaces exhibit wettability contrast only with high surface tension liquids such as water, thereby limiting the applications of the patterned surfaces to only aqueous systems.

Herein, we utilize the design principles of superomniphobicity (repellency towards all liquids) to develop the first-ever patterned superomniphobic-superomniphilic surfaces that exhibit extremely wettability contrast with both high and low surface tension liquids. Utilizing these patterned surfaces, we demonstrate site-selective self-assembly of various liquids including: oils, alcohols, polymer solutions and solid dispersions. We also demonstrate site-selective condensation and boiling with low surface tension liquids, which is crucial when designing surfaces with significantly enhanced, phase-change, heat-transfer properties. We have further utilized surfaces with

patterned wettability as templates for fabricating monodisperse, multi-phasic micro- and nano-particles. The developed technique termed WETS (Wettability Engendered Templated Self-assembly) provides us with an unprecedented ability to manufacture multi-phasic particles, on a large-scale, with precise control over the size (down to 25 nm), shape, chemistry and surface charge of the particles. We further demonstrate the utility of the WETS technique in developing amphiphilic building blocks for self-assembly and multi-functional cargo carriers. Finally, we have also studied stimuli-responsive shape reconfigurations of the multi-phasic WETS particles. Overall, this dissertation puts forward design principles for developing surfaces with patterned wettability that are universal to almost all liquids, thus enabling novel applications for the patterned surfaces, such as the WETS technique reported here.

CHAPTER 1

Introduction

1.1. Introductory Remarks

Surfaces with patterned wettability have well-defined domains of both wettable and non-wettable regions. One of the key features of surfaces with patterned wettability is their ability to localize liquids preferentially within the patterned wettable regions[1-8]. Since the first observation of this phenomenon, researchers have utilized surfaces with patterned wettability for various applications including microchannels and microreactors[3-8], well-defined arrays of polymer films and particles for electronic and optical applications[9-15], patterned arrays of DNA, proteins and cells for biological applications,[16] and more recently as interfaces with enhanced heat transfer properties[17-22].

This chapter serves to introduce some important concepts of the wetting behavior of liquids on patterned surfaces and background information on the applications of the patterned surfaces. In addition to this background, each chapter has its own introduction that will provide a more detailed background to the specific topics discussed.

1.2. Fundamentals of wetting

When a liquid droplet comes in contact with a solid surface, it can either wet the surface completely, or partially, making a finite contact angle with the surface. The contact angle that liquid makes on a surface is a convenient measure of wettability on a solid surface. Based on the value of the contact angle θ of a water droplet, surfaces can be classified as superhydrophilic when $\theta \approx 0^{o}$, hydrophilic when $\theta < 90°$, hydrophobic when $\theta > 90°$ and superhydrophobic when $\theta > 150°$. Similarly, based on the contact angle of an oil droplet, surfaces can be classified as superoleophilic when $\theta \approx 0^{o}$, oleophilic when $\theta < 90°$, oleophobic when $\theta > 90°$ and superoleophobic when $\theta > 150°$. Surfaces with $\theta > 150°$, typically have low adhesion with the liquid droplet owing to very low solid-liquid contact area. Thus, to develop surfaces that are extremely repellent to liquids, it is desired to have contact angles $\theta > 150°$ with liquids.

The equilibrium contact angle (θ_E) on a smooth homogenous surface, is determined by the balance between the solid-vapor (γ_{SV} or the surface energy), solid-liquid (γ_{SL}) and liquid-vapor (γ_{LV} or the surface tension) interfacial tensions acting at the three-phase contact line, and is given by the Young's relation[23]:

(Equation 1.1) $\cos\theta_E = (\gamma_{SV} - \gamma_{SL})/\gamma_{LV}$

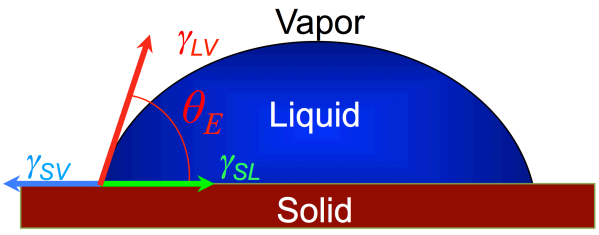

Figure 1.1 A liquid droplet on a smooth solid surface.

From the Young's relation, we can see that surfaces with low solid surface energy

(γ_{SV}) can yield high contact angles[24]. However, based on the literature so far, even on surfaces with the lowest solid surface energy reported to date[25, 26] ($\gamma_{SV} \sim$ 6 mN/m), the water contact angle was not larger than $\sim 125°$. Thus, it is not possible to develop super-repellent surfaces ($\theta > 150°$) on smooth solid surfaces. However it has been shown that super-repellent properties ($\theta > 150°$) are possible on textured surfaces, as discussed below.

1.3. Wetting on textured surfaces

When a liquid droplet comes in contact with a textured surface, it adopts either a Cassie-Baxter[27] state, which supports a composite solid-liquid-air interface or a fully wetted Wenzel[28] state (Figure 1.2). The apparent contact angle that a liquid droplet makes on the textured surface can be very different from the equilibrium contact angle (from Young's equation 1.1) for the liquid on the solid surface. In the case of the Cassie-Baxter state, as shown in Figure 1.2a, the liquid droplet locally makes the equilibrium contact angle with the surface and does not fully penetrate the surface. Consequently, air pockets remains trapped at the interface forming a solid-liquid-air composite interface. The apparent contact angle (θ^*) in this state is given by Cassie-Baxter relation[27]:

(Equation 1.2) $\cos\theta^* = f_{SL}\cos\theta_E + f_{LV}\cos\pi = f_{SL}\cos\theta_E - f_{LV}$

Here f_{SL} and f_{LV} are the areal fractions of the solid-liquid interface and the liquid-air interface per unit projected area of the composite interface. From the Cassie-Baxter relationship, apparent contact angle can be thought of as a weighted average between the values of the equilibrium contact angle of the liquid on the solid (θ_E) and on the air pocket (i.e., π). Thus, a liquid droplet that adopts the composite Cassie-Baxter state on a textured surface can have apparent contact angles (θ^*) much higher than the equilibrium

contact angle (θ_E) for the liquid on a smooth solid surface.

On the other hand, if the liquid cannot reach its equilibrium contact angle without penetrating fully into the pores of the textured surface, then the liquid droplet wets the surface completely and the apparent contact angle in this state is given by Wenzel relation[28]:

(Equation 1.3) $\cos\theta^* = r\cos\theta_E$

Here r is the surface roughness defined as the ratio of actual surface area to the project area. By comparing equation 1.3 and 1.4, we can see that Wenzel relation is a special case of Cassie-Baxter relation for $f_{LV} = 0$ ($f_{SL} = r$).

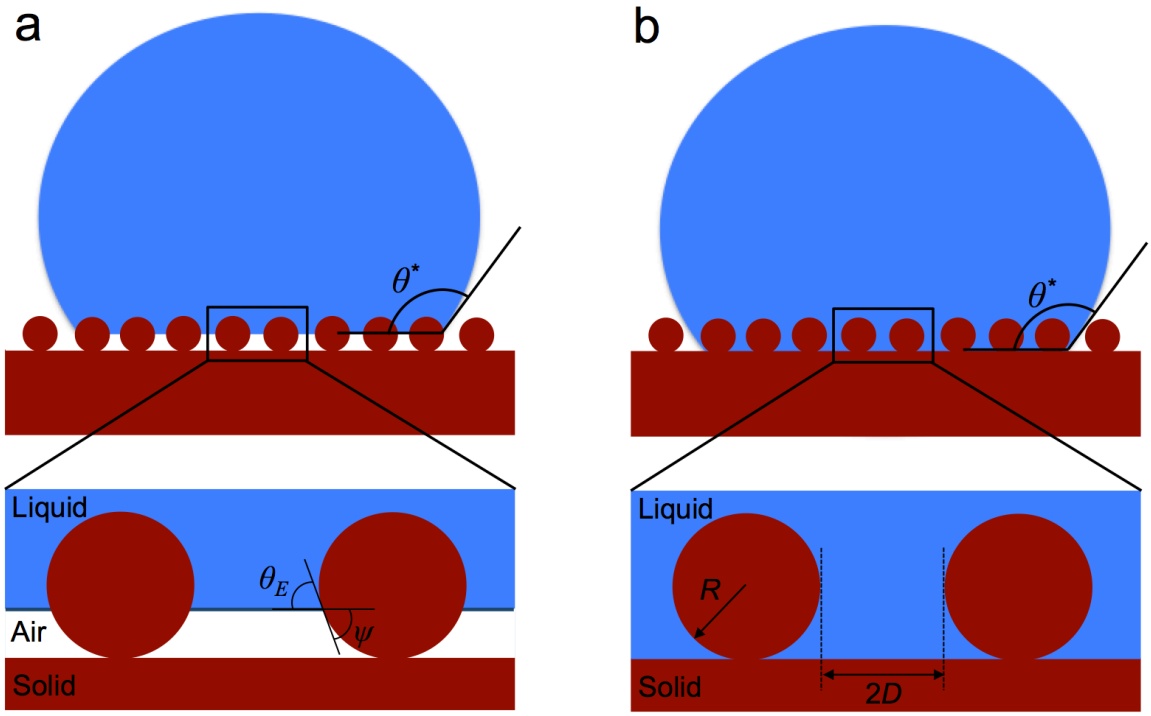

Figure 1.2 Liquid droplets on textured surfaces[29]. (a) A schematic illustration of a liquid droplet in the Cassie-Baxter state forming a composite solid-liquid-air interface. (b) A schematic illustration of a liquid droplet in the 'fully-wetted' Wenzel state.

For liquids with $\theta_E > 90°$ on surfaces with $r >> 1$, equation 1.4 predicts that very high apparent contact angles are possible in the Wenzel state. However, the liquid

droplets in the Wenzel state are strongly adhered to the solid surface owing to the high fraction of solid-liquid interfacial area (f_{SL}).

On the other hand, the liquid droplets in the composite Cassie-Baxter state can have a very low fraction of solid-liquid contact area leading to weak adhesion between the liquid droplet and the solid surface. The adhesion between the solid surface and liquid droplets is characterized by contact angle hysteresis ($\Delta\theta^*$), defined as the difference between the measured values of the apparent contact angles as the liquid droplets advances or recedes ($\Delta\theta^* = \theta_A^* - \theta_R^*$) on the solid surface. Typically, the hysteresis $\Delta\theta^*$ in the Wenzel state is significantly higher than the hysteresis in the Cassie-Baxter state.

Further in the case of liquids with $\theta_E < 90°$ (different low surface tension liquids), we can see from equations 1.2 and 1.3 that high apparent contact angles ($\theta^* >> \theta_E$) are possible only in Cassie-Baxter state. So, the composite Cassie-Baxter state is the preferred configuration for developing super-repellent surfaces that can repel both high and low surface tension liquids.

1.4 Design of superomniphobic surfaces

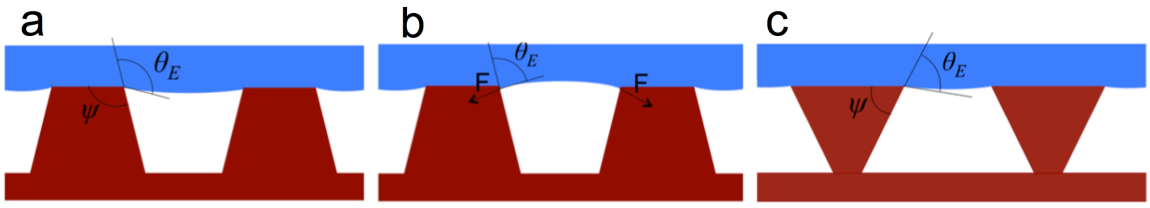

Figure 1.3 The critical role of re-entrant texture[29]. A schematic illustration of a textured surface with $\psi > 90°$ showing a) a liquid droplet with $\theta_E > 90°$ in the Cassie-Baxter state and b) a liquid droplet with $\theta_E < 90°$, here the capillary forces (indicated as F) cannot oppose the pressure exerted on the liquid-vapor interface and thus leading to fully wetted wenzel state. c) A schematic illustration of a re-entrant textured surface ($\psi < 90°$) showing a liquid droplet with $\theta_E < 90°$ in the Cassie-Baxter state.

Superomniphobic surfaces refer to surfaces that display very high contact angles and very low contact angle hysteresis with both high and low surface tension liquids. In other words superomniphobic surfaces display both superhydrophobicity and superoleophobicity.[29-33] From the discussion in last section, it can be seen that superomniphobic surfaces are possible only on textured surfaces that form a stable composite interface (Cassie-Baxter state) with both high and low surface tension liquids. However not all types of textured surfaces can yield a stable composite interface, particularly for low surface tension liquids with $\theta_E < 90°$. To illustrate this, let us consider two different textured surfaces (shown in figures 1.3a and 1.3c), one with texture angle $\psi > 90°$ and another with texture angle $\psi < 90°$. In both cases, any liquid droplet forming a composite interface with the textured surface displays an equilibrium contact angle (θ_E) locally at the solid-liquid-air interface. A stable composite Cassie-Baxter state is possible on the textured surfaces, only when the liquid equilibrium contact angle $\theta_E \geq \psi$. This is because when $\theta_E < \psi$, the net traction on the liquid-vapor interface (below the liquid droplet) is pointed downwards due to the surface tension forces, which causes the liquid droplet to penetrate the pores and wet the surface completely. Thus, the textured surface shown in Figure 1.3a with $\psi > 90°$ can support a stable composite interface with high surface tension liquids but not with low surface tension liquids. On the other hand, the textured surface shown in Figure 1.3b can form a stable composite interface with both high and low surface tension liquids. Such textures with $\psi < 90°$ are called re-entrant textures, i.e textures that bend back on itself[26, 30, 34, 35]. Therefore, re-entrant textured surfaces that enable $\theta_E \geq \psi$ for both high and low surface tension liquids can lead to superomniphobicity.

1.5. Design parameters for patterned superomniphobic-superomniphilic surfaces

For the design of the patterned superomniphobic-superomniphilic surfaces, the superomniphobic regions should support a sable composite interface with almost all liquids, while the superomniphilic regions should form a completely wetted, Wenzel state with all liquids. In this section, we discuss design parameters that correspond to the transition between the Cassie-Baxter state and Wenzel state.

As discussed in section 1.4, reentrant texture where $\theta_E \geq \psi$ is a necessary condition for formation of a stable composite interface with low surface tension liquids. However, it is not a sufficient condition for superomniphobicity[36-38]. In addition to possessing re-entrant texture, a superomniphobic surface should possess a sufficiently high breakthrough pressure $P_{breakthrough}$ to withstand the applied pressure $P_{applied}$ (such as hydrostatic pressure, Laplace pressure, and so on) from the contacting liquid. In other words, a superomniphobic surface must be designed in a manner that $P_{breakthrough} > P_{applied}$ to prevent the transition from the Cassie– Baxter state to the fully wetted Wenzel state.

To correlate $P_{breakthrough}$ with the parameters of a given textured surface, previous works[30, 32] have proposed a dimensionless parameter A^* called the robustness factor. A^* represents the ratio between the breakthrough pressure $P_{breakthrough}$ and a characteristic reference pressure P_{ref}, given as $P_{ref} = 2\gamma_{LV}/l_{cap}$, where $l_{cap} = \sqrt{\gamma_{LV}/\rho g}$ is the capillary length (here ρ is the liquid density, and g is the acceleration due to gravity). This reference pressure P_{ref} is near the minimum possible pressure difference across the composite interface for millimetric sized or larger liquid droplets (or puddles) on extremely non-wetting textured surfaces.[30-33] For textured substrates with discrete

spherical particles, the robustness factor A^* is given as:[30-33, 39]

(Equation 1.4) $$A^* = \frac{P_{breakthrough}}{P_{ref}} = \frac{2\pi l_{cap}}{R(2\sqrt{3}D^* - \pi)} \frac{(1-\cos\theta)}{(\sqrt{D^*} - 1 + 2\sin\theta)}$$

Any surface with $A^* >> 1$ indicates the formation of a robust composite interface with very high breakthrough pressures, whereas surfaces with $A^* < 1$ cannot form a stable composite interface, causing the liquid to penetrate the textured surface. Thus, to design patterned superomniphobic-superomniphilic surfaces, the surfaces should have well-defined domains of regions that have $A^* >> 1$, as well as, regions that have $A^* < 1$. To fabricate such patterned superomniphobic-superomniphilic surfaces (discussed in chapter 2), we first designed and fabricated surfaces with $A^* >> 1$ for almost all liquids. The surfaces were then selectively patterned with domains with $A^* < 1$ for almost all liquids.

1.6. Site-selective self-assembly of liquids on patterned surfaces

When a liquid is brought in contact with a non-wettable surface patterned with wettable domains, the liquid preferentially wets and assembles only within the wettable domains. When the liquid droplets come in contact with a patterned surface, the droplets easily roll-off the non-wettable regions even at very small tilt angles ($< 5°$), facilitating the migration of liquid droplets into the wettable regions.

Further, in the case of liquid droplets that are in contact with both a non-wettable surface (possessing low surface energy γ_{SV}) and a wettable surface (possessing high γ_{SV}), such as shown in Figure 1.4, the droplet experiences a force driving it to assemble preferentially within the wettable domains. This force is due to an imbalance in surface tension forces acting on the droplet edge (the solid-liquid-air three phase contact line).

The imbalanced force (dF_S) experienced by a section of the droplet, with thickness dx is given by[3] :

(Equation 1.5) $dF_S = \gamma_{LV}\left(\cos\theta_H - \cos\theta_L\right)dx$

Here, γ_{LV} is the surface tension of the liquid, and θ_H and θ_L are the contact angles of the liquid in the high and low surface energy regions, respectively (see Figure 1.4). The total force (F_S) on the droplet can be obtained by integrating equation 1.5 over the entire width of the droplet. This force drives the droplet towards the surface with higher solid surface energy because $\theta_H < \theta_L$. However, for surfaces that display high contact angle hysteresis, the receding contact angle on the non-wettable surface may be smaller than the advancing contact angle on the wettable domains. In such cases, the liquid droplet will not advance into the wettable domains[3]. Thus, a non-wettable surface possessing a low contact angle hysteresis, when patterned with wettable domains, can act as a template to engender the self-assembly of liquids within the wettable domains. The ability to assemble liquids in desired geometries and dimensions on patterned surfaces has been widely explored in the past decade for various applications.

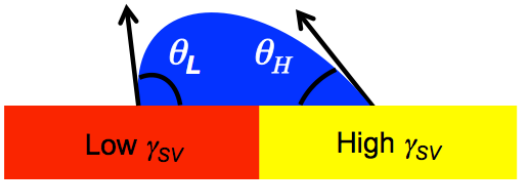

Figure 1.4. Schematic showing cross-section of a liquid droplet in contact with both wettable (high γ_{SV}) and non-wettable (low γ_{SV}) regions.

Manipulating minute volume of liquids within micron scale channels/domains is crucial for the design and fabrication of microfluidic devices for applications like

bioassays, microreactors, sensors, actuators etc.[3-8, 40, 41] Traditionally microfluidic devices have been developed using microfabricated 3-Dimensional polydimethylsiloxane (PDMS) channels. However the fabrication of PDMS based microfluidic devices involves multiple steps and costly procedures. In addition, these microfluidic devices require external hardware including pumps, valves and associated electrical components, making the devices unsuitable for applications like point-of-care diagnostics, and rapid diagnostic tests.[40, 41]

On the other hand, surfaces with patterned wettability have shown to serve as cheaper, portable, and easy to operate alternatives for the traditional microfluidic devices.[40, 41] Microfluidic analytical devices based on the patterned surfaces combine the following capabilities on to a single device: ease of distributing a liquid sample into multiple spatially assembled regions to enable multiple assays; movement of the liquid samples by capillary action (no external pumps are needed); compatibility with small sample volumes, which is very important when the sample size is limited (drops of blood from finger pricks, tears and saliva). These advantages have led researchers to develop microfluidic devices based on patterned surfaces for rapid diagnostic tests such as immunoassays[42, 43], urinalysis[44-46], food safety and environmental monitoring devices[41] etc.

Patterned surfaces have also been demonstrated as convenient lab-on-chip platforms for conducting chemical reactions with limited reactants[6, 47-49]. Further, liquid assemblies on patterned surfaces enable easy access to the liquid-vapor interface and thus make the liquid-gas reactions feasible in microfluidic systems[6].

Even though the site-selective assembly of liquids has been widely explored on

patterned surfaces, the compatibility of the patterned surfaces with low surface tension liquids such as oils, alcohols and organic solvents has been a great challenge. This is primarily because of the inherent difficulty in controlling the wetting of low surface tension liquids on a surface.

1.7. Site-selective self-assembly of solids on patterned surfaces

The site-selective self-assembly of solids can be obtained on patterned surfaces through the assembly of a dispersion of solid particles in a liquid or alternately polymer solutions within the wettable domains[9-15]. Upon evaporation of the liquid dispersant or the solvent, we obtain the assembly of solid particles or polymer films within the wettable domains. Therefore, surfaces with patterned wettability can be used as templates to develop solid patterns in desired geometries and dimensions. Several hydrophobic-hydrophilic and superhydrophobic-superhydrophilic patterned surfaces have been developed and utilized for site-selective self-assembly of solids including conducting polymer patterns for electronic applications[9-15], cell microarrays for genetic screening[41], DNA and protein arrays for biological studies[40] and ink patterns for off-set printing[50] etc.

1.8. Phase change heat transfer on patterned surfaces

Phase change heat transfer processes such as boiling and condensation heat transfer are desired in many industrial applications[51, 52] including thermal generation of electricity, desalination, high-performance heat exchangers, metallurgy, and electronics cooling.

In boiling heat transfer, a hot surface to be cooled is adjacent to a liquid that vaporizes by taking in a large heat of vaporization. The boiling performance is measured in terms of two parameters, the heat transfer coefficient (HTC) and the critical heat flux

(CHF)[21, 51]. The HTC is the ratio between the heat flux and the temperature difference between the hot surface and the liquid. The CHF is the highest heat flux that can be exchanged before the nucleated vapor bubbles merge into a continuous vapor film that insulates the surface from the liquid[51]. An optimum surface for boiling heat transfer is therefore a surface that has high values of both HTC and CHF.

Both HTC and CHF are very dependent on the wetting properties of the surface. Usually a non-wettable surface facilitates high HTC, while a wettable surface facilitates high CHF. So, an ideal boiling surface has complex requirements for surface wettability: a non-wettable surface to promote nucleation and high HTC at low heat flux and a wettable surface to maintain liquid transport to the hot surface for preventing low CHF[20, 21, 51]. Therefore, a wettable surface patterned with non-wettable domains offers an elegant solution to develop the ideal surface with optimum heat transfer properties. For example, Betz et al. have shown that patterned superhydrophobic-superhydrophilic surfaces have doubled the HTC and increased CHF by 80% compared to a homogenous superhydrophilic surface[21].

In condensation heat transfer, a cold surface is adjacent to liquid vapors, which condense on the surface releasing a large latent heat of fusion to the cold surface. Similar to the boiling process, the condensation heat transfer process is also dependent on the wettability of the surface[17, 53]. A wettable surface promotes high rates of nucleation of water droplets, while a non-wettable surface prevents the early formation of an insulating water film across the cold surface (high CHF). In order to have both high nucleation rates, as well as, to avoid the early formation of an insulating water film, it is desired to have a non-wettable surface patterned with wettable domains.

However, most of the reports on enhancement of phase change heat transfer properties on a patterned surface have so far been focused on hydrophobic-hydrophilic or superhydrophobic-superhydrophilic patterned surfaces, using surfactant free water as a heat transfer liquid. As reported in a recent review[51], one of the key challenges in surface engineering for enhanced phase change heat transfer is to develop surfaces that are compatible with low surface tension liquids such as refrigerants used in the heating, ventilation, and air-conditioning industries.

In light of the requirements for various applications discussed here, we first focused on designing and developing patterned surfaces that are universal to almost all liquids. We then extended the above-discussed applications to low surface tension liquids. Further, using the patterned surfaces as templates, we have developed a novel methodology to fabricate multi-phasic micro and nanoparticles of virtually any desired geometry and chemistry.

1.9. References

1. Zhai, L. et al. Patterned superhydrophobic surfaces: Toward a synthetic mimic of the Namib Desert beetle. *Nano Letters* **6**, 1213-1217 (2006).
2. Zheng, Y. et al. Directional water collection on wetted spider silk. *Nature* **463**, 640-643 (2010).
3. Bruzewicz, D.A., Reches, M. & Whitesides, G.M. Low-cost printing of poly(dimethylsiloxane) barriers to define microchannels in paper. *Anal Chem* **80**, 3387-3392 (2008).
4. Carrilho, E., Martinez, A.W. & Whitesides, G.M. Understanding Wax Printing: A Simple Micropatterning Process for Paper-Based Microfluidics. *Analytical Chemistry* **81**, 7091-7095 (2009).
5. Zahner, D., Abagat, J., Svec, F., Frechet, J.M.J. & Levkin, P.A. A Facile Approach to Superhydrophilic-Superhydrophobic Patterns in Porous Polymer Films. *Advanced Materials* **23**, 3030-3034 (2011).
6. Zhao, B., Moore, J.S. & Beebe, D.J. Surface-directed liquid flow inside microchannels. *Science* **291**, 1023-1026 (2001).
7. Chitnis, G., Ding, Z., Chang, C.-L., Savran, C.A. & Ziaie, B. Laser-treated hydrophobic paper: an inexpensive microfluidic platform. *Lab Chip* **11**, 1161-1165 (2011).
8. Gau, H., Herminghaus, S., Lenz, P. & Lipowsky, R. Liquid morphologies on structured surfaces: From microchannels to microchips. *Science* **283**, 46-49 (1999).
9. Balgar, T., Franzka, S., Hasselbrink, E. & Hartmann, N. Laser-assisted fabrication of submicron-structured hydrophilic/hydrophobic templates for the directed self-assembly of alkylsiloxane monolayers into confined domains. *Applied Physics a-Materials Science & Processing* **82**, 15-18 (2006).
10. Maoz, R., Cohen, S.R. & Sagiv, J. Nanoelectrochemical patterning of monolayer surfaces: Toward spatially defined self-assembly of nanostructures. *Advanced Materials* **11**, 55-61 (1999).
11. Masuda, Y., Ieda, S. & Koumoto, K. Site-selective deposition of anatase TiO2 in an aqueous solution using a seed layer. *Langmuir* **19**, 4415-4419 (2003).
12. Masuda, Y., Tomimoto, K. & Koumoto, K. Two-dimensional self-assembly of spherical particles using a liquid mold and its drying process. *Langmuir* **19**, 5179-5183 (2003).
13. Qin, D. et al. Fabrication of ordered two-dimensional arrays of micro- and nanoparticles using patterned self-assembled monolayers as templates. *Advanced Materials* **11**, 1433-1437 (1999).
14. Hohnholz, D., Okuzaki, H. & MacDiarmid, A.G. Plastic electronic devices through line patterning of conducting polymers. *Advanced Functional Materials* **15**, 51-56 (2005).
15. Li, L. et al. High-Performance and Stable Organic Transistors and Circuits with Patterned Polypyrrole Electrodes. *Advanced Materials* **24**, 2159-2164 (2012).
16. Gillmor, S.D., Thiel, A.J., Strother, T.C., Smith, L.M. & Lagally, M.G. Hydrophilic/hydrophobic patterned surfaces as templates for DNA arrays. *Langmuir* **16**, 7223-7228 (2000).

17. Varanasi, K.K., Hsu, M., Bhate, N., Yang, W. & Deng, T. Spatial control in the heterogeneous nucleation of water. *Applied Physics Letters* **95** (2009).
18. Chen, X. et al. Nanograssed Micropyramidal Architectures for Continuous Dropwise Condensation. *Advanced Functional Materials*, n/a-n/a (2011).
19. Patankar, N.A. Supernucleating surfaces for nucleate boiling and dropwise condensation heat transfer. *Soft Matter* **6**, 1613-1620 (2010).
20. Betz, A.R., Xu, J., Qiu, H. & Attinger, D. Do surfaces with mixed hydrophilic and hydrophobic areas enhance pool boiling? *Applied Physics Letters* **97** (2010).
21. Betz, A.R., Jenkins, J.R., Kim, C.J., Attinger, D. & Ieee in 2011 Ieee 24th International Conference on Micro Electro Mechanical Systems 1193-1196 (Ieee, New York; 2011).
22. Jo, H., Ahn, H.S., Kane, S. & Kim, M.H. A study of nucleate boiling heat transfer on hydrophilic, hydrophobic and heterogeneous wetting surfaces. *International Journal of Heat and Mass Transfer* **54**, 5643-5652 (2011).
23. Young, T. An Essay on the Cohesion of Fluids. *Philos. Trans. R. Soc. London* **95**, 65 (1805).
24. Zisman, W.A. Relation of the equilibrium contact angle to liquid and solid construction. *In Contact Angle, Wettability and Adhesion, ACS Advances in Chemistry Series* (1964).
25. Nishino, T., Meguro, M., Nakamae, K., Matsushita, M. & Ueda, Y. The lowest surface free energy based on -CF3 alignment. *Langmuir* **15**, 4321-4323 (1999).
26. Tuteja, A. et al. Designing superoleophobic surfaces. *Science* **318**, 1618-1622 (2007).
27. Cassie, A.B.D. & Baxter, S. Wettability of porous surfaces. *Transactions of the Faraday Society* **40**, 0546-0550 (1944).
28. Wenzel, R.N. Resistance of solid surfaces to wetting by water. *Industrial and Engineering Chemistry* **28**, 988-994 (1936).
29. Kota, A.K., Kwon, G. & Tuteja, A. The design and applications of superomniphobic surfaces. *Npg Asia Mater* **6** (2014).
30. Tuteja, A., Choi, W., Mabry, J.M., McKinley, G.H. & Cohen, R.E. Robust omniphobic surfaces. *P Natl Acad Sci USA* **105**, 18200-18205 (2008).
31. Tuteja, A. et al. Designing superoleophobic surfaces. *Science* **318**, 1618-1622 (2007).
32. Tuteja, A., Choi, W., McKinley, G.H., Cohen, R.E. & Rubner, M.F. Design parameters for superhydrophobicity and superoleophobicity. *Mrs Bulletin* **33**, 752-758 (2008).
33. Chhatre, S.S. et al. Scale Dependence of Omniphobic Mesh Surfaces. *Langmuir* **26**, 4027-4035 (2010).
34. Ahuja, A. et al. Nanonails: A simple geometrical approach to electrically tunable superlyophobic surfaces. *Langmuir* **24**, 9-14 (2008).
35. Liu, J.L., Feng, X.Q., Wang, G.F. & Yu, S.W. Mechanisms of superhydrophobicity on hydrophilic substrates. *J Phys-Condens Mat* **19** (2007).
36. Marmur, A. Wetting on hydrophobic rough surfaces: To be heterogeneous or not to be? *Langmuir* **19**, 8343-8348 (2003).

37. Marmur, A. From hygrophilic to superhygrophobic: Theoretical conditions for making high-contact-angle surfaces from low-contact-angle materials. *Langmuir* **24**, 7573-7579 (2008).
38. Nosonovsky, M. Multiscale roughness and stability of superhydrophobic biomimetic interfaces. *Langmuir* **23**, 3157-3161 (2007).
39. Kobaku, S.P.R., Kota, A.K., Lee, D.H., Mabry, J.M. & Tuteja, A. Patterned Superomniphobic-Superomniphilic Surfaces: Templates for Site-Selective Self-Assembly. *Angew Chem Int Edit* **51**, 10109-10113 (2012).
40. You, I., Yun, N. & Lee, H. Surface-Tension-Confined Microfluidics and Their Applications. *Chemphyschem* **14**, 471-481 (2013).
41. Yetisen, A.K., Akram, M.S. & Lowe, C.R. Paper-based microfluidic point-of-care diagnostic devices. *Lab Chip* **13**, 2210-2251 (2013).
42. Cheng, C.M. et al. Paper-Based ELISA. *Angew Chem Int Edit* **49**, 4771-4774 (2010).
43. Abe, K., Kotera, K., Suzuki, K. & Citterio, D. Inkjet-printed paperfluidic immuno-chemical sensing device. *Anal Bioanal Chem* **398**, 885-893 (2010).
44. Dungchai, W., Chailapakul, O. & Henry, C.S. Use of multiple colorimetric indicators for paper-based microfluidic devices. *Anal Chim Acta* **674**, 227-233 (2010).
45. Ellerbee, A.K. et al. Quantifying Colorimetric Assays in Paper-Based Microfluidic Devices by Measuring the Transmission of Light through Paper. *Anal Chem* **81**, 8447-8452 (2009).
46. Martinez, A.W. et al. Programmable diagnostic devices made from paper and tape. *Lab Chip* **10**, 2499-2504 (2010).
47. Swickrath, M.J., Burns, S.D. & Wnek, G.E. Modulating passive micromixing in 2-D microfluidic devices via discontinuities in surface energy. *Sensor Actuat B-Chem* **140**, 656-662 (2009).
48. Li, X., Tian, J.F. & Shen, W. Progress in patterned paper sizing for fabrication of paper-based microfluidic sensors. *Cellulose* **17**, 649-659 (2010).
49. You, I. et al. Polydopamine Microfluidic System toward a Two-Dimensional, Gravity-Driven Mixing Device. *Angew Chem Int Edit* **51**, 6126-6130 (2012).
50. Tian, D.L., Song, Y.L. & Jiang, L. Patterning of controllable surface wettability for printing techniques. *Chem Soc Rev* **42**, 5184-5209 (2013).
51. Attinger, D. et al. Surface engineering for phase change heat transfer: A review. *MRS Energy & Sustainability - A Review Journal* **1**, null-null (2014).
52. Bar-Cohen, A., Arik, M. & Ohadi, M. Direct liquid cooling of high flux micro and nano electronic components. *P Ieee* **94**, 1549-1570 (2006).
53. Chen, X. et al. Nanograssed Micropyramidal Architectures for Continuous Dropwise Condensation. *Advanced Functional Materials* **21**, 4617-4623 (2011).

CHAPTER 2

Patterned superomniphobic-superomniphilic surfaces

2.1. Introduction

Superhydrophobic surfaces display apparent contact angles greater than 150° and low contact angle hysteresis with water, while superoleophobic surfaces display apparent contact angles greater than 150° and low contact angle hysteresis with low surface tension liquids such as oils and alcohols.[1-4] Superomniphobic surfaces display both superhydrophobicity and superoleophobicity. Similarly, superomniphilic surfaces display both superhydrophilicity and superoleophilicity i.e., apparent contact angles ~ 0° with both water and low surface tension liquids.[5] Patterned surfaces containing well defined domains that display both these extreme wetting properties have many potential applications in fog harvesting and liquid transport,[6,7] microchannels and microreactors,[8-13] enhanced condensation[14-16] and boiling[17-19] heat transfer, and the directed growth of thin films.[20-22] Further, such surfaces can also serve as templates for the wettability-driven self-assembly of liquids,[8-13] micro- or nano-particles,[23-26] and DNA.[27] However, the majority of patterned surfaces developed, thus far, exhibit extreme wettability contrast only with high surface tension liquids such as water (surface tension, γ_{LV} = 72.1

mN m^{-1}), thereby limiting the applications of such surfaces mostly to surfactant-free aqueous systems.[8-27]

In order to expand the application range to non-aqueous systems, especially those with low surface tension liquids such as oils (e.g., heptane, γ_{LV} = 20.1 mN/m) and alcohols (e.g., methanol, γ_{LV} = 22.5 mN/m), it is crucial to develop patterned superomniphobic-superomniphilic surfaces. While there have been a few reports on switchable superoleophobic-superoleophilic surfaces,[28-31] there have been no reports on either superoleophobic or superomniphobic surfaces that are patterned with regular, well-defined superomniphilic domains (or vice-versa).

Recent work[1-4,32-34] has explained how re-entrant surface texture, in conjunction with surface chemistry and roughness, can be used to design superomniphobic surfaces. In this work, we report a simple, fast and practical methodology to develop patterned superomniphobic-superomniphilic surfaces that exhibit stark contrast in wettability with a wide range of polar and non-polar liquids. Here first we fabricate superomniphobic surfaces that repel almost all liquids. Then the superomniphobic surfaces were patterned with superomniphilic domains of desired geometries and dimensions. Using the surfaces, we demonstrate the site-selective self-assembly of heptane within the patterned superomniphilic domains upon dipping and spraying the liquid. We also demonstrate site-selective condensation and boiling with low surface tension liquids, which is crucial to design surfaces with enhanced heat-transfer properties. We further demonstrated site-selective self-assembly of both polymers and microparticles within the patterned domains upon spraying polymer solutions and particle dispersions, respectively.

2.2. Design principles

When a liquid comes in contact with a textured surface, it adopts either the fully-wetted Wenzel[35] state or the Cassie-Baxter[36] state, which supports a composite solid-liquid-air interface. The Cassie-Baxter state promotes high apparent contact angles (θ^*) and low contact angle hysteresis.[37-39] Development of superomniphobic surfaces requires the design of substrates that promote the formation of the Cassie-Baxter state with both water and low surface tension liquids. In recent work,[1-4] two dimensionless design parameters, spacing ratio D^* and robustness factor A^*, were discussed for the systematic design of superomniphobic surfaces. D^* is a measure of the air trapped underneath a liquid droplet in the Cassie-Baxter state. For textured substrates composed of discrete spherical particles (such as those considered here), $D^* = \left[(R+D)/R\right]^2$, where R is the radius of the spherical particle and D is half the inter-particle spacing. The Cassie-Baxter relationship can be written in terms of D^* as:[1-4]

(Equation 2.1) $$\cos\theta^* = -1 + \frac{1}{D^*}\left[\frac{\pi}{2\sqrt{3}}(1+\cos\theta)^2\right]$$

Here, θ is the Young's contact angle.[40] Higher values of D^* result in higher apparent contact angles (Equation 2.1). The robustness factor A^* represents the ratio between the breakthrough pressure $P_{breakthrough}$ required to force the transition from non-wetting Cassie-Baxter state to the fully-wetted Wenzel state and a characteristic reference pressure P_{ref}, given as $P_{ref} = 2\gamma_{LV}/l_{cap}$, where $l_{cap} = \sqrt{\gamma_{LV}/\rho g}$ is the capillary length (here ρ is the liquid density and g is the acceleration due to gravity). This reference pressure P_{ref} is near the minimum possible pressure difference across the composite interface for

millimetric sized or larger liquid droplets (or puddles) on extremely non-wetting textured surfaces.[1-4] For textured substrates with discrete spherical particles, the robustness factor A^* is given as:[1-4]

(Equation 2.2) $$A^* = \frac{P_{breakthrough}}{P_{ref}} = \frac{2\pi l_{cap}}{R(2\sqrt{3}D^* - \pi)} \frac{(1-\cos\theta)}{(\sqrt{D^*} - 1 + 2\sin\theta)}$$

Any surface with $A^* >> 1$ indicates the formation of a robust composite interface with very high breakthrough pressures, whereas surfaces with $A^* < 1$ cannot form a stable composite interface, causing the liquid to penetrate the textured surface.

To fabricate patterned superomniphobic-superomniphilic surfaces, we first designed and fabricated surfaces with $A^* >> 1$ for almost all liquids. Subsequently, the surfaces were selectively patterned with domains with $A^* < 1$ for almost all liquids. This allowed us to develop patterned surfaces that can assemble a wide range of liquids within patterns of different shapes and sizes.

2.3. Experimental Procedure

2.3.1. Materials

Poly(methylmethacrylate) (PMMA) with a weight-average molecular weight of $M_w \sim 35{,}000$ and polyisobutylene (PIB, $M_w \approx 400{,}000$) were obtained from Scientific Polymer Products. Poly(vinylpyrrolidone) (PVP, $M_w \approx 1{,}300{,}000$), fluorescent dyes: rhodamine B, fluorescein isothiocyanate isomer I (FITC) were obtained from Sigma-Aldrich. 1H, 1H, 2H, 2H-heptadecafluorodecyl polyhedral oligomeric silsequioxane (fluorodecyl POSS) was synthesized as described elsewhere.[2] UV fluorescent red and green polyethylene microspheres of diameter 10-45 μm were obtained from Cospheric LLC. Asahiklin AK-225 solvent was obtained from Structure Probe, Inc. Heptane,

methanol and hydrofluoric acid were obtained from Fisher Scientific. Silicon wafers, photoresist SPR 220 3.0 and photoresist developer AZ300 MIF were obtained from the cleanroom (Lurie Nanofabrication Facility) at the University of Michigan.

2.3.2. Substrate preparation

10 mg/mL solutions of 50 wt% 1H,1H,2H,2H-heptadecafluorodecyl polyhedral oligomeric silsesquioxane (fluorodecyl POSS) + poly(methylmethacrylate) were prepared in 95:5 vol:vol solvent mixture of Ashakilin AK-225 (Asahi Glass Co.):Dimethyl Formamide. The solutions were electrospun onto silicon wafers using a custom-built setup, at flow rate, voltage and plate-to-plate distance of 0.03 mL/min, 15 kV and 25 cm, respectively. Non-textured surfaces were prepared by spin-coating (Specialty Coating Systems Spincoater G3P–8) 10 mg/mL solutions of 50 wt% fluorodecyl POSS + PMMA in Ashakilin AK-225 on silicon wafers at 1500 RPM for 30 s.

2.3.3. Surface patterning

The electrospun superomniphobic surfaces were exposed to O_2 plasma (Plasmatherm 790) at single bias RF source power of 100 Watt and a pressure of 10^{-2} Torr for 5 min. Stainless steel perforated mask (McMaster-Carr) with hole diameters of 840 μm and 150 μm and center to center spacings of 1400 μm and 280 μm respectively were used to obtain superomniphobic surfaces patterned with superomniphilic domains. We have also developed a novel photoresist mask transfer method (see section 2.4.3) to obtain superomniphobic surfaces patterned with superomniphilic domains of different shapes and sizes.

2.3.4. Polymer solutions and particle dispersions

UV fluorescent red and green polyethylene microspheres (Cospheric LLC) of diameter 10-45 μm were dispersed in heptane and water, respectively, at 25 mg/mL using a vortexer. 50 mg/mL solution of poly(isobutylene) (PIB) in heptane containing a red fluorescent dye and 50 mg/mL solution of poly(vinylpyrrolidone) (PVP) in water containing a green fluorescent dye were prepared using a vortexer.

2.3.5. Characterization techniques

2.3.5.1. X-ray photoelectron spectroscopy (XPS)

XPS analysis was conducted using a Kratos Axis Ultra X-ray photoelectron spectrometer. A monochromatic Al-Kα X-ray source was operated at 15 kV and 10 mA. Photoelectrons were collected at a takeoff angle of ~ 65° relative to the sample surface. Wide-scan survey spectra were acquired at an analyzer pass energy of 160 eV and a step size of 1 eV. O 1s, F 1s and C 1s high-resolution spectra were collected at an analyzer pass energy of 60 eV and a step size of 1 eV. The peaks in the high-resolution C 1s spectra were indexed by comparing the binding energy at the peak maximum with standard spectra available for PMMA and poly(vinylidene fluoride).[41]

2.3.5.2. Contact angle measurements

The contact angle measurements were conducted using a Ramé-Hart 200-F1 goniometer. All contact angles reported in this work were measured by advancing or receding a small volume of liquid (~ 2 μL) onto the surface using a 2 mL micrometer syringe (Gilmont). At least three measurements were performed on each substrate. Typical error in measurements was ±2º.

2.3.5.3. Microscopy

The surfaces were imaged using a Hitachi SU8000 ultra-high resolution scanning electron microscope (SEM) at 5 kV and an Olympus BX 51 fluorescent microscope.

2.4. Results and discussion

2.4.1. Superomniphobic and superomniphilic surfaces

Superomniphobic surfaces were fabricated by electrospinning solutions of 50 wt% fluorodecyl POSS[1-4] + poly(methyl methacrylate) (PMMA) in Asahiklin AK-225 (see section 2.3.2). The fabricated electrospun surfaces as shown in Figure 2.1 are highly porous and have re-entrant, bead morphology. We estimated the porosity of the electrospun surfaces terms of spacing ratio, D^* = 15.9. We used equation 2.1 in the main manuscript, in conjunction with contact angle measurements (Table 2.1), to estimate the spacing ratio. From Figure 2.1a, we obtained the average size of the electrospun beads, $2R$ = 13.4 μm. The high porosity of the electrospun surface, combined with the low surface energy of 50 wt% fluorodecyl POSS + PMMA blend (γ_{SV} = 11.1 mN m^{-1}, see section 2.5), leads to superomniphobicity[1-4] with a high robustness factor, high advancing contact angle (see Figure 2.1b), and low contact angle hysteresis for water (A^* = 16.2, θ^*_{adv} = 162° and $\Delta\theta^*$ = 2°), as well as, for various low surface tension liquids (see Table 2.1), such as heptane (A^* = 3.4, θ^*_{adv} = 151° and $\Delta\theta^*$ = 10°).

To switch the superomniphobic surfaces to superomniphilic, we exposed the surfaces to O_2 plasma. This resulted in $\theta^*_{adv} = \theta^*_{rec} \approx 0°$ for both water and heptane (see Figure 2.1b). These contact angles remain unchanged with time (see Figure 2.2). The

morphology of the electrospun beads also remains unaffected after O_2 plasma treatment (see Figure 2.1a).

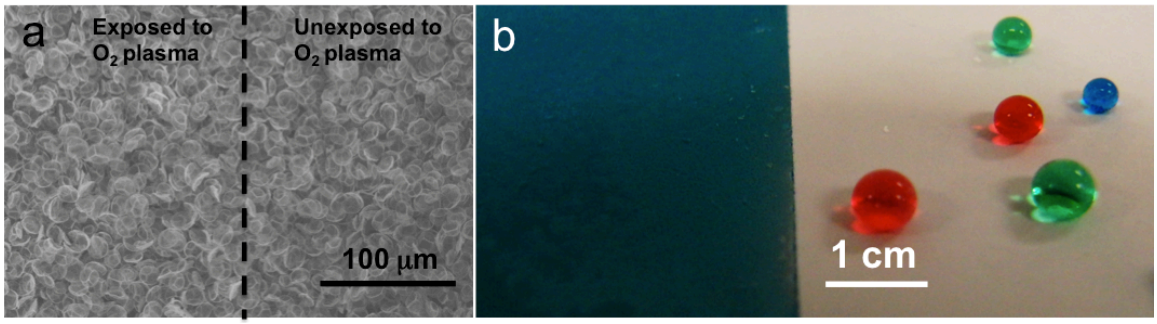

Figure 2.1. Patterned superomniphobic-superomniphilic surfaces. a) An SEM image showing electrospun bead morphology at the interface of the areas exposed and not exposed to O_2 plasma. This image indicates that there is no change in the bead morphology after O_2 plasma treatment. b) An electrospun bead surface (composed of 50 wt% fluorodecyl POSS + PMMA) that was exposed to O_2 plasma on the left (superomniphilic) and not exposed to O_2 plasma on the right (superomniphobic). Water (dyed blue) completely wets the superomniphilic region, but shows a high contact angle on the superomniphobic region. Heptane (dyed red) and methanol (dyed green) also show high contact angles on the superomniphobic region. The reflective surface visible underneath the droplets on the superomniphobic surface indicates the presence of microscopic pockets of air due to the formation of a composite interface.

However, O_2 plasma treatment results in oxygen enrichment and simultaneous defluorination of the surface as indicated by the change in peak intensities for the oxygen 1s, fluorine 1s (see Figure 2.3) and the $-CF_2$ and $-CF_3$ groups in the high-resolution carbon 1s (see Figure 2.3) XPS spectra. The surface is likely defluorinated due to the degradation of the fluorinated end groups in fluorodecyl POSS.[42,43] The change in surface chemistry and consequently the change in surface energy (increased to γ_{SV} = 67.8 mN m^{-1}, see section 2.4.2) upon O_2 plasma treatment are also confirmed by contact angle measurements on non-textured surfaces spin-coated with 50 wt% fluorodecyl POSS + PMMA blend. For non-textured surfaces, the contact angles for water decreased from θ_{adv} = 123°, θ_{rec} = 110° to θ_{adv} = 20°, θ_{rec} = 0°, while those for heptane decreased from

θ_{adv} = 61°, θ_{rec} = 38° to θ_{adv} = 10°, θ_{rec} = 0° upon O_2 plasma treatment. This results in extremely low robustness factors, A^* = 0.8 for water and A^* = 0.1 for heptane on the electrospun bead surface, which explain the superomniphilic behavior after O_2 plasma treatment.

Table 2.1. Contact angles on electrospun surfaces composed of 50 wt% fluorodecyl POSS + PMMA before and after O_2 plasma treatment.

	Electrospun surface					
	Water		Heptane		Methanol	
	θ^*_{adv}	θ^*_{rec}	θ^*_{adv}	θ^*_{rec}	θ^*_{adv}	θ^*_{rec}
Before O_2 plasma treatment	162°	160°	151°	141°	153°	145°
After O_2 plasma treatment	0°	0°	0°	0°	0°	0°

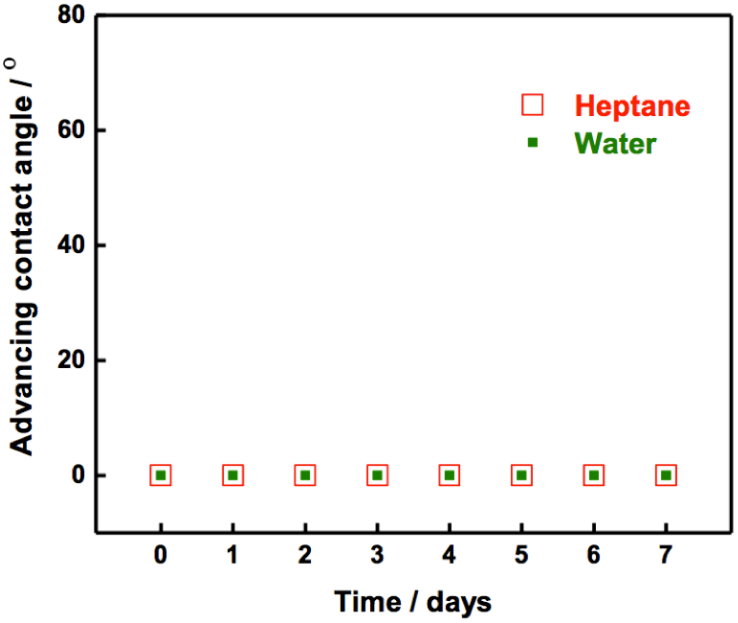

Figure 2.2. The apparent advancing contact angles of water and heptane on the superomniphilic surface at various times after O_2 plasma treatment.

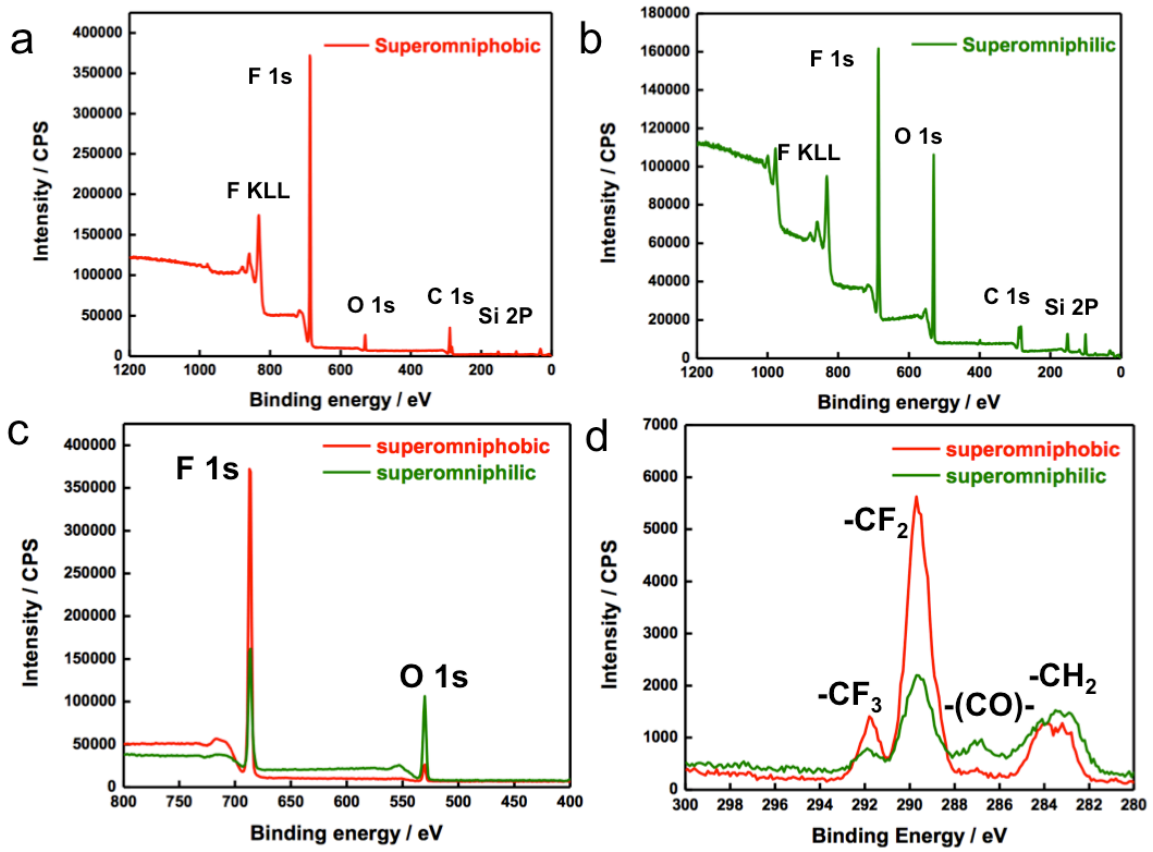

Figure 2.3. XPS spectra for the superomniphobic surface and the superomniphilic surfaces. a) and b) Survey spectra showing intensity of different elements present on a superomniphobic surface and a superomniphilic surface, respectively. The characteristic peaks for carbon, fluorine, oxygen and silicon within the spectra are labeled. (c) Fluorine and oxygen elemental peaks for superomniphobic and the superomniphilic surfaces. (d) High- resolution carbon 1s peaks corresponding to the different carbon moieties present on the surface.

2.4.2. Estimation of solid surface energy

We used the Owens and Wendt approach[44] to estimate the surface energy γ_{SV} of the 50 wt% fluorodecyl POSS + PMMA blend surface before and after O_2 plasma treatment. According to this approach, the solid surface energy is the sum of contributions from two types of intermolecular forces at the surface:

(Equation 2.3) $\gamma_{SV} = \gamma_{SV}^{p} + \gamma_{SV}^{d}$

Here γ_{SV}^{d} accounts for the dispersive component of the surface energy, while γ_{SV}^{p} accounts for the polar component of the surface energy. Further, this approach postulates that:

(Equation 2.4) $\gamma_{SL} = \gamma_{SV} + \gamma_{LV} - 2\sqrt{\gamma_{SV}^{d}\gamma_{LV}^{d}} - 2\sqrt{\gamma_{SV}^{p}\gamma_{LV}^{p}}$

Here, γ_{LV}^{p} and γ_{LV}^{d} are the polar and dispersive components of the liquid surface tension respectively. Combining equations 2.3 and 2.4 with the Young's equation (equation 1.1) and recognizing that the polar component of liquid surface tension is zero γ_{LV}^{p} for non-polar liquids such as oils, the dispersive component of solid surface energy is given as:

(Equation 2.5) $\gamma_{SV}^{d} = \gamma_{LV}\left(\frac{1+\cos\theta}{2}\right)^{2}$

Here, γ_{LV} is the surface tension of a non-polar liquid and θ is the equilibrium contact angle of the same non-polar liquid on the solid surface. We used heptane (γ_{LV} = 20.1 mN/m) as the non-polar liquid to estimate γ_{SV}^{d}. After determining the dispersive component γ_{SV}^{d}, the polar component of the solid surface energy γ_{SV}^{p}, is determined using a polar liquid:

(Equation 2.6) $\gamma_{SV}^{p} = \frac{1}{\gamma_{LV}^{p}}\left(\frac{\gamma_{LV}(1+\cos\theta)}{2} - \sqrt{\gamma_{SV}^{d}\gamma_{LV}^{d}}\right)^{2}$

Here γ_{LV}^{p} and γ_{LV} are the polar component of the surface tension and the total surface tension of a polar liquid and θ is the equilibrium contact angle for the same polar liquid on the solid surface. We used water (γ_{LV}^{p} = 51.0 mN/m and γ_{LV}^{d} =21.1) as the polar liquid to estimate γ_{SV}^{p}. Finally total solid surface energy γ_{SV} is given by the summation of γ_{SV}^{p} and γ_{SV}^{d}.

The solid surface energy values were estimated by using the advancing contact angles measured on spin-coated surfaces before and after O_2 plasma treatment (Table S2). The calculated surface energies are reported in Table 2.3.

Table 2.2. Contact angles on spin-coated 50 wt% fluorodecyl POSS + PMMA surfaces before and after O_2 plasma treatment.

	Spin-coated surface					
	Water		Heptane		Methanol	
	θ_{adv}	θ_{rec}	θ_{adv}	θ_{rec}	θ_{adv}	θ_{rec}
Before O_2 plasma treatment	123°	110°	61°	38°	64°	43°
After O_2 plasma treatment	20°	0°	10°	0°	11°	0°

Table 2.3. Estimated solid surface energies for 50 wt% fluorodecyl POSS + PMMA blend before and after O_2 plasma treatment.

	Surface energy (mN m^{-1})		
	Polar component (γ_{SV}^{p})	Dispersive component (γ_{SV}^{d})	Total (γ_{SV})
Before O_2 plasma treatment	11.08	0.02	11.1
After O_2 plasma treatment	19.8	48.0	67.8

2.4.3. Photoresist mask transfer (PRMT) method

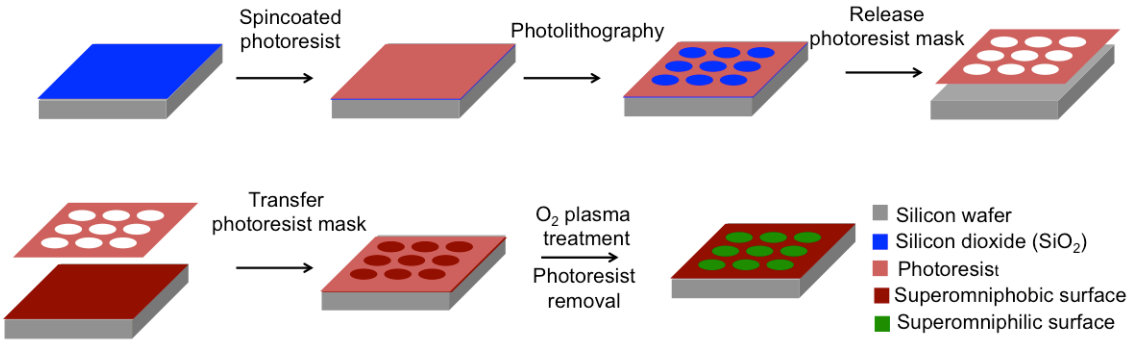

Figure 2.4. Schematic showing the steps of the photoresist mask transfer (PRMT) method.

In order to make the fabrication of patterned superomniphobic-superomniphilic surfaces with different sizes and shapes easier and more universal, we have developed the photoresist mask transfer method, as shown in Figure 2.4. Since the photoresist cannot be spin-coated on a superomniphobic surface due to its extreme non-wettability, we used an alternative technique to transfer the photoresist mask onto the superomniphobic surface. In this method, a 1 μm thick layer of silicon dioxide (SiO_2) is deposited on a silicon wafer using plasma enhanced chemical vapor deposition (PECVD). The photoresist (SPR 220 3.0) is spin-coated at 3000 rpm on the SiO_2 surface. This resulted in a 3 μm thick photoresist film. The photoresist film is then patterned with the desired geometry using photolithography and developed (in AG 300 MIF, manufacturer). The developed photoresist film is then lifted off from the silicon wafer by dissolving SiO_2 in dilute hydrofluoric acid and transferred onto the electrospun superomniphobic surface. Using the developed photoresist film as a mask, the electrospun superomniphobic surface is exposed to O_2 plasma. After O_2 plasma exposure, the photoresist mask is removed by degrading with ultraviolet light (365 nm) and dissolving in the photoresist developer (AG 300 MIF). Thus, patterned superomniphobic-superomniphilic surfaces are obtained.

Overall the PRMT methodology allows us to easily fabricate superomniphilic domains of different sizes and shapes.

2.4.4. Site-selective self-assembly of liquids

When such a patterned surface (see Figure 2.5a) is dipped in heptane (dyed red), heptane selectively wets each of the superomniphilic domains due to the extreme contrast in wettability, resulting in the self-assembly of heptane droplets within the superomniphilic patterns (see Figure 2.5b). This self-assembly is also assisted by the low contact angle hysteresis of heptane ($\Delta\theta^* = 10°$, roll-off angle $\approx 7°$, the minimum angle at which liquid droplets roll-off the surface under it's own gravity) on the superomniphobic regions. Similar self-assembly of heptane droplets is also obtained by spraying heptane on the patterned surfaces. Figures 2.5c-5f show the site-selective self-assembly of heptane droplets on superomniphobic surfaces patterned with either circular or striped superomniphilic domains. Such self-assembled organic liquids can serve as surface-directed microchannels and microreactor arrays for liquid-phase reactions. [8-13,45,46]

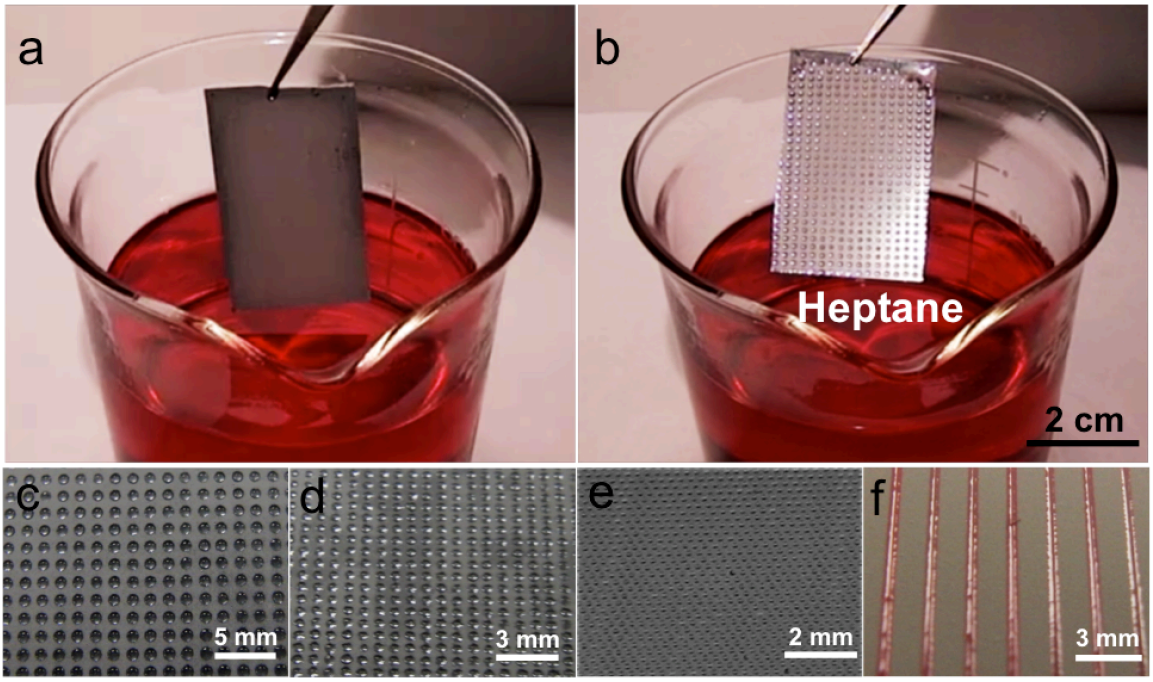

Figure 2.5. Site-selective self-assembly of heptane a) A superomniphobic surface patterned with superomniphilic domains before dipping in a beaker filled with heptane (dyed red). b) Site-selective self-assembly of heptane droplets within the superomniphilic domains after dipping in heptane. c), d), e) and f) Site-selective self-assembly obtained by spraying heptane on patterned surfaces with superomniphilic domains. Surfaces in c), d), and e) have circular superomniphilic domains of diameters 800 μm, 510 μm, and 150 μm, respectively. Surface in f) has striped superomniphilic domains of width 500 μm.

2.4.5 Patterned surface to enhance condensation and boiling heat transfer

It has been recently demonstrated that superhydrophobic surfaces with superhydrophilic domains enhance condensation heat transfer,[14,47] while superhydrophilic surfaces with superhydrophobic domains enhance boiling heat transfer.[17,18] However, such surfaces can enhance heat transfer only when water is the heat transfer fluid. Many heat transfer operations (e.g., refrigeration and distillation) involve non-aqueous liquids with low surface tension. Here, we demonstrate the applicability of our patterned superomniphobic-superomniphilic surfaces in potentially enhancing condensation and boiling heat transfer even with low surface tension liquids.

2.4.5.1 Site-selective condensation of heptane vapors

We used the setup shown in Figure 2.6 to expose the superomniphobic surface patterned with superomniphilic domains to heptane vapors. The reservoir of liquid heptane was heated to 50°C using a hot plate and the patterned substrate was at room temperature (~ 25°C). Figures 2.7a and 2.7b illustrate how heptane vapors preferentially condense on, and wet, the superomniphilic domains. This is because of the strong dependence of heterogeneous nucleation on the Young's contact angle of the surface.[8] We estimate that the nucleation rate for heptane condensation on the superomniphilic regions of the surface is ~ *5 orders of magnitude* higher than that on the superomniphobic regions, based on Volmer's classical nucleation theory[48,49] (see section 2.4.5.2). Note that this site-selective condensation in superomniphilic domains is observed even though the Young's contact angle for heptane on both the superomniphobic domains (θ_{adv} = 61°) and the superomniphilic domains (θ_{adv} = 10°) is less than 90º, i.e., both the domains are inherently oleophilic. In our control experiments, we observed a similar site-selective condensation of heptane vapors on non-textured (smooth) surfaces with patterned wettability. However, similar to previous reports,[9] we observed that the patterned non-textured surfaces do not promote roll-off of the condensed droplets like the patterned superomniphobic surfaces. Surfaces that provide high nucleation rates for condensation (superomniphilic domains), while also providing efficient roll-off of the condensed droplets, are important as they promote drop-wise condensation over film-wise condensation.[14,47]

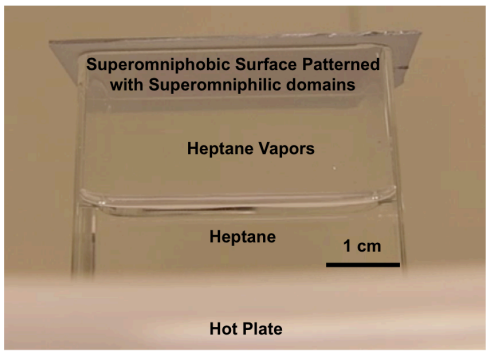

Figure 2.6. Experimental setup used for the condensation of heptane on superomniphobic surface patterned with superomniphilic domains

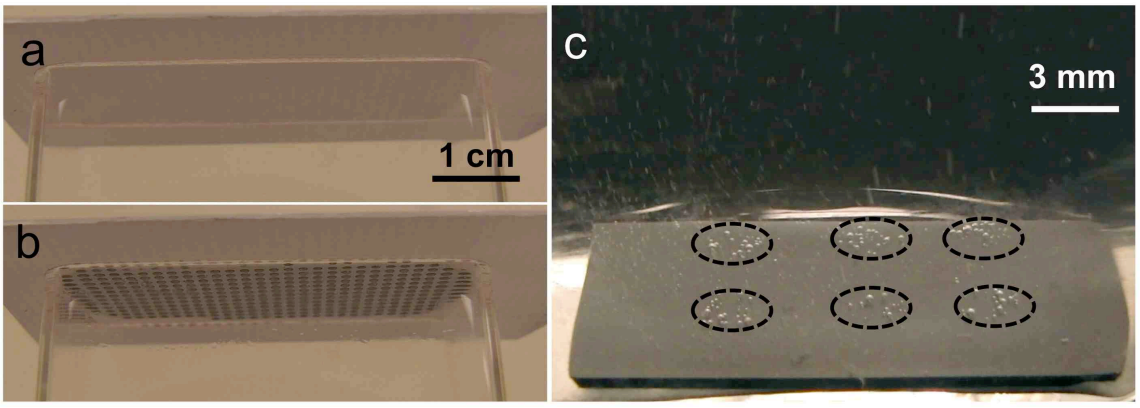

Figure 2.7. Site-selective condensation and boiling of liquids a) and b) Superomniphobic surface patterned with superomniphilic domains before and after exposure, respectively, to heptane vapors. The site-selective condensation of heptane vapors within the superomniphilic domains is evident in (b). c) Superomniphilic surface patterned with superomniphobic domains immersed in boiling methanol. It is evident that the methanol vapor bubbles preferentially nucleate on the superomniphobic domains (black dashed circles).

2.4.5.2 Comparison of heptane nucleation rates in superomniphobic and superomniphilic regions

The free energy barrier for the nucleation of a liquid droplet on a flat surface is strongly dependent on the Young's contact angle θ. According to Volmer's classical nucleation theory, the free energy barrier for nucleation is given as[14,48,49]:

(Equation 2.7) $\Delta G = \pi \gamma_{LV} r^2 (2 - 3\cos\theta + \cos^3\theta)/3$

Here, γ_{LV} is the surface tension of the liquid and r is the critical radius. The critical radius is given by Kelvin's classical equation:

(Equation 2.8) $\ln\left(P/P_o\right) = 2\gamma_{LV}M_V/RTr$

Here, P_o is the vapor pressure over the flat surface of the liquid, P is the vapor pressure over a curved surface of a condensed liquid droplet with radius r, M_V is the molar volume of the liquid, T is the temperature and R is the universal gas constant. The vapor pressure over the flat surface of a liquid at a given temperature T (in °C) is given by the Antoine equation[50]:

(Equation 2.9) $\ln P_o = A - \dfrac{B}{T+C}$

Here, P_o is in kPa. A, B and C are the parameters for the Antoine equation. For heptane, A =13.86, B = 2910.26 and C = 216.43.[50] From equation 2.9, the vapor pressure P_o = 5.2 kPa at 25°C (substrate temperature). Assuming equilibrium between the reservoir of liquid heptane (at 50°C) and the heptane vapors, the vapor pressure over the curved surface of a condensed heptane droplet P = vapor pressure of heptane P_o at 50°C. Thus, from equation 2.9, we obtain P = 18.9 kPa. Substituting the values of P and P_o into equation 2.8, we estimate the critical radius r of nucleation for heptane = 2.1 nm. The nucleation rate, J, is related to the free energy barrier ΔG by the relation[14,48,49]:

(Equation 2.10) $J = J_o \exp\left(\Delta G/kT\right) = J_o \exp\left(\pi\gamma_{LV}r^2\left(2-3\cos\theta+\cos^3\theta\right)\Big/3kT\right)$

Here, k is the Boltzmann's constant. From equation (2.10), we obtain the ratio of nucleation rates for heptane condensation in the superomniphilic regions (with θ_{adv} = 10°) to that in the superomniphobic regions (with θ_{adv} = 61°) to be ~10^5.

2.4.5.3. Site-selective evaporation of methanol

We also immersed our superomniphilic surface patterned with superomniphobic domains in boiling methanol at 65°C (the boiling point for methanol). Figure 2.7c illustrates that the methanol vapor bubbles preferentially nucleate on the superomniphobic domains. Surfaces that are not easily wet by the boiling liquid (i.e., surfaces with low surface energy) exhibit a high value for the boiling heat transfer coefficient (HTC) because they facilitate bubble nucleation. In our control experiments, we observed that low surface energy, non-textured surfaces facilitate bubble nucleation. However, as reported previously,[18] the cavities (air trapped) in low surface energy textured surfaces provide additional sites for nucleation of vapor bubbles. Consequently, superomniphobic surfaces are expected to yield high values for the HTC,[18] even for low surface tension heat transfer liquids. As the heat flux increases, the rate of nucleation of bubbles increases, and at the critical heat flux (CHF), the over-crowded bubbles coalesce to form a continuous vapor film between the heating surface and the boiling liquid.[17,18] This vapor film possesses a high thermal resistance and acts as a barrier to heat transfer. Thus, it is desirable to increase the CHF.[17,18] High CHF can be achieved by utilizing surfaces that are easily wet by the boiling liquid (i.e., surfaces with high surface energy). [18] Consequently, superomniphilic surfaces are expected to yield a high CHF. Surfaces that provide high nucleation rates for boiling (superomniphobic domains), while also efficiently preventing the formation of a continuous vapor film (superomniphilic surface), even with low surface tension liquid systems, such as those developed here, are therefore of significant importance for simultaneously increasing both HTC and CHF.

Our patterned surfaces provide an avenue for systematically varying the domain size and the inter-domain spacing in order to study enhanced condensation and boiling heat transfer[14,17,18,47] with both high and low surface tension liquids.

2.4.6. Site-selective self-assembly of microparticles and polymers

Additionally, we have utilized our superomniphobic surfaces patterned with superomniphilic domains as templates for wettability-driven site-selective self-assembly of microparticles and polymers. When a dispersion of UV fluorescent green microspheres in water is sprayed on the patterned surface, water droplets and consequently the microspheres are confined within the superomniphilic domains. After the water dries, the microspheres are deposited within the superomniphilic domain (see inset in Figure 2.8a), resulting in site-selective self-assembly of microspheres (see Figure 2.8a). Similarly, we obtained site-selective self-assembly of UV fluorescent red microspheres in heptane (see Figure 2.8b). We also obtained site-selective self-assembly of poly(vinyl pyrrolidone) (PVP, $M_w \approx 1{,}300{,}000$) films (see Figure 2.8c) and poly(isobutylene) (PIB, $M_w \approx$ 400,000) films (see Figure 2.8d) by spraying solutions of PVP (10 wt%) in water and PIB (10 wt%) in heptane, respectively.

We also obtained PIB films of different sizes and shapes using our PRMT methodology (see Figures 2.8e-8h). Thus, our methodology offers a simple route to make precisely tailored arrays of microparticles and polymer films of different sizes and shapes on textured surfaces, using both high and low surface tension liquids. Such precise control over the site-selective self-assembly of particles and films can be useful in developing electronic and optical devices,[23,24] patterned assembly of cells, and growth of well defined thin films and nanostructures (3-D assembly).[20-22]

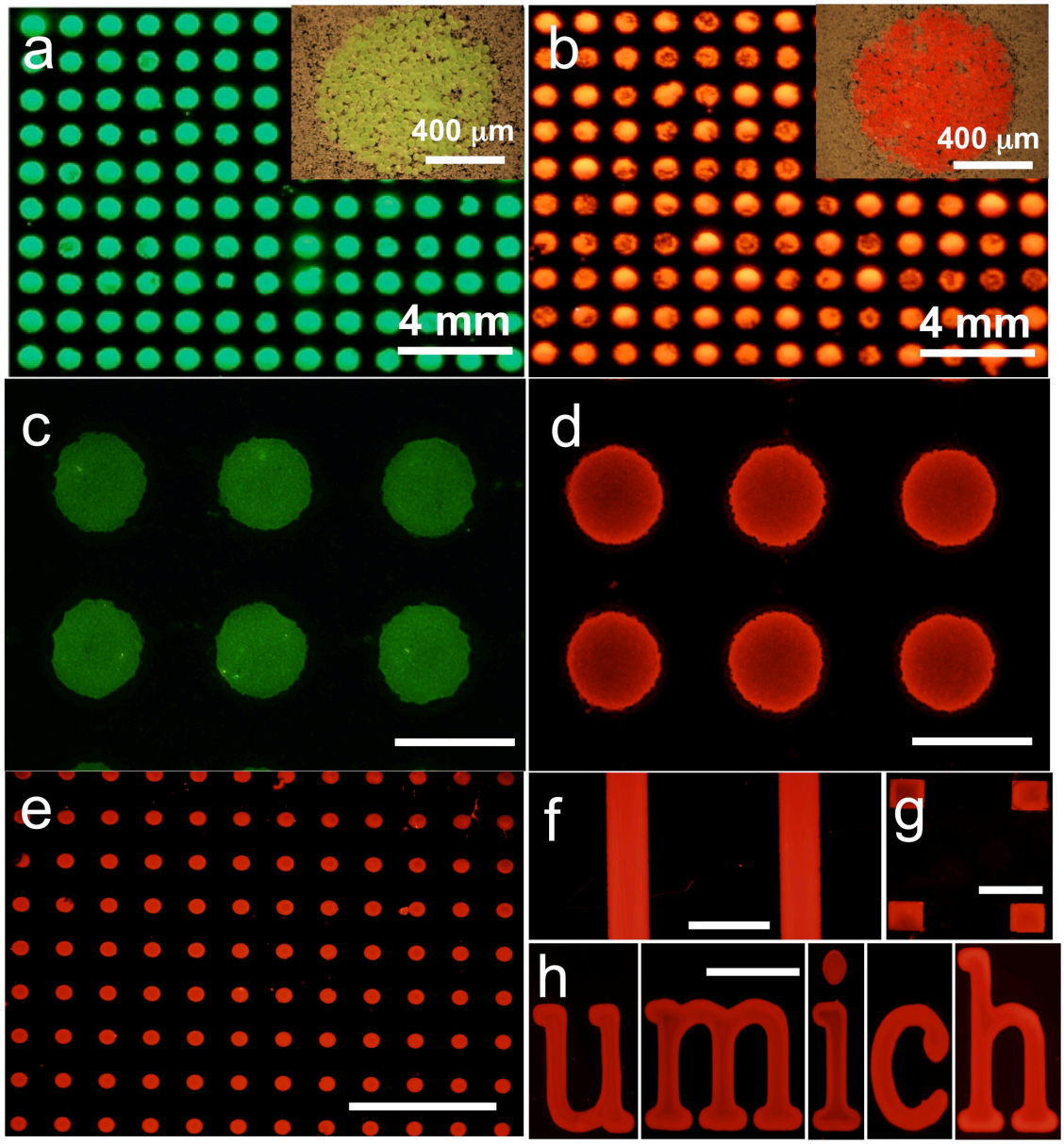

Figure 2.8. Site-selective self-assembly of solids within the patterned superomniphilic domains. a) and b) Site-selective self-assembly of UV fluorescent green microspheres dispersed in water and UV fluorescent red microspheres dispersed in heptane, respectively. (a) and (b) were obtained under a 365 nm UV lamp and the corresponding insets show higher magnification optical microscope images. c) Site-selective self-assembly of PVP dissolved in water using 800 μm diameter circular superomniphilic domains. d) and e) Site-selective self-assembly of PIB dissolved in heptane using 800 μm and 100 μm diameter circular superomniphilic domains, respectively. f), g), and h) Site-selective self-assembly of PIB using superomniphilic domains of non-circular shapes. c), d), e), f), g) and h) were obtained using fluorescent microscopy and scale bars represent 1 mm.

2.5. Conclusions

In conclusion, we have demonstrated a facile methodology to create patterned superomniphobic-superomniphilic surfaces. Utilizing our patterned surfaces, we have obtained site-selective self-assembly of heptane droplets via dipping and spraying. Such self-assembled organic liquids can serve as microreactor arrays for liquid-phase reactions. We have also demonstrated the preferential condensation of heptane within patterned superomniphilic domains and preferential boiling of methanol on patterned superomniphobic domains. Such surfaces provide an avenue to study enhanced condensation and boiling heat transfer with both high and low surface tension liquids. We have also utilized our superomniphobic surfaces patterned with superomniphilic domains as templates for wettability-driven site-selective self-assembly of microparticles and polymers.

2.6. References

1 Tuteja, A., Choi, W., Mabry, J. M., McKinley, G. H. & Cohen, R. E. Robust omniphobic surfaces. *P Natl Acad Sci USA* **105**, 18200-18205, (2008).

2 Tuteja, A., Choi, W., Ma, M., Mabry, J. M., Mazzella, S. A., Rutledge, G. C., McKinley, G. H. & Cohen, R. E. Designing superoleophobic surfaces. *Science* **318**, 1618-1622, (2007).

3 Tuteja, A., Choi, W., McKinley, G. H., Cohen, R. E. & Rubner, M. F. Design parameters for superhydrophobicity and superoleophobicity. *Mrs Bulletin* **33**, 752-758, (2008).

4 Chhatre, S. S., Choi, W., Tuteja, A., Park, K. C., Mabry, J. M., McKinley, G. H. & Cohen, R. E. Scale Dependence of Omniphobic Mesh Surfaces. *Langmuir* **26**, 4027-4035, (2010).

5 Koch, K., Blecher, I. C., Koenig, G., Kehraus, S. & Barthlott, W. The superhydrophilic and superoleophilic leaf surface of Ruellia devosiana (Acanthaceae): a biological model for spreading of water and oil on surfaces. *Functional Plant Biology* **36**, 339-350, (2009).

6 Zhai, L., Berg, M. C., Cebeci, F. C., Kim, Y., Milwid, J. M., Rubner, M. F. & Cohen, R. E. Patterned superhydrophobic surfaces: Toward a synthetic mimic of the Namib Desert beetle. *Nano Lett* **6**, 1213-1217, (2006).

7 Zheng, Y., Bai, H., Huang, Z., Tian, X., Nie, F.-Q., Zhao, Y., Zhai, J. & Jiang, L. Directional water collection on wetted spider silk. *Nature* **463**, 640-643, (2010).

8 Bruzewicz, D. A., Reches, M. & Whitesides, G. M. Low-cost printing of poly(dimethylsiloxane) barriers to define microchannels in paper. *Anal Chem* **80**, 3387-3392, (2008).

9 Carrilho, E., Martinez, A. W. & Whitesides, G. M. Understanding Wax Printing: A Simple Micropatterning Process for Paper-Based Microfluidics. *Analytical Chemistry* **81**, 7091-7095, (2009).

10 Zahner, D., Abagat, J., Svec, F., Frechet, J. M. J. & Levkin, P. A. A Facile Approach to Superhydrophilic-Superhydrophobic Patterns in Porous Polymer Films. *Adv Mater* **23**, 3030-+, (2011).

11 Zhao, B., Moore, J. S. & Beebe, D. J. Surface-directed liquid flow inside microchannels. *Science* **291**, 1023-1026, (2001).

12 Chitnis, G., Ding, Z., Chang, C.-L., Savran, C. A. & Ziaie, B. Laser-treated hydrophobic paper: an inexpensive microfluidic platform. *Lab Chip* **11**, 1161-1165, (2011).

13 Gau, H., Herminghaus, S., Lenz, P. & Lipowsky, R. Liquid morphologies on structured surfaces: From microchannels to microchips. *Science* **283**, 46-49, (1999).

14 Varanasi, K. K., Hsu, M., Bhate, N., Yang, W. & Deng, T. Spatial control in the heterogeneous nucleation of water. *Applied Physics Letters* **95**, (2009).

15 Chen, X., Wu, J., Ma, R., Hua, M., Koratkar, N., Yao, S. & Wang, Z. Nanograssed Micropyramidal Architectures for Continuous Dropwise Condensation. *Adv Funct Mater*, n/a-n/a, (2011).

16 Patankar, N. A. Supernucleating surfaces for nucleate boiling and dropwise condensation heat transfer. *Soft Matter* **6**, 1613-1620, (2010).

17 Betz, A. R., Xu, J., Qiu, H. & Attinger, D. Do surfaces with mixed hydrophilic and hydrophobic areas enhance pool boiling? *Appl Phys Lett* **97**, (2010).
18 Betz, A. R., Jenkins, J. R., Kim, C. J., Attinger, D. & Ieee. in *2011 Ieee 24th International Conference on Micro Electro Mechanical Systems Proceedings: Ieee Micro Electro Mechanical Systems* 1193-1196 (Ieee, 2011).
19 Jo, H., Ahn, H. S., Kane, S. & Kim, M. H. A study of nucleate boiling heat transfer on hydrophilic, hydrophobic and heterogeneous wetting surfaces. *International Journal of Heat and Mass Transfer* **54**, 5643-5652, (2011).
20 Balgar, T., Franzka, S., Hasselbrink, E. & Hartmann, N. Laser-assisted fabrication of submicron-structured hydrophilic/hydrophobic templates for the directed self-assembly of alkylsiloxane monolayers into confined domains. *Applied Physics a-Materials Science & Processing* **82**, 15-18, (2006).
21 Maoz, R., Cohen, S. R. & Sagiv, J. Nanoelectrochemical patterning of monolayer surfaces: Toward spatially defined self-assembly of nanostructures. *Adv Mater* **11**, 55-61, (1999).
22 Masuda, Y., Ieda, S. & Koumoto, K. Site-selective deposition of anatase TiO2 in an aqueous solution using a seed layer. *Langmuir* **19**, 4415-4419, (2003).
23 Masuda, Y., Tomimoto, K. & Koumoto, K. Two-dimensional self-assembly of spherical particles using a liquid mold and its drying process. *Langmuir* **19**, 5179-5183, (2003).
24 Qin, D., Xia, Y. N., Xu, B., Yang, H., Zhu, C. & Whitesides, G. M. Fabrication of ordered two-dimensional arrays of micro- and nanoparticles using patterned self-assembled monolayers as templates. *Adv Mater* **11**, 1433-1437, (1999).
25 Hohnholz, D., Okuzaki, H. & MacDiarmid, A. G. Plastic electronic devices through line patterning of conducting polymers. *Advanced Functional Materials* **15**, 51-56, (2005).
26 Li, L., Jiang, L., Wang, W., Du, C., Fuchs, H., Hu, W. & Chi, L. High-Performance and Stable Organic Transistors and Circuits with Patterned Polypyrrole Electrodes. *Advanced Materials* **24**, 2159-2164, (2012).
27 Gillmor, S. D., Thiel, A. J., Strother, T. C., Smith, L. M. & Lagally, M. G. Hydrophilic/hydrophobic patterned surfaces as templates for DNA arrays. *Langmuir* **16**, 7223-7228, (2000).
28 Yang, J., Zhang, Z., Men, X., Xu, X., Zhu, X., Zhou, X. & Xue, Q. Rapid and reversible switching between superoleophobicity and superoleophilicity in response to counterion exchange. *J Colloid Interf Sci* **366**, 191-195, (2012).
29 Zhang, M., Zhang, T. & Cui, T. Wettability Conversion from Superoleophobic to Superhydrophilic on Titania/Single-Walled Carbon Nanotube Composite Coatings. *Langmuir* **27**, 9295-9301, (2011).
30 Zimmermann, J., Rabe, M., Artus, G. R. J. & Seeger, S. Patterned superfunctional surfaces based on a silicone nanofilament coating. *Soft Matter* **4**, 450-452, (2008).
31 Choi, W., Tuteja, A., Chhatre, S., Mabry, J. M., Cohen, R. E. & McKinley, G. H. Fabrics with Tunable Oleophobicity. *Adv Mater* **21**, 2190-2195, (2009).
32 Ahuja, A., Taylor, J. A., Lifton, V., Sidorenko, A. A., Salamon, T. R., Lobaton, E. J., Kolodner, P. & Krupenkin, T. N. Nanonails: A simple geometrical approach to electrically tunable superlyophobic surfaces. *Langmuir* **24**, 9-14, (2008).

33 Cao, L., Price, T. P., Weiss, M. & Gao, D. Super water- and oil-repellent surfaces on intrinsically hydrophilic and oleophilic porous silicon films. *Langmuir* **24**, 1640-1643, (2008).
34 Marmur, A. From hygrophilic to superhygrophobic: Theoretical conditions for making high-contact-angle surfaces from low-contact-angle materials. *Langmuir* **24**, 7573-7579, (2008).
35 Wenzel, R. N. Resistance of solid surfaces to wetting by water. *Industrial and Engineering Chemistry* **28**, 988-994, (1936).
36 Cassie, A. B. D. & Baxter, S. Wettability of porous surfaces. *Trans. Faraday Soc.* **40**, 0546-0550, (1944).
37 Chen, W., Fadeev, A. Y., Hsieh, M. C., Oner, D., Youngblood, J. & McCarthy, T. J. Ultrahydrophobic and ultralyophobic surfaces: Some comments and examples. *Langmuir* **15**, 3395-3399, (1999).
38 Extrand, C. W. Model for contact angles and hysteresis on rough and ultraphobic surfaces. *Langmuir* **18**, 7991-7999, (2002).
39 Lafuma, A. & Quere, D. Superhydrophobic states. *Nat Mater* **2**, 457-460, (2003).
40 Young, T. An Essay on the Cohesion of Fluids. *Philos. Trans. R. Soc. London* **95**, 65, (1805).
41 Beamson, G., Briggs, D. High resolution XPS of organic polymers : the Scienta ESCA300 database. *Wiley, Chichester [England]; New York*, (1992).
42 Li, X., Tian, J., Nguyen, T. & Shen, W. Paper-Based Microfluidic Devices by Plasma Treatment. *Anal Chem* **80**, 9131-9134, (2008).
43 Zhu, X., Zhang, Z., Xu, X., Men, X., Yang, J., Zhou, X. & Xue, Q. Rapid Control of Switchable Oil Wettability and Adhesion on the Copper Substrate. *Langmuir* **27**, 14508-14513, (2011).
44 Owens, D. K. & Wendt, R. C. ESTIMATION OF SURFACE FREE ENERGY OF POLYMERS. *Journal of Applied Polymer Science* **13**, 1741-&, (1969).
45 Wang, B., Zhao, Q. H., Wang, F. & Gao, C. Y. Biologically driven assembly of polyelectrolyte microcapsule patterns to fabricate microreactor arrays. *Angewandte Chemie-International Edition* **45**, 1560-1563, (2006).
46 Wang, Z., Shang, H. & Lee, G. U. Nanoliter-scale reactor arrays for biochemical sensing. *Langmuir* **22**, 6723-6726, (2006).
47 Chen, X., Wu, J., Ma, R., Hua, M., Koratkar, N., Yao, S. & Wang, Z. Nanograssed Micropyramidal Architectures for Continuous Dropwise Condensation. *Advanced Functional Materials* **21**, 4617-4623, (2011).
48 Sigsbee, R. A. (ed A. C. Zettlemoyer) (M. Dekker, New York, 1969).
49 Volmer, M. *Kinetik der phasenbildung*. (Steinkopff, 1939).
50 Poling, B. E., Prausnitz, J. M. & O'Connell, J. P. (McGraw-Hill, New York, 2001).

CHAPTER 3

Wettability engendered templated self-assembly (WETS) for fabricating multi-phasic particles

3.1. Introduction

Precise control over the geometry and chemistry of multi-phasic (monophasic, biphasic or Janus, tri-phasic, quad-phasic etc.) micro- and nano-particles is of significant importance for a wide range of applications including drug delivery,[1-3] vaccines and inhalation biotherapeutics,[4] biological sensors,[5] optical devices,[5] and nanomotors.[6] Further, in the bottom-up approach envisioned for building materials and devices of the future, it is necessary to develop precisely designed particles (building blocks) that can assemble in a preprogrammed manner to yield desired structures and properties.[7-14] However, typically, fabricated particles have a uniform distribution of all materials (isotropic). In order to design particles that self-assemble in a preprogrammed manner, it is essential to control the size, shape, and distribution of dissimilar materials within each particle to form anisotropic particles, such as Janus, tri-phasic, or quad-phasic particles.[7-11]

In addition, in case of medical therapies such as combinatorial treatment methods, which uses more than one medication to treat a disease, requires encapsulation and release of multiple drugs, ideally with independently controlled release kinetics. To address this challenge, nanoparticles with multiple compartments, each being made of distinct polymer phases encapsulating different drugs, would be very beneficial. However there hasn't been an easy way to fabricate monodisperse multi-phasic nanoparticles at large-scale while precisely controlling geometry and dimensions of the particles.

In past few decades, many strategies have been developed to fabricate multi-phasic particles. These include pickering emulsion method, electrohydrodynamic cojetting, photopolymerisation within microfluidic devices and Particle Replication on Non-wetting Template (PRINT) methods.[15-19] Although these techniques have been successful in fabricating specific types of multi-phasic particles, a simple and universal technique for the fabrication of mono-disperse, multi-phasic particles of any desired composition and size, with precise control over particle geometry has not been developed thus far. In this work, we have developed a facile technique termed WETS (Wettability Engendered Templated Self-assembly) which provides an unprecedented ability for the large scale manufacturing of monodisperse, multi-phasic particles possessing almost any projected shape, composition, modulus, and dimensions as small as 25 nm, using a simple dip-coating process.

3.2. Design principles

When a liquid comes in contact with a smooth homogenous surface, it can either wet the surface completely, or partially, making a finite equilibrium contact angle (θ_E) with the surface. The equilibrium contact angle is determined by the balance between the

solid-vapor (γ_{SV} or the surface energy), solid-liquid (γ_{SL}) and liquid-vapor (γ_{LV} or the surface tension) interfacial tensions acting at the three-phase contact line, and is given by Young's relation $\cos\theta_E = (\gamma_{SV} - \gamma_{SL})/\gamma_{LV}$.[20] The contact angles for a liquid as it advances or recedes from a smooth surface are called the advancing (θ_A) and receding (θ_R) contact angles respectively. When a substrate with a receding contact angle, $\theta_R = 0$ is pulled through a liquid, the substrate is coated with a uniform liquid film of finite thickness, controlled by the dip-coating velocity[21-24]. In contrast, when a partially wetting surface ($\theta_R > 0$) is dip-coated, the liquid film is unstable and dewets off the surface, leaving the surface completely dry[21-24]. Similarly, when a non-wettable (or low surface energy) surface patterned with wettable domains is dip-coated, the liquid wets and coats only the wettable (or high surface energy) domains and leaves the non-wettable surface completely dry[24-26].

Another important parameter to consider while dip-coating a patterned surface is that there is a maximum dip-coating velocity (critical velocity V_C) above which a liquid will not dewet off a surface, even if the surface exhibits a finite receding contact angle. This critical velocity depends on the viscosity (η) and surface tension (γ_{LV}) of the liquid, and is given by[23]:

(Equation 3.1) $V_C = k\frac{\gamma_{LV}}{\eta}\theta_E^3$

Here, *k* is proportionality constant. Below this critical dip-coating velocity, the liquid dewets off a non-wettable or partially wettable surface completely. The non-wettable surfaces developed in this work have high receding contact angles (θ_R > 20º), see Table 3.1) for different liquids and polymer solutions (including very low surface tension

liquids) used in this work. This leads to relatively high critical dip-coating velocities, typically in the range of several cm/sec.

Further, in case of liquid droplets that are in contact with both non-wettable surface (possessing low surface energy γ_{SV}) and a wettable surface (possessing high surface energy), as discussed in section 1.6, experiences a force driving the droplets to assemble preferentially within the wettable domains.

There have been several reports[25-28] on using surfaces with patterned wettability to engender the self-assembly of water (γ_{LV} ~ 72 mN/m), and water-based polymer solutions or dispersions. However, typically, it has been more difficult to self-assemble low surface tension organic liquids (such as alcohols, dimethylformamide, tetrahydrofuran, toluene etc.) or polymer solutions within patterned high surface energy domains.[29] This is because organic solvents and polymer solutions possess low surface tension values (γ_{LV} ~ 15 – 30 mN/m), and as a consequence they tend to wet and spread on both the high and low surface energy patterned domains, forming a film over the entire surface.

3.3. Experimental Procedure

3.3.1. Materials

Heptadecafluoro-1,1,2,2-tetrahydrodecyl)trichlorosilane (HDFTS) was purchased from Gelest Inc. Poly(vinylidene fluoride) (PVDF, with a weight-average molecular weight of $M_w \approx$ 275kDa) and polystyrene (PS, $M_w \approx$ 190kDa) were purchased from Scientific polymer products Inc. SU-8 (2010) purchased from MicroChem Corp. Poly(sodium 4-styrenesulfonate) (PSS, $M_w \approx$ 70 kDa), poly(ethyleneglycol)diacrylate (PEGDA, $M_w \approx$ 700Da), fluorescent dyes: rhodamine B, fluorescein isothiocyanate

isomer I (FITC), 4', 6-diamidino-2-phenylindole dihydrochloride (DAPI) and solvents: dimethylformamide (DMF), toluene, propylene glycol monomethyl ether acetate (PGMEA) and perfluorodecalin (PFD) were purchased from Sigma-Aldrich. Ferrofluid (EMG 304) was purchased from Ferrotec. Silicon wafers were obtained from the cleanroom (Lurie Nanofabrication Facility) at the University of Michigan.

3.3.2. Templates fabrication

A ~5 nm thin film of titanium dioxide (TiO_2) was deposited on to silicon wafers through e-beam evaporation. To make the TiO_2 surface non-wettable, the surface was exposed to HDFTS silane vapors at 100°C for 30 minutes. Next, the silanised TiO_2 surfaces were exposed to deep ultraviolet radiation (UV, 254 nm) for 90-120 minutes through a quartz photomask with desired patterns. The exposed TiO_2 domains through the photomask switched from non-wettable (low surface energy) to wettable (high surface energy). This gave us non-wettable templates with wettable domains possessing any desired geometry.

3.3.3. Nanotemplates fabrication

The WETS templates with wettable domains of 700 nm and 25 nm in diameter were fabricated using photolithography and block copolymer lithography, respectively. Here, we used standard photolithography, and a stepper (GCA AS200 Autostep), to obtain the photoresist mask with a uniform array of 700 nm holes on top of a silicon wafer. We used block copolymer lithography, using an asymmetric block copolymer, polystyrene-block-poly(methyl methacrylate) (PS-b-PMMA) forming cylindrical nanostructures (molecular weight: PS/PMMA – 46 kDa /21 kDa) to develop a polystyrene mask with 25 nm hexagonally packed holes array on top of a silicon wafer.

Next the Si wafers with the polymer masks were deposited with 5 nm (for 25 nm templates) and 15 nm (for 700 nm templates) thin TiO_2 through e-beam evaporation. Following TiO_2 deposition, the polymer masks were lifted off the surface in their respective solvents. This produced silicon substrates with TiO_2 nano-domains of diameter 700 nm, as well as substrates with TiO_2 nano-domains of diameter 25 nm. Then, the substrates were made non-wettable by exposing them to HDFTS vapors. Finally, the substrates were exposed to deep UV radiation. This increased the surface energy of the TiO_2 nano domains, while the rest of the silicon substrate remained non-wettable.

3.3.4. Polymer solutions for dip-coating

PSS, PVDF and PS solutions used for dip-coating were 15 wt% solutions of the polymers in deionized water, DMF and toluene, respectively. For the PS deposition within the 25 nm and 700 nm patterned domains we used low molecular weight polystyrene (molecular weight 2000 – 5000 Da). The sugar solution used was a 30wt% solution in water. PEGDA and SU-8 were used as received. We also used 80 wt% (SU-8 0.8) and 50 wt% (SU-8 0.5) solutions of SU-8 in PGMEA for additional depositions. For magnetic polymer dispersion, ferrofluid was added to SU-8 at 0.5 % (v/v). All solutions were dip-coated using a syringe pump (KD Scientific) at a constant dip-coating velocity in the range of 0.1 to 1 cm/sec.

3.3.4. Characterization techniques

3.3.4.1. Contact angle measurements

The contact angle measurements were conducted using a Ramé-Hart 200-F1 goniometer. All contact angles reported in this work were measured by advancing or receding a small volume of liquid (~ 2 μL) onto the surface using a 2 mL micrometer

syringe (Gilmont). At least three measurements were performed on each substrate. Typical error in measurements was ±2º.

3.3.4.2. Microscopy

Tapping-mode atomic force microscopy (AFM) was conducted using a Veeco Innova instrument. Veeco TESPA tips and Hi Res C probes were used for imaging. The surfaces were imaged using a Hitachi SU8000 ultra-high resolution scanning electron microscope (SEM) at 5 kV and an Olympus BX 51 fluorescent microscope. The multi-phasic particles were visualized using a FCLSM (Nikon A1 Confocal). Three different lasers, 405 nm laser, 488 nm Argon laser, and 533 nm Helium-Neon green (HeNeG) laser, were used to excite the dyes DAPI, FITC, and Rhodomine B respectively.

3.4. Results and discussion

3.4.1. Templates for wettability engendered templated self-assembly

There have been several reports[25-28] on using surfaces with patterned wettability to engender the self-assembly of water (γ_{LV} ~ 72 mN/m), and water-based polymer solutions or dispersions. However, typically, it has been more difficult to self-assemble low surface tension organic liquids (such as alcohols, dimethylformamide, tetrahydrofuran, toluene etc.) or polymer solutions within patterned high surface energy domains.[29] This is because organic solvents and polymer solutions possess low surface tension values (γ_{LV} ~ 15 – 30 mN/m), and as a consequence they tend to wet and spread on both the high and low surface energy patterned domains, forming a film over the entire surface.

In this work, we employed smooth, low surface energy, silanized, titanium dioxide (TiO_2) surfaces (see section 3.3.2) that possess finite receding contact angles (θ_R)

for both water and different low surface tension liquids (including fluorinated liquids), and patterned them with high surface energy domains ($\theta_R = 0$) of different shapes and sizes. Such surfaces serve as templates to engender the self-assembly of both aqueous and organic polymer solutions and dispersions (Table 3.1). We fabricated the patterned templates by irradiating the TiO_2 surfaces with deep UV light (254 nm) through a quartz photo-mask possessing any desired pattern (see Figure 3.1). Upon deep UV irradiation, the surface energy of TiO_2 surfaces in the unmasked regions increases significantly due to the photo-catalytic cleavage of the TiO_2 – silane bond.[28, 30, 31] This simple fabrication process gave us a non-wettable surface patterned with wettable domains defined by the mask geometry. When such templates are dip-coated with a polymer solution (or dispersion), the solution preferentially wets and self-assembles within the patterned wettable domains. Upon evaporation of the solvent, the polymer (or particles from a dispersion) deposits within the patterned high surface energy domains, conforming to their shape and size (see Figure 3.2 and 3.3).

We observe similar assembly of liquids within the patterned high surface energy domains for spin- or spray-coating. Further, this wettability-engendered templated self-assembly of polymers or particles works effectively with a wide variety of polymer solutions and dispersions (as listed in Table 3.1).

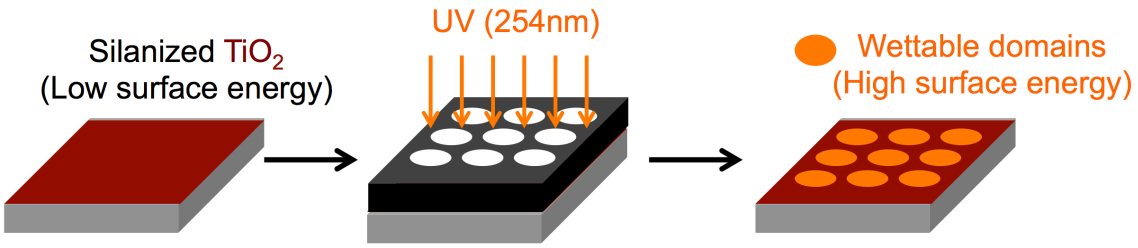

Figure 3.1. A schematic illustrating the fabrication of TiO_2 templates with patterned wettability.

3.4.2. Wettability engendered templated self-assembly (WETS) methodology

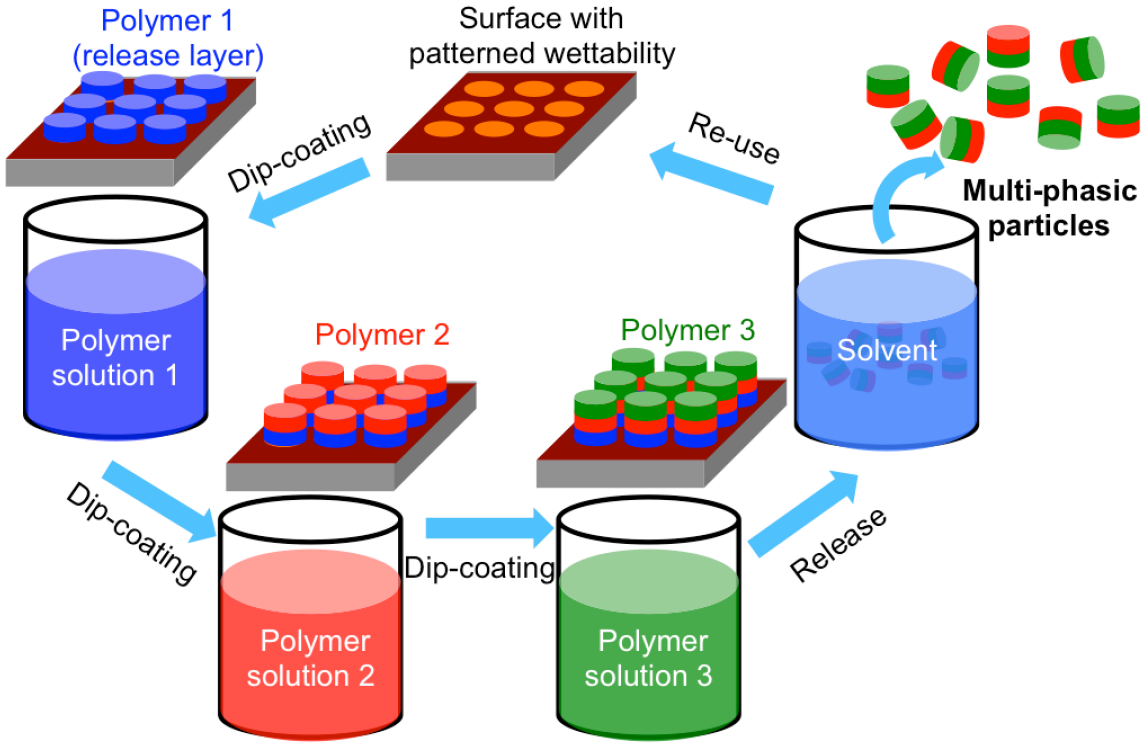

Figure 3.2. A schematic illustrating the WETS technique for fabricating multi-phasic particles.

Table 3.1 lists many of the different liquids and polymer solutions that demonstrated wettability engendered self-assembly within the patterned surfaces developed in this work. The table also lists the advancing and receding contact angles for all liquids on both the wettable and non-wettable regions of the patterned surfaces. All the polymer solutions used for contact angle measurements are 15 wt% solutions.

Table 3.1. Advancing (θ_A) and receding (θ_R) contact angles for over 30 different liquids and polymer solutions on the non-wettable and wettable regions of the patterned surfaces.

Liquids	Non-wettable surface		Wettable surface	
	θ_A	θ_R	θ_A	θ_R
Water	120°	112°	<10°	0°
Dimethylformamide (DMF)	76°	66°	<10°	0°
Toluene	72°	62°	<10°	0°
Ethanol	50°	38°	0°	0°
Hexane	47°	33°	0°	0°
Acetone	62°	47°	0°	0°
Methanol	52°	39°	0°	0°
Isopropanol	56°	42°	0°	0°
Tetrahydrofuran (THF)	66°	53°	0°	0°
Chloroform	64°	51°	0°	0°
Propylene glycol monomethyl ether acetate (PGMEA)	66°	57°	0°	0°
SU-8	68°	55°	0°	0°
PEGDA	85°	72°	<10°	0°
AK 225 (Fluorinated solvent)	28°	14°	0°	0°
Hexadecane	66°	53°	0°	0°

PSS-Water	108^{o}	97^{o}	<10^{o}	0^{o}
PVDF-DMF	72^{o}	59^{o}	<10^{o}	0^{o}
PS-Toluene	72^{o}	58^{o}	<10^{o}	0^{o}
PMMA-Toluene	70^{o}	57^{o}	<10^{o}	0^{o}
Sugar-Water	112^{o}	99^{o}	<10^{o}	0^{o}
PMMA-DMF	73^{o}	60^{o}	<10^{o}	0^{o}
PMMA-AK 225	32^{o}	17^{o}	0^{o}	0^{o}
PVDF-Acetone	66^{o}	52^{o}	0^{o}	0^{o}
Polydimethylsiloxane (PDMS)	30^{o}	15^{o}	0^{o}	0^{o}
Polyvinylalcohol (PVA)-Water	108^{o}	96^{o}	<10^{o}	0^{o}
SU-8-PGMEA	68^{o}	56^{o}	0^{o}	0^{o}
Polyisobutylene (PIB)-Hexane	50^{o}	32^{o}	0^{o}	0^{o}
PEGDA-DMF	78^{o}	68^{o}	<10^{o}	0^{o}
SU-8-DMF	70^{o}	59^{o}	<10^{o}	0^{o}
PVA-Ethanol	52^{o}	37^{o}	0^{o}	0^{o}
PIB-THF	53^{o}	39^{o}	0^{o}	0^{o}
PMMA-Chloroform	58^{o}	42^{o}	0^{o}	0^{o}

Thus, the WETS technique can serve as a facile, bottom-up approach to pattern a wide variety of polymers and particles with precise control over geometry. In addition, utilizing the WETS technique, we sequentially deposited multiple polymers and inorganic particles, one on top of another within the wettable domains, to fabricate multi-phasic assemblies. Upon releasing the multi-phasic assemblies from the template by dissolving away a pre-deposited sacrificial layer, we obtained multi-phasic particles with precisely controlled geometry and chemistry. After release of the particles from the template, the templates can be readily reused (over 20 times in our experiments) for fabricating a new batch of multi-phasic particles (see Figure 3.2), enabling a rapid, inexpensive, waste-free (significant when fabricating particles that encapsulate expensive biomolecules and drugs)[1] and easily reproducible method for manufacturing multi-phasic particles.

In order to demonstrate the fabrication of multi-phasic polymer particles using the WETS technique, we first deposited poly(sodium 4-styrenesulfonate) (PSS; using PSS in water solution) within the wettable domains (see Figure 3.3a), followed by poly(vinylidene fluoride) (PVDF; using PVDF in dimethylformamide solution) on top of PSS (see Figure 3.3b) and finally polystyrene (PS; using PS in toluene solution) on top of PVDF and PSS (see Figure 3.3c). Note that the preferential assembly of polymer solutions on top of the preceding polymer patterns is driven by the difference in receding contact angles between the polymer patterns and the non-wettable background (see Table 3.2). After depositing each polymer layer, we annealed the surfaces slightly above the glass transition temperature of the polymers to ensure good adhesion between the layers. We confirmed this sequential deposition of polymers, one on top of another, using

fluorescence microscopy and atomic force microscopy height measurements (see Figure 3.3a-3c, corresponding insets). Additional layers can be stacked within the wettable domains from other polymer solutions, as long as the solvents don't affect the already deposited polymer layers. The projected shape and size of the multi-phasic assemblies (PSS-PVDF-PS) can be precisely controlled by utilizing a patterned surface possessing the desired geometry as a template (see Figure 3.3d-3f).

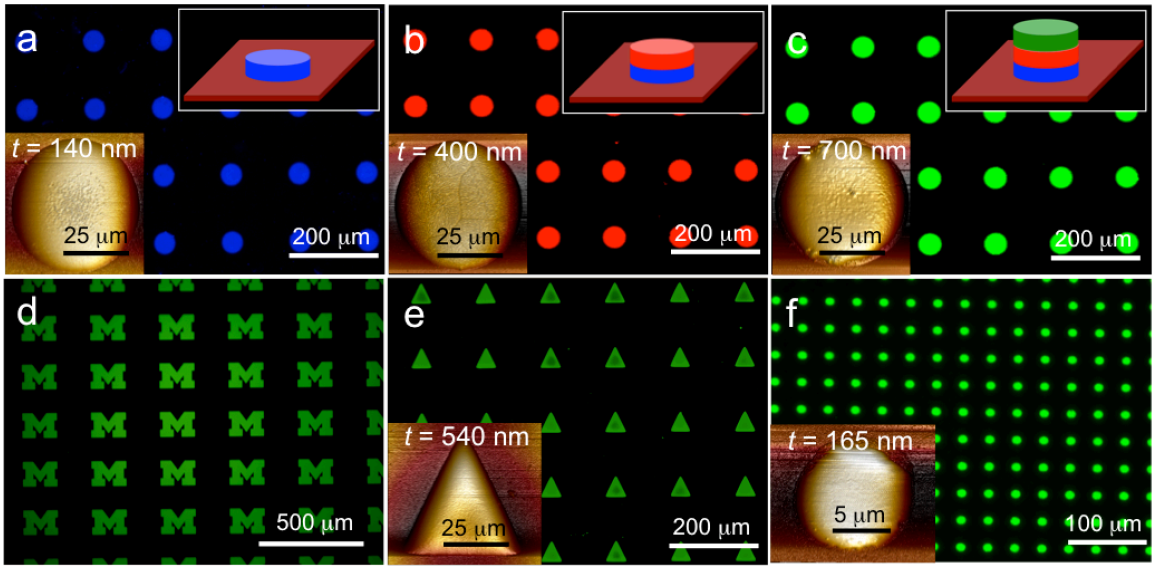

Figure 3.3. WETS enabled multi-phasic assemblies. Fluorescent micrographs showing wettability engendered assembly of (a) poly(sodium 4-styrenesulfonate) (PSS; dyed blue), (b) poly(vinylidene fluoride) (PVDF; dyed red) on top of PSS, and (c) (d) (e) and (f) polystyrene (PS; dyed green) on top of PVDF and PSS. The top insets in a-c show schematics of the polymer layers within the high surface energy (or wettable) domains. The bottom insets in a-c, e and f show the corresponding AFM height images and the thickness (*t*) of the polymer assembly.

Table 3.2. Receding contact angles (θ_R) for dip-coated polymer solutions on other polymers used in the fabrication of multi-phasic particles.

Polymer pattern	Polymer solution dip-coated	Receding contact angle (θ_R)
PSS	PVDF-DMF	0^o
	SU-8	0^o
	PEGDA	0^o
	SU-8-PGMEA	0^o
	PEGDA-DMF	0^o
	PMMA-Chloroform	0^o
	PS-Toluene	0^o
PVDF	PS-Toluene	0^o

3.4.3. Wettability engendered self-assembly of polymers within nanoscale wettable domains.

Further, the methodology works across a wide range of domain sizes. Figure 3.4 shows the assembly of PS, on top of SU-8, on top of PSS (see AFM measurements in Figure 3.4), within 700 nm domains. Fascinatingly, the WETS technique even extends to the sub-50 nm length scale (see AFM measurements in Figure 3.5). Figure 3.5d shows the assembly of PS, on top of SU-8, on top of sugar within patterned 25 nm wettable domains. The templates with 25 nm wettable domains were developed utilizing block-copolymer nanolithography (BCNL). BCNL was necessary to fabricate these monodisperse (~ 25 nm diameter) domains because the inherent diffraction limit of light precludes the use of common photolithographic techniques. BCNL is a scalable alternate

approach that utilizes molecular self-assembly processes to generate regular nanoscopic patterns, ~5 − 50 nm, in size.[32, 33].

To engender assembly of polymers within nanoscale wettable domains (of diameters 700 nm and 25 nm), we utilized non-wettable surfaces patterned with wettable TiO_2 nano domains (as shown in Figure. 3.4a, 3.4e and 3.5a, 3.5e) as templates. First, these templates were dip-coated with a sacrificial polymer layer. Here, we used PSS (15 wt% solution in water) and sugar layers (30 wt% solution in water) as sacrificial layers for templates possessing 700 nm and 25 nm wettable domains, respectively (see Fig. 3.4b, 3.4f and 3.5b, 3.5f). Next, the substrates were dip-coated with SU-8 and cross-linked using UV radiation (365nm). Subsequently, the substrates were dip-coated with polystyrene (molecular weight ~ 2000 – 5000 Da). This gave us polystyrene, SU-8 and sacrificial polymer layers stacked one upon another, within the wettable domains, as shown in Figure 3.4 and Figure 3.5. The substrates were annealed above the glass transition temperatures of the polymers after each polymer deposition. The AFM height images (Figure 3.4 and 3.5) show an increase in height after each polymer layer deposition within the wettable domains, indicating successful depositions of polymer layers one on top of another within the wettable domains.

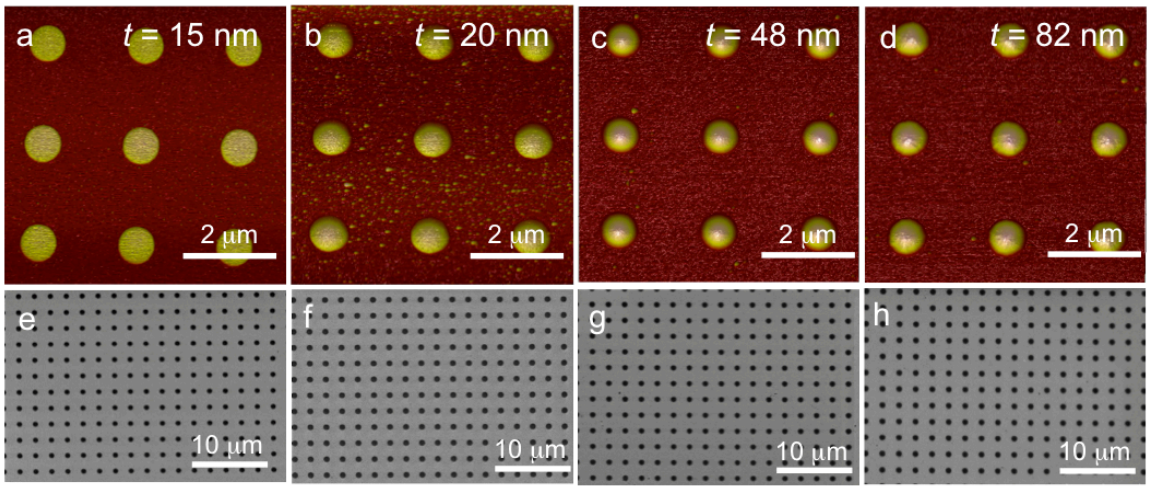

Figure 3.4. WETS for fabricating 700 nm multiphasic nanoparticles. AFM height images and thickness '*t*' for (a) High surface energy TiO_2 domains; (b) PSS deposited on top of the wettable TiO_2 domains; (c) SU-8 deposited on top of PSS; (d) Polystyrene deposited on top of SU-8 and PSS. Corresponding SEM images of (e) High surface energy TiO_2 domains; (f) PSS deposited within the wettable domains; (g) SU-8 deposited on top of PSS; and (h) Polystyrene deposited on top of SU-8 and PSS.

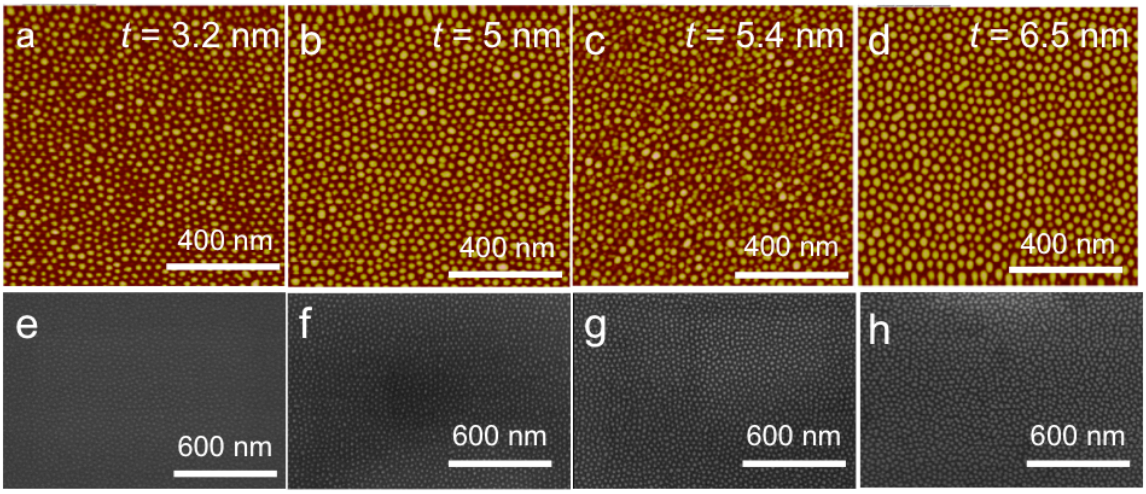

Figure 3.5. WETS for fabricating 25 nm multiphasic nanoparticles. AFM height images and thickness *t* of (a) High surface energy TiO_2 domains; (b) Sugar deposited on top of the wettable TiO_2 domains; (c) SU-8 deposited on top of Sugar; (d) Polystyrene deposited on top of SU-8 and sugar. Corresponding SEM images of (e) High surface energy TiO_2 domains; (f) Sugar deposited within the wettable domain; (g) SU-8 deposited on top of Sugar; and (h) Polystyrene deposited on top of SU-8 and sugar. The thickness '*t*' of the patterned domains is an average value across 30 domains. The variation in thickness across the domains is ~ ±0.5 nm. This highlights the uniformity in thicknesses for the particles fabricated using the WETS technique.

3.4.4. Tuning thickness of polymers deposited within wettable domains

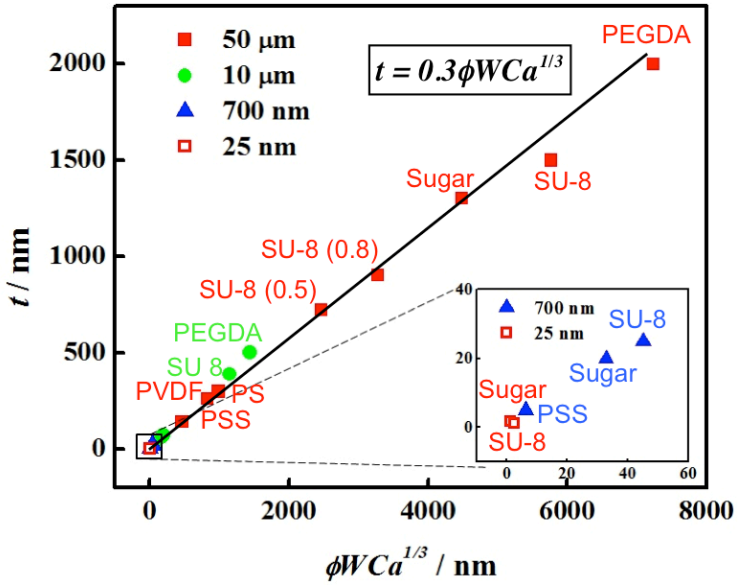

Figure 3.6. A plot comparing the predicted (solid black line) and measured (individual data points) thicknesses for a variety of polymers. The thickness t for the polymer depositions within patterned domains is an average value across 30 domains.

The thickness (t) of the liquid or polymer solution film deposited within the wettable domains of a patterned surface is dependent on the width of the wettable domain (W) and the capillary number ($Ca = \mu V/\gamma_{LV}$) for dip-coating. Here μ is the viscosity of the polymer solution, and V is the dip-coating velocity. The thickness of the polymer solution deposited within the wettable domain is given by $t = kWCa^{1/3}$ where k is a proportionality constant.[26] After the solvent has evaporated, the thickness of the polymer layer deposited within the wettable domain can be approximated as $t = k\phi WCa^{1/3}$, where ϕ is the volume fraction for the polymer in the solution. The thicknesses predicted using this approach matched well with our experimental thickness measurements (as shown in Figure 3.6) for different polymer solutions deposited within wettable domains, possessing a range of different sizes (25 nm – 50 μm). Using this understanding, it is possible to

directly control the specific thickness of each individual layer within the multiphasic particles to within a few nm of any desired value.

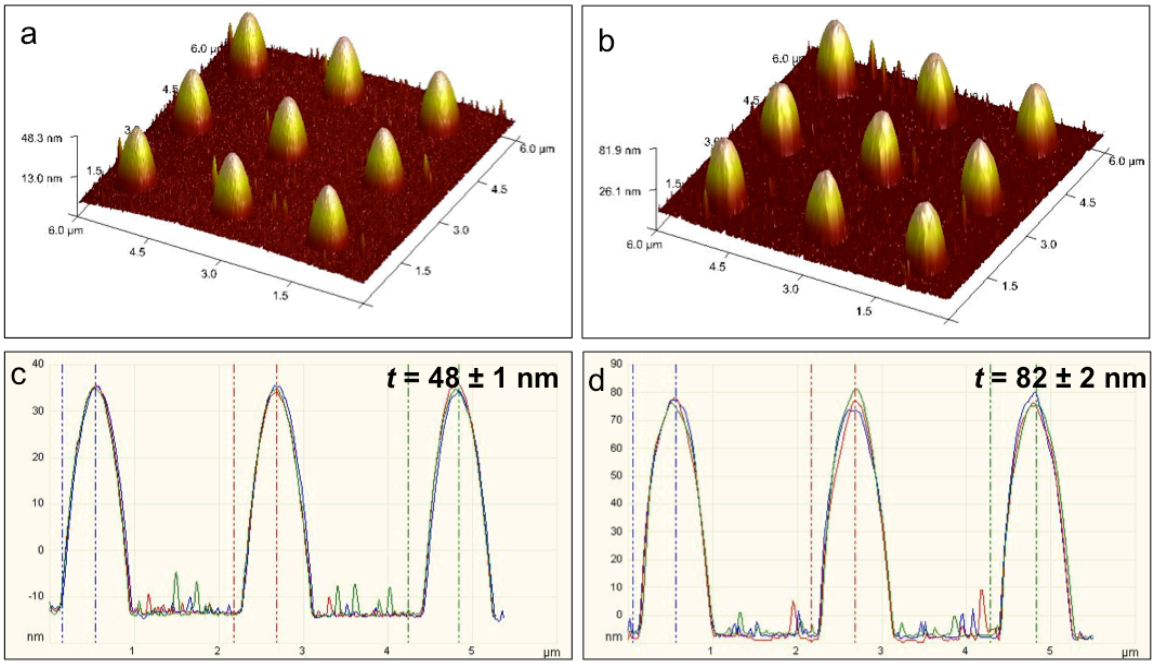

Figure 3.7. Variation in thickness of polymer depositions across different 700 nm TiO_2 wettable domains. (a) and (b) 3-Dimensional AFM height images of multi-phasic polymer assemblies shown in 5c and 5d respectively. (c) and (d) Height scan profiles of the different polymer assemblies shown in a and b respectively. The thickness '*t*' of the patterned domains is an average value across 30 domains. The variation in thickness across the domains is ~ ± 1 nm for bi-phasic (PSS–SU-8) and ± 2 nm for tri-phasic (PSS–SU-8–PS) polymer assemblies. This highlights the uniformity in thicknesses for the particles fabricated using the WETS technique.

The variation in thickness of the bi-phasic (PSS–SU-8–PS) and tri-phasic (PSS–SU-8–PS) polymer assemblies deposited within 700 nm wettable domains, is ±1 nm and ±2 nm respectively (Figure 3.7). The thickness (*t*) values reported for the particles here correspond to the thicknesses measured at the center of the particle. The thickness profile for the polymer solutions deposited within the wettable domains is convex due to the liquid droplet morphology. However, upon evaporation of solvent, the thickness profile of the polymers deposited within the patterned domains can be either convex or flat or

concave (coffee-ring effect) shaped depending on the solvent evaporation rate and contact-line pinning[34]. The assembled multi-phasic particles can be released upon dissolving the sacrificial polymer layer (PSS) in water. In this manner, the WETS technique allows for the fabrication of a wide variety of monodisperse, multi-phasic particles with precise control over the size, projected shape, composition, thickness, and placement of the different polymer phases within the particle.

3.4.5. Multi-phasic amphiphilic particles in different shapes and sizes

We also fabricated multi-phasic particles by utilizing cross-linkable oligomers. The cross-linkable oligomers offer the freedom to deposit multiple layers using the same polymer solution without any detrimental effects on the already deposited layers. Here, we chose one of the cross-linkable oligomers to be hydrophobic (SU-8) and the other to be hydrophilic (poly(ethyleneglycol)diacrylate, PEGDA) in order to impart amphiphilicity to the cross-linked multi-phasic particles. To fabricate these amphiphilic particles, first PSS patterned templates were dip-coated with SU-8 and cross-linked with UV irradiation (365 nm). Next, the templates were dip-coated with a mixture of PEGDA and its cross-linker (Darocur 1173) and also cross-linked with UV irradiation (365 nm). This process resulted in bi-phasic amphiphilic assemblies deposited on top of PSS within the patterned domains (see Figure 3.8). The amphiphilic particles were subsequently released from the templates by dissolving the PSS sacrificial layer in water (see Figure 3.9). By changing the volume fraction of the cross-linker, it was easy to control the modulus of each individual phase within the amphiphilic particles.[35] Precise control over the modulus[35, 36] and projected shape[1, 2, 4, 35-37] of the fabricated particles can be critical in developing drug carriers with enhanced circulation times and enabling their accumulation

within specific target sites. Figure 3.9 show PEGDA–SU-8 amphiphilic particles of different shapes, fabricated using the WETS technique.

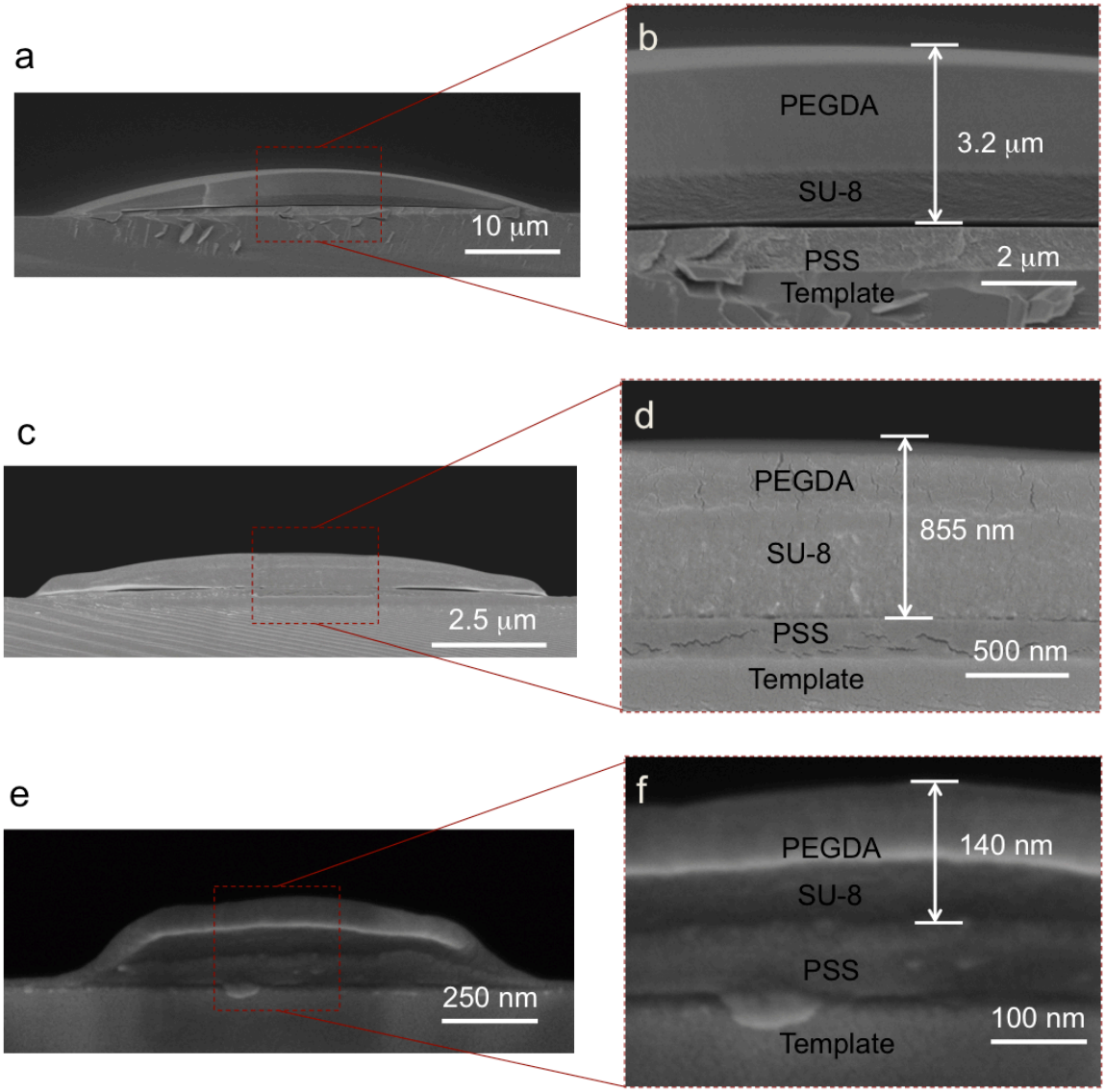

Figure 3.8. Cross-section SEM images of multi-phasic assemblies. (a), (c), (e) SEM cross-section images showing sequential deposition of SU-8 and PEGDA on top of the scarifical layer PSS within wettable domains of diameter 50 μm (a) 10 μm (c) and 1.5 μm (e). (b) (d) (f) show higher magnification images of the area indicated by the dashed red square shown in a, c, e.

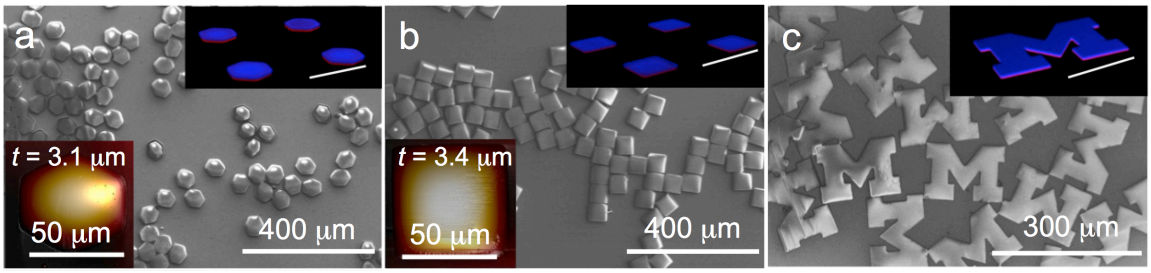

Figure 3.9. Multi-phasic particles of different shapes fabricated using the WETS technique. (a)-(c) SEM images of the released bi-phasic amphiphilic particles comprising SU-8 and PEGDA polymers of hexagon (a) square (b), complex shapes (c) and circular shapes of diameter 50 μm. The top insets show corresponding 3-D stacked fluorescence confocal microscopy images of the particles before release. SU-8 is dyed red and PEGDA is dyed blue. Scale bars for the top insets in a-c represent 100 μm. The bottom insets in a and b show the corresponding AFM height images and thickness (*t*) of the released particles.

Figure 3.10 show different circular biphasic (PEGDA – SU-8) particles, of different dimensions, fabricated in this work. Cross-sectional SEM images of the multi-phasic assemblies in different sizes clearly highlight the distinct phases comprising the multi-phasic particles (see Figure 3.8 and Figure 3.10). We also fabricated bi-phasic, polymer nanoparticles with diameters as small as 25 nm (see Figure 3.10d) by releasing the multi-phasic polymer assemblies shown in Figure 3.5d and 5h. While there have been a few previous reports[38, 39], in general it has been extremely difficult to fabricate organic nanoparticles of desired chemistry possessing all dimensions below 50 nm.[16, 35] Thus, although various inorganic nanoparticles, possessing different shapes, and with all dimensions below 30 nm are commercially available, even single-phase organic nanoparticles possessing similar dimensions are not. To the best of our knowledge, the WETS technique is the only methodology that allows for the fabrication of monodisperse, multiphasic particles of essentially any projected shape, composition, and dimensions as small as 25 nm. Particles within the size range of 10-100 nm, when used as drug carriers, exhibit high circulation time in blood and provide high tumor accumulation.[1, 2, 36] In

addition, we fabricated hybrid, organic-inorganic, bi-phasic particles with SU-8, and SiO_2 nanoparticles (see Figure 3.11).

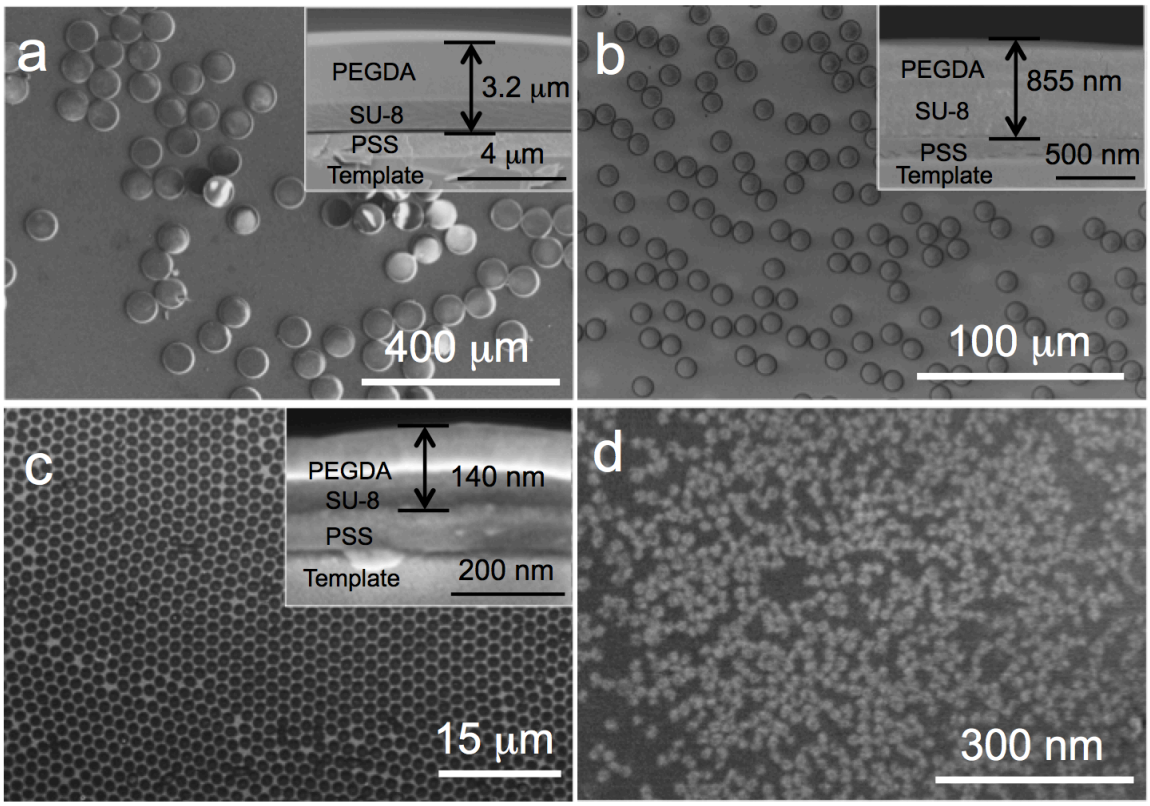

Figure 3.10 Multi-phasic particles of different sizes fabricated using the WETS technique. (a)-(d) SEM images of the released bi-phasic amphiphilic particles comprising SU-8 and PEGDA polymers of circular shapes of diameter 50 μm (d), 10 μm (e) and 1.5 μm (f). (g) SU-8–PS biphasic polymeric nanoparticles, 25 nm in diameter. The top insets in a-c show the corresponding SEM cross-section images of the multi-phasic particles before release.

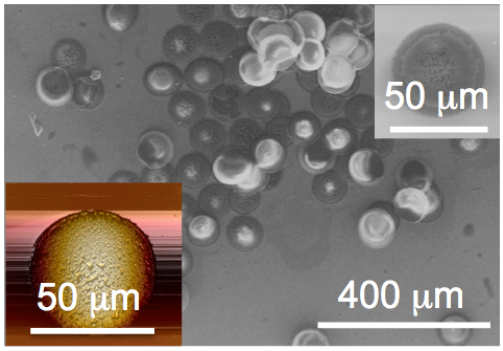

Figure 3.11 Inorganic-organic bi-phasic WETS particles composed of SU 8 polymer and SiO_2 nanoparticle (~500 nm) layers. The bottom inset shows AFM height image of the bi-phasic particle.

3.4.6. Fabrication of Hexaphasic particles

Furthermore, we stacked up to 6 polymer layers, comprising alternate layers of hydrophobic and hydrophilic phases, within the wettable domains (see Figure 3.12). Cross-sectional SEM images of the multi-phasic assembly clearly show the deposition of alternating SU-8 and PEGDA layers on top of PSS. Note that we can independently tailor the thickness of each layer within the hexa-phasic particles. The assembled tri-phasic and hexa-phasic particles were released from the template (see Figure 3.12m and 3.12n) by dissolving the sacrificial polymer (PSS) layer in water. Such multi-phasic particles, if formulated with alternating layers of a biodegradable polymer and a pharmacologically active agent, with precisely controlled thicknesses, may be ideal for the controlled and sustained delivery of drug molecules at the optimal rate and dose regimen, over several days.[3]

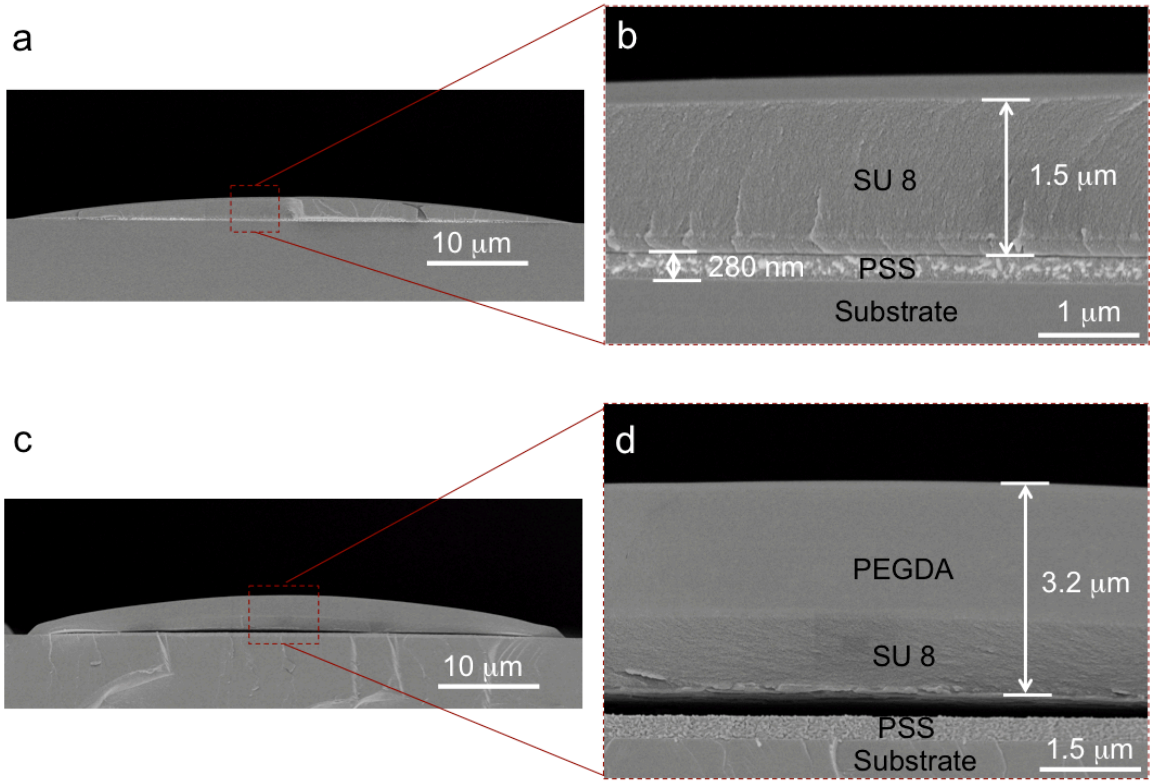

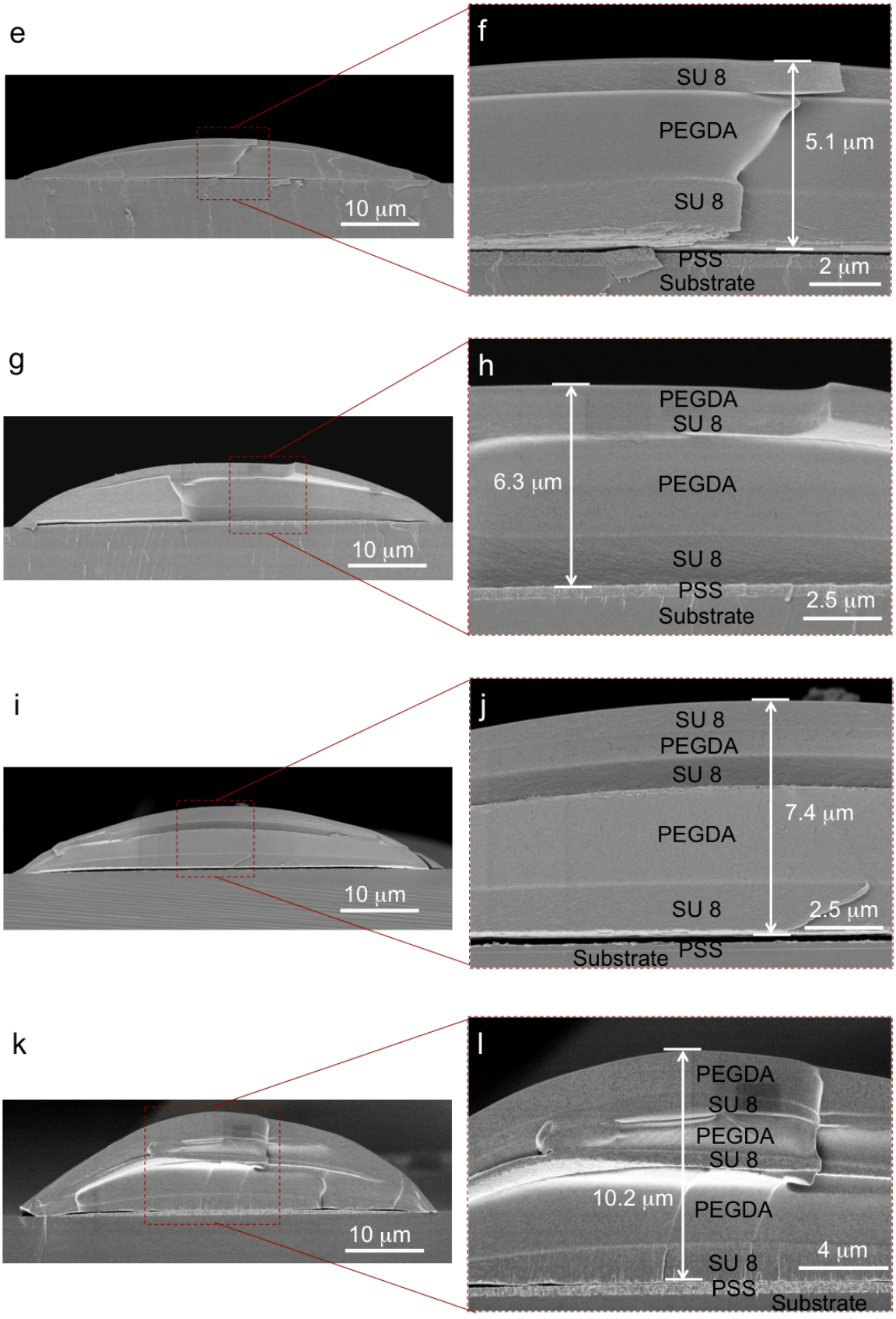
e
10 μm
f
SU 8
PEGDA
SU 8
PSS
Substrate
5.1 μm
2 μm
g
10 μm
h
PEGDA
SU 8
6.3 μm
PEGDA
SU 8
PSS
Substrate
2.5 μm
i
10 μm
j
SU 8
PEGDA
SU 8
PEGDA
SU 8
PSS
Substrate
7.4 μm
2.5 μm
k
10 μm
l
PEGDA
SU 8
PEGDA
SU 8
10.2 μm
PEGDA
SU 8
PSS
Substrate
4 μm

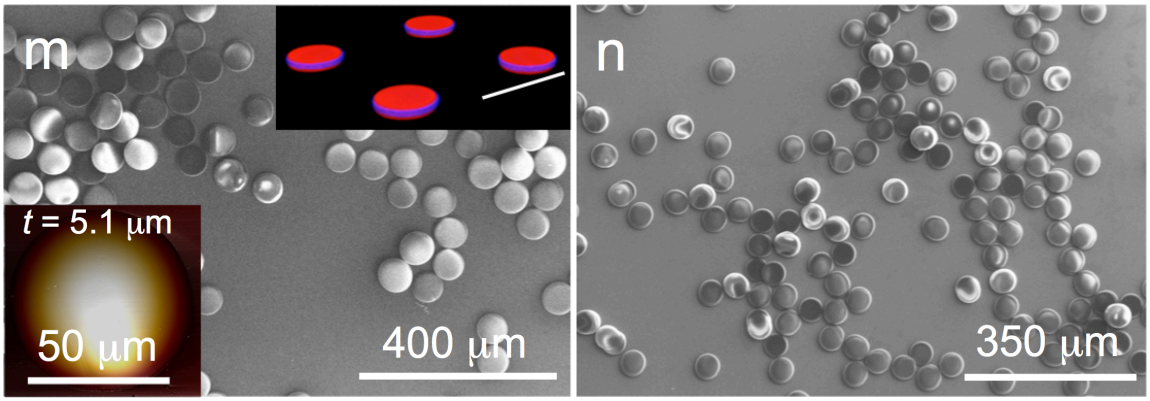

Figure 3.12 Fabrication of hexa-phasic particles. (a), (c), (e), (g), (i), (k) SEM images showing the cross section after sequential polymer depositions within a single wettable circular-shaped domain (50 mm in diameter). These images distinctly show the deposition of six alternating layers of SU-8 and PEGDA, on top of the sacrificial PSS layer. (b), (d), (f), (h), (j), (l) show high magnification images of the area indicated by the dashed red square shown in a, c, e, g, i, k respectively. (m) released hexa-phasic particles upon the dissolution of the sacrificial PSS layer. (n) SU-8–PEGDA–SU-8 tri-phasic particles. The top inset in n shows corresponding 3-D stacked fluorescence confocal microscopy images of the particles before release. SU-8 is dyed red and PEGDA is dyed blue. Scale bar for the top inset in n represent 100 μm. The bottom insets in n shows the corresponding AFM height images and thickness (*t*) of the released particles.

3.4.7. Fabrication of multifunctional particles

The multiple phases within the particles may be independently loaded with different cargos to provide the particles with multi-functional capabilities. Such particles can be beneficial in developing multi-functional therapeutic systems,[1, 2, 35, 36] as they can encapsulate multiple drugs simultaneously. It is also possible for the different drugs to possess different, independently controlled release kinetics, depending on the degradation/swelling behavior of their respective encapsulant phases in the target environment. In addition, some of the particle phases can be loaded with functional nanoparticles or molecules to aid in the imaging and transportation of the particles within a biological system using an external field.[40] For example, as shown in Figure 3.13, we have developed tri-phasic particles integrated with three different functionalities. Here,

the first phase is SU-8 loaded with magnetite nano-particles, second phase is SU-8 loaded with a fluorescent red dye, and the third phase is a hydrogel (cross-linked PEGDA). Such tri-phasic particles can function as drug carriers (hydrogel phase) that are easy to track (fluorescent imaging) and manipulate using a magnetic field to evade biological hurdles, and guide towards the target site. Figure 3.13d shows the trajectory of the motion of the particles upon application of the field in different directions.

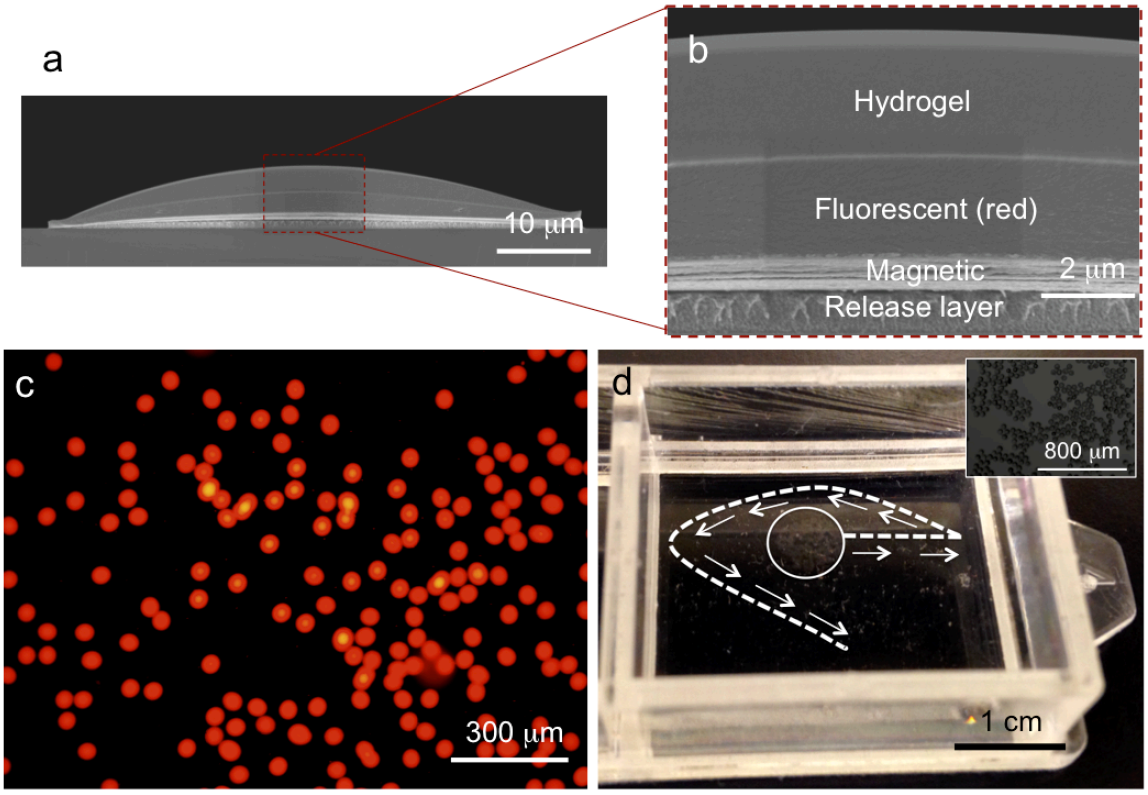

Figure 3.13. Multi-functional particles fabricated using the WETS technique. (a) A cross-sectional SEM image of a tri-functional particle comprising magnetic, fluorescent and hydrogel phases. (b) shows higher magnification image of the area indicated by the dashed red square shown in a. (c) shows a fluorescent microscope image of the tri-functional particles, released from the WETS template. (d) A cluster of tri-functional particles on a water surface. The cluster was transported along the trajectory indicated by the white dashed line using an external magnetic field. The inset is a higher magnification optical micrograph of the particle cluster indicated by the white circle in d.

3.4.8. Two dimensional self-assembly of amphiphilic particles

We have also studied the two-dimensional self-assembly of the fabricated bi-phasic amphiphilic particles at an oil-water interface. First, we added the amphiphilic particles to oil-water mixture and agitated the system vigorously through sonication. Then, the amphiphilic particles were allowed to settle at the oil-water interface. Further, we have used a vibrating stage to induce in-plane movement of the particles. The frequency and amplitude of the vibrations were adjusted to bring the particles close to one another, and to break misaligned particle aggregates. The bi-phasic amphiphilic particles assembled into close packed structures with the hydrophobic phase (SU-8) preferentially oriented towards the oil layer, and the hydrophilic phase (PEGDA) towards the water layer. The assembled structures grew in size with time (see Figure 3.14). This assembly of particles is driven by the minimization of interfacial free energy at the oil-water interface.[41] Figure 3.15 shows that the self-assembled close packed structures obtained were defined by the geometry (circle, square and hexagon shapes) of the amphiphilic building blocks. These results illustrate the utility of the WETS technique for developing a variety of amphiphilic building blocks that are expected to be of importance for fundamental studies on particle self-assembly, as well as, the bottom-up approaches envisioned to build materials and devices of the future.

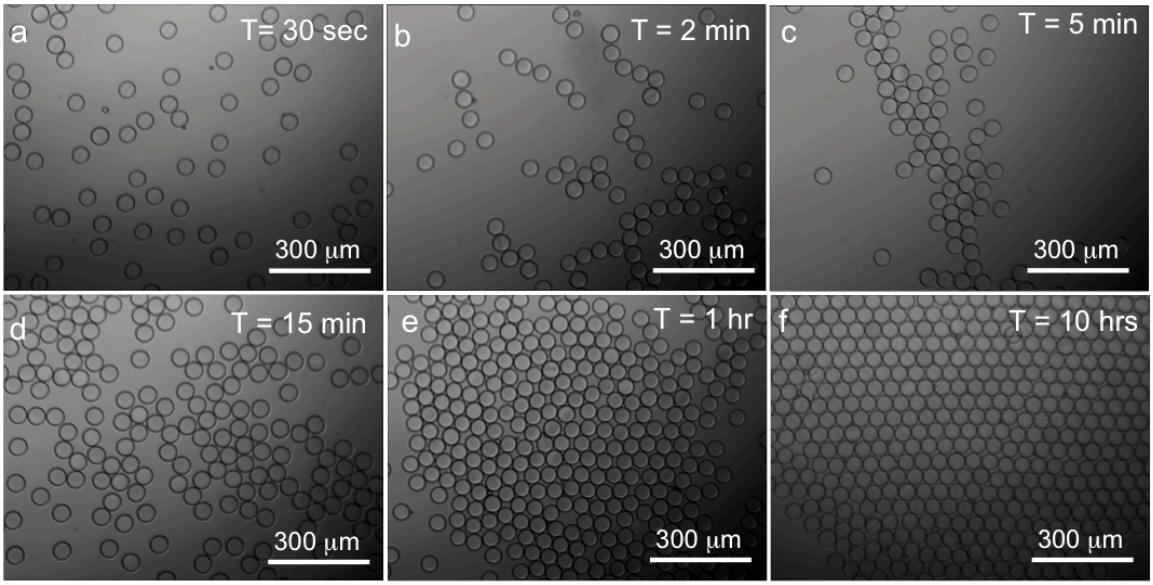

Figure 3.14. Assembly of SU-8–PEGDA biphasic particles at an oil-water interface. Optical microscopy images taken at times (a) T= 30 sec (b) T= 2 min (c) T= 5 min (d) T= 15 min (e) T= 1 hr and (f) T= 10hrs.

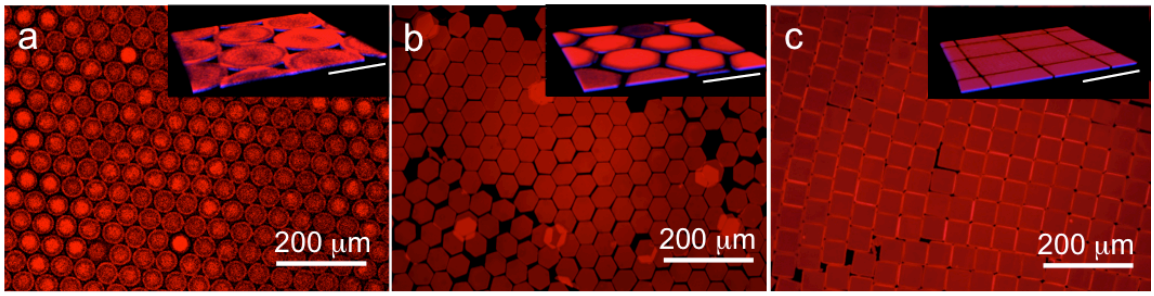

Figure 3.15. Two-dimensional self-assembly of amphiphilic particles. Self-assembled, close packed structures at an oil-water interface formed by (a) circle-shaped (b) hexagon-shaped, and, (c) square-shaped, bi-phasic amphiphilic particles. The top insets show corresponding 3-D stacked fluorescence confocal microscopy images of the assemblies. Scale bars in the insets represent 50 μm.

3.5. Conclusions

In conclusion, we have demonstrated that the WETS technique can be used to fabricate a wide variety of monodisperse, multi-phasic particles in complex shapes, and sizes as small as 25 nm, while maintaining control over the thickness, composition, and modulus of each particle phase. We have also fabricated a range of multi-phasic, amphiphilic particles that are anisotropic in both geometry and chemistry. We have further demonstrated the utility of the WETS technique in developing multi-functional nanoparticles and cargo carriers that are of significant importance in developing drug carriers with controlled release kinetics, increased circulation half-life, and enhanced targeting efficacy.

3.6. References

1. Caldorera-Moore, M., Guimard, N., Shi, L. & Roy, K. Designer nanoparticles: incorporating size, shape and triggered release into nanoscale drug carriers. *Expert opinion on drug delivery* **7**, 479-495 (2010).
2. Hubbell, J.A. & Chilkoti, A. Nanomaterials for drug delivery. *Science* **337**, 303-305 (2012).
3. Soppimath, K.S., Aminabhavi, T.M., Kulkarni, A.R. & Rudzinski, W.E. Biodegradable polymeric nanoparticles as drug delivery devices. *J Control Release* **70**, 1-20 (2001).
4. Mack, P.H., K.; Garcia, A.; Tully, J.; Maynor, B.; Particle Engineering for Inhalation Formulation and Delivery of Biotherapeutics. *Inhalation* **August 2012** (2012).
5. McConnell, M.D., Kraeutler, M.J., Yang, S. & Composto, R.J. Patchy and Multiregion Janus Particles with Tunable Optical Properties. *Nano Letters* **10**, 603-609 (2010).
6. Valadares, L.F. et al. Catalytic Nanomotors: Self-Propelled Sphere Dimers. *Small* **6**, 565-572 (2010).
7. Cheng, Q.F. et al. Janus interface materials: superhydrophobic air/solid interface and superoleophobic water/solid interface inspired by a lotus leaf. *Soft Matter* **7**, 5948-5951 (2011).
8. Glotzer, S.C. Some assembly required. *Science* **306**, 419-420 (2004).
9. Zhang, Z.L. & Glotzer, S.C. Self-assembly of patchy particles. *Nano Lett* **4**, 1407-1413 (2004).
10. Dendukuri, D., Hatton, T.A. & Doyle, P.S. Synthesis and self-assembly of amphiphilic polymeric microparticles. *Langmuir* **23**, 4669-4674 (2007).
11. Whitesides, G.M. & Boncheva, M. Beyond molecules: Self-assembly of mesoscopic and macroscopic components. *P Natl Acad Sci USA* **99**, 4769-4774 (2002).
12. Tang, Z.Y., Kotov, N.A. & Giersig, M. Spontaneous organization of single CdTe nanoparticles into luminescent nanowires. *Science* **297**, 237-240 (2002).
13. Jones, M.R. & Mirkin, C.A. Materials Science Self-Assembly Gets New Direction. *Nature* **491**, 42-43 (2012).
14. Walther, A. & Muller, A.H.E. Janus Particles: Synthesis, Self-Assembly, Physical Properties, and Applications. *Chem Rev* **113**, 5194-5261 (2013).
15. Roh, K.H., Martin, D.C. & Lahann, J. Biphasic Janus particles with nanoscale anisotropy. *Nat Mater* **4**, 759-763 (2005).
16. Wang, J.Y., Wang, Y.P., Sheiko, S.S., Betts, D.E. & DeSimone, J.M. Tuning Multiphase Amphiphilic Rods to Direct Self-Assembly. *J Am Chem Soc* **134**, 5801-5806 (2012).
17. Dendukuri, D., Pregibon, D.C., Collins, J., Hatton, T.A. & Doyle, P.S. Continuous-flow lithography for high-throughput microparticle synthesis. *Nat Mater* **5**, 365-369 (2006).
18. Bhaskar, S., Hitt, J., Chang, S.W.L. & Lahann, J. Multicompartmental Microcylinders. *Angew Chem Int Edit* **48**, 4589-4593 (2009).

19. Hong, L., Jiang, S. & Granick, S. Simple method to produce Janus colloidal particles in large quantity. *Langmuir* **22**, 9495-9499 (2006).
20. Young, T. An Essay on the Cohesion of Fluids. *Philos. Trans. R. Soc. London* **95**, 65 (1805).
21. Snoeijer, J.H. & Andreotti, B. Moving Contact Lines: Scales, Regimes, and Dynamical Transitions. *Annu Rev Fluid Mech* **45**, 269-292 (2013).
22. Blake, T.D. & Ruschak, K.J. A maximum speed of wetting. *Nature* **282**, 489-491 (1979).
23. Degennes, P.G. Deposition of Langmuir-Blodgett Layers. *Colloid Polym Sci* **264**, 463-465 (1986).
24. Kobaku, S.P.R. et al. Wettability Engendered Templated Self-assembly (WETS) for Fabricating Multiphasic Particles. *Acs Appl Mater Inter* **7**, 4075-4080 (2015).
25. Huang, Z.Y., Wang, P.C., MacDiarmid, A.G., Xia, Y.N. & Whitesides, G. Selective deposition of conducting polymers on hydroxyl-terminated surfaces with printed monolayers of alkylsiloxanes as templates. *Langmuir* **13**, 6480-6484 (1997).
26. Darhuber, A.A., Troian, S.M., Davis, J.M., Miller, S.M. & Wagner, S. Selective dip-coating of chemically micropatterned surfaces. *J Appl Phys* **88**, 5119-5126 (2000).
27. Zhao, B., Moore, J.S. & Beebe, D.J. Surface-directed liquid flow inside microchannels. *Science* **291**, 1023-1026 (2001).
28. Lai, Y.K. et al. Bioinspired Patterning with Extreme Wettability Contrast on TiO2 Nanotube Array Surface: A Versatile Platform for Biomedical Applications. *Small* **9**, 2945-2953 (2013).
29. Kobaku, S.P.R., Kota, A.K., Lee, D.H., Mabry, J.M. & Tuteja, A. Patterned Superomniphobic-Superomniphilic Surfaces: Templates for Site-Selective Self-Assembly. *Angew Chem Int Edit* **51**, 10109-10113 (2012).
30. Fujishima, A., Zhang, X.T. & Tryk, D.A. TiO2 photocatalysis and related surface phenomena. *Surf Sci Rep* **63**, 515-582 (2008).
31. Linsebigler, A.L., Lu, G.Q. & Yates, J.T. Photocatalysis on Tio2 Surfaces - Principles, Mechanisms, and Selected Results. *Chem Rev* **95**, 735-758 (1995).
32. Park, S. et al. Macroscopic 10-Terabit-per-Square- Inch Arrays from Block Copolymers with Lateral Order. *Science* **323**, 1030-1033 (2009).
33. Park, M., Harrison, C., Chaikin, P.M., Register, R.A. & Adamson, D.H. Block copolymer lithography: Periodic arrays of similar to 10(11) holes in 1 square centimeter. *Science* **276**, 1401-1404 (1997).
34. Cawse, J.N. et al. Combinatorial chemistry methods for coating development V: generating a combinatorial array of uniform coatings samples. *Prog Org Coat* **47**, 128-135 (2003).
35. Perry, J.L., Herlihy, K.P., Napier, M.E. & Desimone, J.M. PRINT: A Novel Platform Toward Shape and Size Specific Nanoparticle Theranostics. *Accounts Chem Res* **44**, 990-998 (2011).
36. Mitragotri, S. & Stayton, P. Organic nanoparticles for drug delivery and imaging. *MRS Bulletin* **39**, 219-223 (2014).

37. Yoo, J.W., Doshi, N. & Mitragotri, S. Endocytosis and Intracellular Distribution of PLGA Particles in Endothelial Cells: Effect of Particle Geometry. *Macromol Rapid Comm* **31**, 142-148 (2010).
38. Groschel, A.H. et al. Guided hierarchical co-assembly of soft patchy nanoparticles. *Nature* **503**, 247-+ (2013).
39. Groschel, A.H. et al. Precise hierarchical self-assembly of multicompartment micelles. *Nat Commun* **3** (2012).
40. Nunes, J., Herlihy, K.P., Mair, L., Superfine, R. & DeSimone, J.M. Multifunctional Shape and Size Specific Magneto-Polymer Composite Particles. *Nano Lett* **10**, 1113-1119 (2010).
41. Bowden, N., Terfort, A., Carbeck, J. & Whitesides, G.M. Self-assembly of mesoscale objects into ordered two-dimensional arrays. *Science* **276**, 233-235 (1997).

CHAPTER 4

Fabrication of charged biocompatible multilayered WETS particles

4.1. Introduction

Polymeric micro- and nanoparticles have been widely investigated for a broad range of biomedical applications, in particular for drug delivery systems[1-5]. Polymeric nanoparticles offer many advantages as drug carriers, including encapsulation, targeting efficiency and sustained release of drugs at a diseased site[3-5]. The drug delivery efficiency of the nanoparticles is governed by the composition, size, shape, surface charge and chemistry of the particles[1-5]. It is necessary to precisely control the different characteristics of the fabricated nanoparticles to develop efficient nanoparticle drug delivery systems. In addition, combinatorial therapy, aimed at inducing synergism would require encapsulation and release of multiple drugs at diseased sites, ideally with independently controlled release kinetics[3, 6, 7]. To address this challenge, nanoparticle drug-carriers should have multiple compartments that can encapsulate and deliver different drugs simultaneously[3, 6, 7]. Also given the differences in physio-chemical properties of the therapeutic moieties to be delivered, it is necessary that the nanoparticle

drug carriers possess compartments of different chemistries (Eg, Hydrophobic, Hydrophilic, charged polymers etc) and physical properties. However there hasn't been a easy route to fabricate monodisperse multi-layered nanoparticles at large-scale with precise control over composition, geometry and dimensions of the particles[3].

In our recent work, we have developed one of the simplest methodologies termed WETS to fabricate multiphasic particles of desired composition with precise control over size and shape of the particles[8]. Using WETS technique, we have fabricated a wide range of multi-phasic particles (comprising polymers such as polyethyleneglycoldiacrylate, polylacticglycolide polystyrene, polyvinylidenedifluoride etc). While these particles are capable of encapsulating a wide variety of drug molecules and diagnostic agents simultaneously, they are not ideally suited for encapsulation of highly charged therapeutic molecules such as small interfering RNA (siRNA)[9-11]. In theory, appropriately designed siRNA can silence nearly any gene in the body, giving it a broader therapeutic potential than typical small molecule drugs. Further, co-delivery of siRNA and chemotherapeutic drugs holds a great potential of treating specific tumor types that have been resistant to available therapies, such as triple-negative breast cancers[9-11]. Combining genetic targeting of specific resistant pathways of tumor cells with corelease of chemotherapetutic drugs can prove successful in 'turning off' the ability of tumor cells to fight/recover from a given chemotherapy. Thus, it would be beneficial to develop multi-layered particles comprising both charged as well as neutral polymeric layers, which are capable of encapsulating both charged macromolecules as well as hydrophobic chemotherapeutic drugs. So, in this work, we demonstrate a simple strategy to assemble charged multi-layered polyelectrolyte (PEL) films on to polymeric particles

(Polymer-PEL). Such particles are capable of incorporating broad range of therapeutics such as small molecule drugs, proteins and nucleic acids within polyelectrolyte nano layers, in addition to the drugs or diagnostic agents encapsulated within the core nanoparticle[6, 7, 10, 12, 13]. In addition, PEL assembly on to nanoparticles has shown to improve systemic circulation lifetime of drug carriers, reduce off-target drug delivery and also allows us to control the cellular internalization kinetics[6, 7, 12, 14].

Polyelectrolyte films are assembled on to bulk solid surfaces through Layer-by-Layer (LbL) adsorption process. This process typically involves dip-coating a surface of interest consecutively in polycationic and polyanionic aqueous solutions and each PEL deposition is followed by a washing step. While LbL process is a well characterized, automated and highly reproducible technique on bulk surfaces, the LbL assembly of PELs on to nanoparticles is very time-consuming process and involves multiple centrifugation and purification steps[1, 2, 10, 12]. To address this challenge, several alternate techniques have been developed including surface acoustic wave atomization[15], membrane filtration[16] and microfluidic methods[17-19]. Though these techniques avoid time-consuming centrifugation steps, it is difficult to scale up these techniques for high throughput fabrication of PEL-polymer particles. To utilize multilayered PEL-Polymer particles for medical applications, it is highly desirable to develop an easy-to-fabricate, high throughput methodology, ideally that uses similar dip-coating procedures that have been well characterized for bulk substrates.

For large-scale fabrication of multilayered Polymer-PEL particles, it would be advantageous to utilize template based techniques that localize polymer particles in well defined arrays on a substrate, in turn enabling standard LbL process on the particle arrays

using dip-coating or spray-coating methodologies. This has been achieved recently using spray-assisted LbL process on Particle Replication on Non-wetting Templates (PRINT) particles[14]. In a similar fashion, here we report an alternate, rapid and inexpensive WETS methodology to fabricate multi-layered Polymer-PEL particles of different shapes and sizes using simple dip-coating procedures.

4.2. Experimental Procedure

4.2.1. Materials

Heptadecafluoro-1,1,2,2-tetrahydrodecyl)trichlorosilane (HDFTS) was purchased from Gelest Inc. Polymers: poly(4-vinylphenol) (PVP, with a weight average molecular weight of $M_w \approx$ 25 kDa), Poly(*D,L*-lactide-co-glycolide) (PLGA, $M_w \approx$ 24-38 kDa, lactide:glycolide 50:50, acid terminated), Poly(sodium 4-styrenesulfonate) (PSS, $M_w \approx$ 70 kDa), Poly(allylaminehydrochloride) (PAH, $M_w \approx$ 15 kDa), fluorescent dyes: rhodamine B, fluorescein isothiocyanate isomer I (FITC), 4', 6-diamidino-2-phenylindole dihydrochloride (DAPI) and solvents: ethanol, chloroform, were purchased from Sigma-Aldrich. Silicon wafers were obtained from the cleanroom (Lurie Nanofabrication Facility) at the University of Michigan.

4.2.2. Templates fabrication

A ~5 nm thin film of titanium dioxide (TiO_2) was deposited on to silicon wafers through e-beam evaporation. To make the TiO_2 surface non-wettable, the surface was exposed to HDFTS silane vapors at 100°C for 30 minutes. Next, the silanised TiO_2 surfaces were exposed to deep ultraviolet radiation (UV, 254 nm) for 90-120 minutes through a quartz photomask with desired patterns. The exposed TiO_2 domains through the photomask switched from non-wettable (low surface energy) to wettable (high surface

energy). This gave us non-wettable templates with wettable domains possessing any desired geometry.

4.2.3. PLGA-PEL particle fabrication

WETS templates were dip-coated consecutively in PVP (25 wt%) in ethanol, PLGA (10-55 wt%) in chloroform, PAH (2.5 wt%) in deionized water and PSS (2.5 wt%) in deionized water solutions. All solutions were dip-coated using a syringe pump (KD Scientific) at a constant dip-coating velocity of 40 mm/min. For PVP and PLGA (on top of PVP) depositions within wettable domains, templates were dipped into their corresponding solutions and pulled out immediately (40 mm/min) without any wait time. For PAH deposition on PLGA, the surfaces were dipped in PAH aqueous solution for 2 min before pulling out of the solution. For subsequent polyelectrolyte (PEL) depositions the substrates were dipped in the solutions for 30 sec before pulling out. Each PEL deposition is followed by washing in water for 10 sec. Finally PLGA-PEL particles were released in ethanol. Then the particle dispersion in ethanol was diluted using water and sedimented for further characterization. For fluorescent microscopy measurements, rhodamine B, FITC and DAPI were added to PVP, PLGA and PSS solutions respectively before dip-coating.

4.2.4. Characterization techniques

4.2.4.1. Contact angle measurements

The contact angle measurements were conducted using a Ramé-Hart 200-F1 goniometer. All contact angles reported in this work were measured by advancing or receding a small volume of liquid (~ 2 μL) onto the surface using a 2 mL micrometer

syringe (Gilmont). At least three measurements were performed on each substrate. Typical error in measurements was ±2º.

4.2.4.2. Microscopy

Tapping-mode atomic force microscopy (AFM) was conducted using a Veeco Innova instrument. Veeco TESPA tips and Hi Res C probes were used for imaging. The surfaces were imaged using a Hitachi SU8000 ultra-high resolution scanning electron microscope (SEM) at 5 kV and an Olympus BX 51 fluorescent microscope. The multi-phasic particles were visualized using a FCLSM (Nikon A1 Confocal). Three different lasers, 405 nm laser, 488 nm Argon laser, and 533 nm Helium-Neon green (HeNeG) laser, were used to excite the dyes DAPI, FITC, and Rhodomine B respectively.

4.3. Results and discussion

4.3.1. Templates for Polymer-PEL multilayered assembly

In the WETS technique, we employ smooth, low surface energy, silanized, titanium dioxide (TiO_2) surfaces (see chapter 3) that possess finite receding contact angles (θ_{rec}) for both aqueous and different organic liquids, and pattern them with high surface energy domains (θ_{rec}) of different shapes and sizes. When such surfaces with patterned wettability are dip-coated with a polymer solution, the solution preferentially wets and self-assembles within the patterned wettable domains. Upon evaporation of the solvent, the polymer deposits within the patterned high surface energy domains, conforming to the shape and size of the domains. Similarly, multiple polymers can be sequentially deposited one on top of another within the wettable domains by dip-coating the templates in their respective polymer solutions. By varying the geometry and dimensions of the wettable domains, we can fabricate multi-phasic particles (comprising

polymers of distinct chemistries) in different shapes and in sizes as small as 25 nm[8]. Thus, this technique allows us to build multiple polymeric layers within localized micron and nanoscale domains of different shapes. In similar fashion, we can deposit PEL multilayers (followed by wash steps) on top of previously deposited polymeric layers within the wettable domains. This process of PEL assembly on nanoparticles avoids time-consuming centrifugation and purification steps[1]. Thus WETS can be easily coupled with well-characterized LbL process (on bulk substrates) to facilitate large-scale production of multi-layered particles composed of charged PEL multilayers as well as other neutral biocompatible polymeric layers (see Figure 4.1).

4.3.2. Fabrication and characterization of Polymer-PEL multilayered particles

To fabricate, multilayered Polymer-PEL particles, we first deposited polyvinylphenol (PVP, using PVP in ethanol solution) as a release layer within the wettable domains, followed by polylacticglycloicacid (PLGA, using PLGA in chloroform solution). This gave us uniform arrays of bi-phasic assemblies of PLGA and PVP (PLGA on top of PVP, see Figure 4.2) in well-defined shapes. Then the templates with PLGA-PVP patterns were dip-coated consecutively in aqueous solutions of cationic and anionic polyelectrolytes, similar to the procedures established for macroscopic surfaces. However, the difference here is PEL multilayers deposition is restricted to localized PLGA domains. Finally the PLGA particles coated with multi-layered PELs were released from the template by dissolving the sacrificial layer (PVP) in ethanol. We chose PVP as a release layer, as it doesn't dissolve in most of the solvents (including water and organic solvents such as chloroform, toluene etc) and thus allowed us to assemble multiple polymeric layers from both aqueous and organic solutions on top of the release

layer. After the release of multi-layered particles from the template, the templates can be readily reused for fabricating a new batch of multi-layered particles (see Figure 4.1), enabling a rapid, inexpensive, waste-free (significant when fabricating particles that encapsulate expensive biomolecules and drugs)[4] and easily reproducible method for manufacturing multi-layered particles.

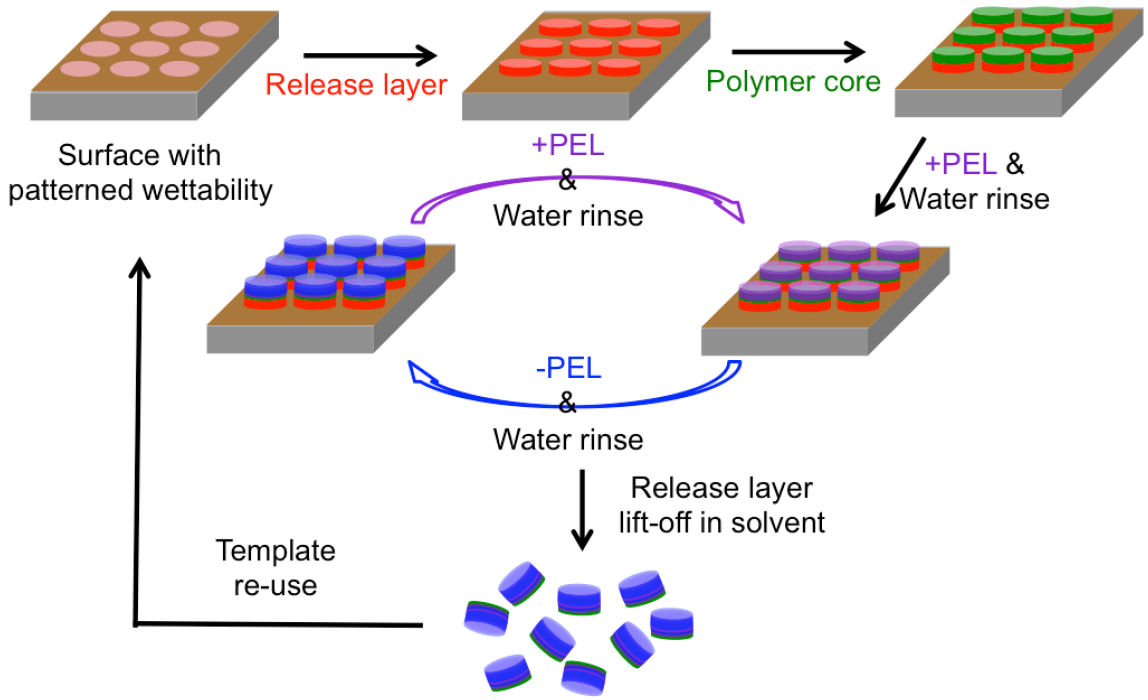

Figure 4.1. A schematic illustrating the fabrication of multi-layered PEL coated polymeric particles using WETS technique.

In this work, we utilized polly(allylaminehydrochloride) (PAH) and poly(sodium 4-styrenesulfonate) (PSS) as cationic and anionic polyelectrolytes respectively. We confirmed the sequential deposition of PVP, PLGA and polyelectrolytes (PAH-PSS) preferentially within the wettable domains using both confocal fluorescent microscopy and atomic force microscopy (AFM) measurements. We performed the measurements after each polymer deposition. Figure 4.2a, 2b and 2c shows confocal microscopy images

after polymer depositions of PVP, PLGA on top of PVP and finally PSS (before wash cycle) on top of PAH functionalized PLGA on top of PVP respectively.

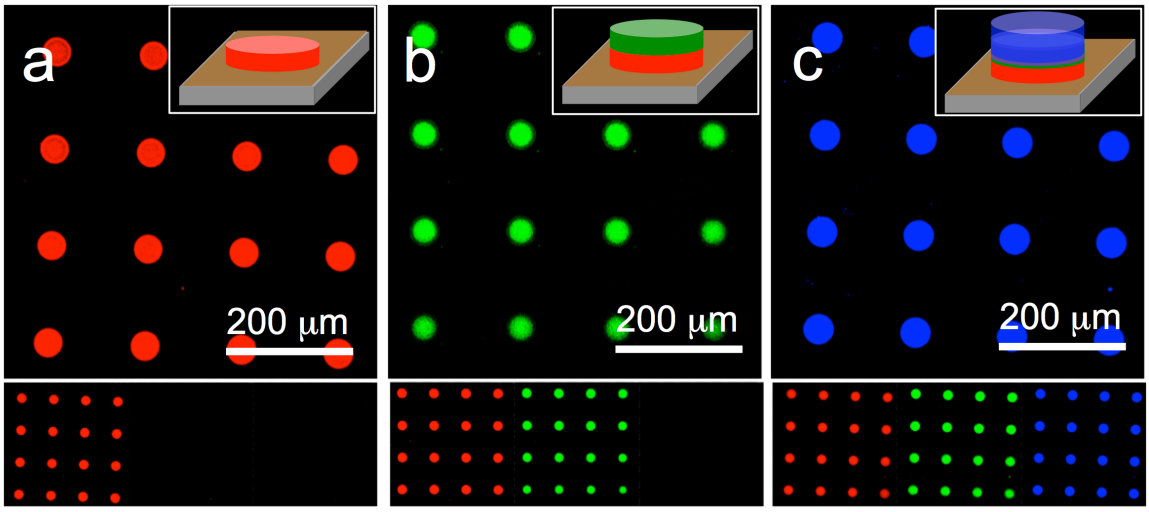

Figure 4.2. WETS enabled Multi-layered polymer depositions within localized wettable domains. Confocal fluorescent microscopy images showing wettability engendered assembly of (a) poly(4-vinylphenol) (PVP; dyed red), (b) poly(lactide-co-glycolide) acid terminated (PLGA; dyed green) on top of PVP, (c) poly(sodium 4-styrenesulfonate) (PSS; dyed blue) on top of polly(allylaminehydrochloride) (PAH; followed by water rinsing) on top of PLGA and PVP. The images below a b and c show corresponding composite confocal microscopy images indicating different phases present within the wettable domains. The top insets in a-c show schematics of the polymer layers within the high surface energy (or wettable) domains.

Here, in contrast to spray LbL on PRINT technique or other macroscopic LbL deposition techniques, PEL solutions are deposited only on PLGA patterned domains but not on the template background, during dip-coating of PEL aqueous solutions. This is due to non-wettable nature of the template background towards different polymer solutions (see Table 4.1). Localized PEL deposition minimizes the wastage of PEL aqueous solutions and it is of significant importance when fabricating particles that encapsulate expensive biomolecules and drugs.

Table 4.1 lists the advancing and receding contact angles for different liquids and polymer solutions on both the wettable and non-wettable regions of the patterned

surfaces. These measurements indicate that the polymer solutions utilized in the fabrication of PLGA-PEL particles would assemble preferentially within wettable domains upon dip-coating.

Table 4.1. Advancing (θ_A) and receding (θ_R) contact angles for different liquids and polymer solutions on the non-wettable and wettable regions of the patterned surfaces.

Liquids	Non-wettable surface		Wettable surface	
	θ_A	θ_R	θ_A	θ_R
Water	120°	112°	<10°	0°
Chloroform	64°	51°	0°	0°
Ethanol	50°	38°	0°	0°
Toluene	72°	62°	<10°	0°
Dimethylformamide (DMF)	76°	66°	<10°	0°
PVP-Ethanol	54°	39°	0°	0°
PLGA-Chloroform	66°	52°	0°	0°
PAH-Water	110°	99°	<10°	0°
PSS-Water	108°	97°	<10°	0°

As shown in Figure 4.3, we can easily tune the shape and size of the multi-layered assemblies by changing the geometry and dimensions of wettable domains (see section 4.2.2). Finally, the multi-layered PEL-PLGA particles were released in ethanol.

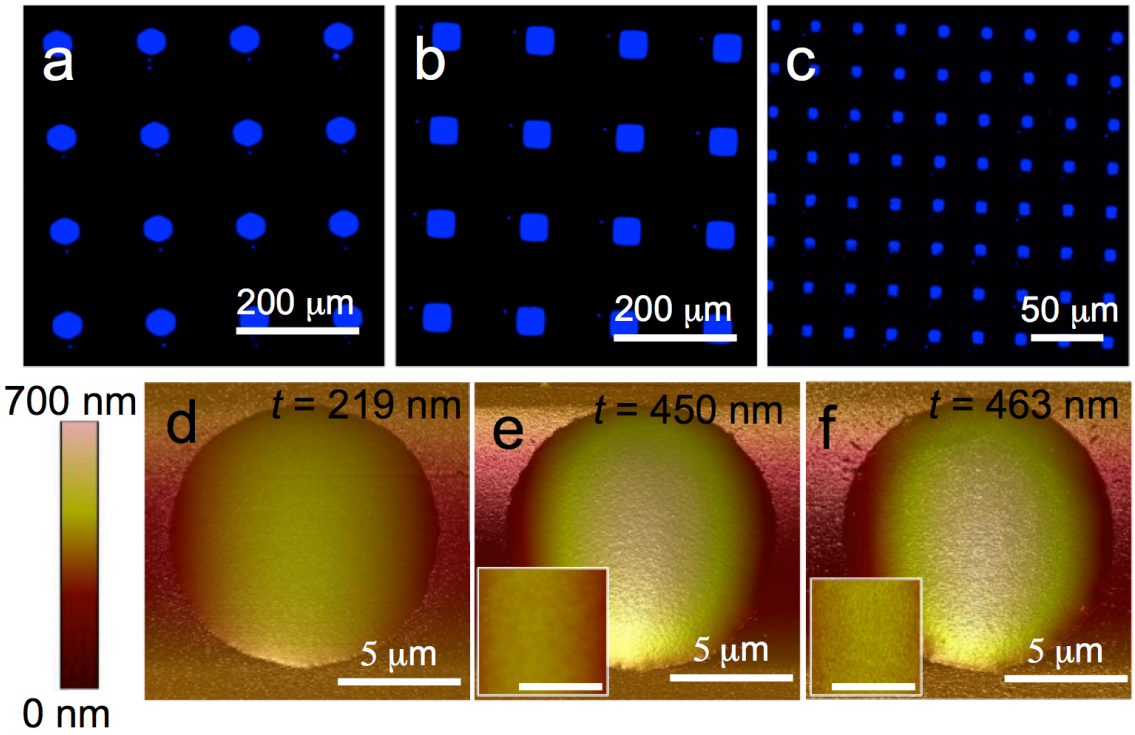

Figure 4.3. WETS enabled Multi-layered polymer depositions within localized wettable domains of different shapes. (a)-(c) Fluorescent images of multi-layered polymer patterns of different shapes: poly(sodium 4-styrenesulfonate) (PSS; dyed blue) on top of polly(allylaminehydrochloride) (PAH; followed by water rinsing) on top of PLGA and PVP. (d) (e) and (f) Atomic force microscopy height images of PVP, PLGA on top of PVP and 3 bilayers of PAH-PSS ((PAH-PSS)$_3$) on top of PLGA and PVP respectively, deposited within a wettable domain of 10 μm in diameter. Thickness *t* is the average thickness of polymers deposited within the patterned domains. The insets in h and i show corresponding AFM height images at smaller scan sizes. These images indicate change in surface morphology upon PEL deposition. The scale bars in insets for e and f represent 1 μm.

Figure 4.4a and 4c shows released PLGA particles and PLGA particles coated with 2 bilayers of PAH-PSS polyelectrolytes (PLGA-(PAH-PSS)$_2$) respectively. The carboxyl end groups present on PLGA gives the PLGA particles a net negative surface charge in aqueous medium (also indicated in zeta-potential measurements, Figure 4.4e). So, we first dip-coated PLGA patterned WETS templates in aqueous solution of PAH (cationic), followed by aqueous solution of PSS (anionic) solution. Zeta potential measurements for PLGA-PAH and PLGA-(PAH-PSS) particles are consistent with the

corresponding polyelectrolytes present on the surface of the particles (Figure 4.4e). We also see change in the surface morphology of the PLGA particles upon $(PAH\text{-}PSS)_2$ deposition (Figure 4.4b, Figure 4.4d). Figure 4.4f and 4.4h show scanning electron microscopy (SEM) images of cross-section of $(PLGA\text{-}(PAH\text{-}PSS)_2)$ and PLGA particles (10 μm in diameter) respectively. These images indicate a thin film (~8 nm) of $(PAH\text{-}PSS)_2$ coated on top of PLGA.

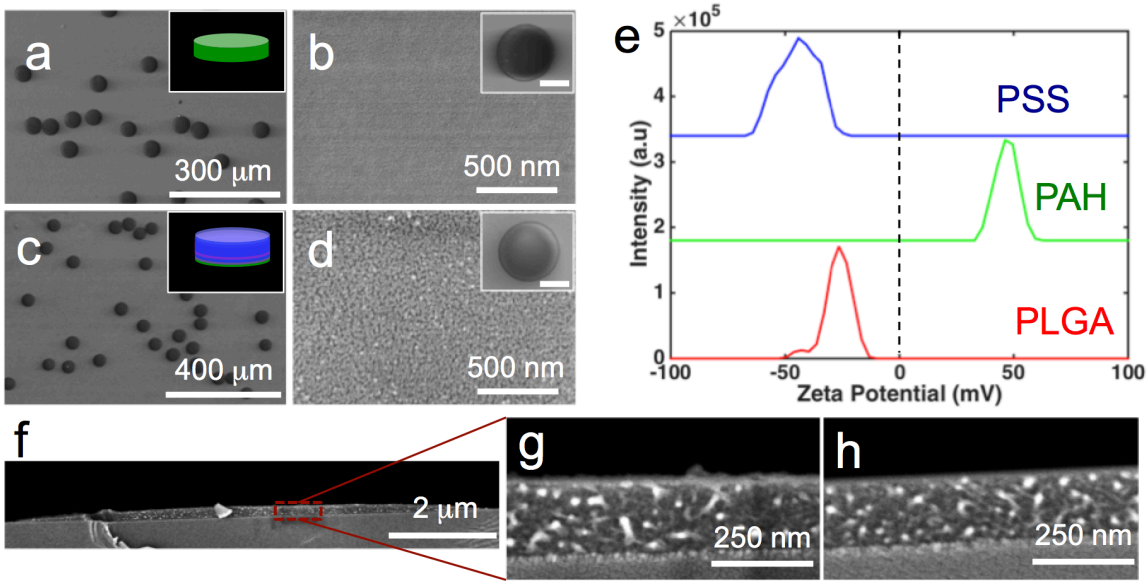

Figure 4.4. Multi-layered polyelectrolytes coated PLGA particles. Scanning electron microscopy (SEM) images of (a) PLGA circular disc shaped particles (b) PLGA particle at higher magnification showing surface morphology of the particle (c) PLGA-$(PAH\text{-}PSS)_2$ circular shaped particles (d) PLGA-$(PAH\text{-}PSS)_2$ particle at higher magnification showing surface morphology of the particle. The insets in a and c show corresponding schematics of multilayered particles (e) Zeta-potential measurements showing shift in surface charge of the PLGA particles upon layer by layer deposition of PAH and PSS. (f) Cross-section SEM image of PLGA-$(PAH\text{-}PSS)_2$ particle. (g) Higher magnification image of the region indicated by red dotted square in f. (h) Higher magnification SEM image of PLGA (uncoated) particle. These images indicate the deposition of polyelectrolyte thin film on top of PLGA.

4.3.3. Fabrication of Polymer-PEL multilayered particles in different shapes and sizes

One of the main advantages of using WETS technique to develop PLGA-PEL particles is that the technique allows us to fabricate the particles in a wide range of shapes and sizes[8]. Figure 4.5 show fabricated multi-layered PEL-PLGA particles in different shapes and sizes. In addition, we have previously reported that the preferential assembly of polymer solutions within the wettable domains on WETS templates is universal to almost all polymer solutions. So, similar to the fabrication of PLGA-(PAH-PSS) particles, this technique can be utilized for other polymer-PEL combinations as well.

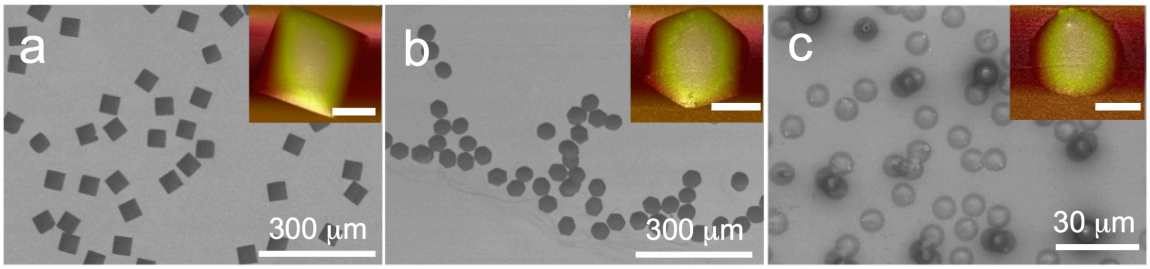

Figure 4.5. Multi-layered PEL-PLGA particles of different shapes and sizes. (a) (b) and (c) SEM images showing fabricated PLGA-$(PAH\text{-}PSS)_2$ particles of square shapes, Hexagon shapes and circular shapes (10 μm in diameter) respectively. The scale bar for the insets in a and b represent 25 μm and inset in c represent 5 μm.

4.3.4. Precise control over the thickness of polymer and PEL layers

Figure 4.6a and 6b show cross-section of a PLGA-$(PAA\text{-}PSS)_8$ particle (W = 10 μm) indicating the presence of PLGA phase and multilayered PEL phase of thickness about 31 nm. It is also possible to independently control the thickness of both PLGA and PEL layers independently while maintaining the projected shape and size of the particles. PLGA thickness (t) can be tuned by varying capillary number ($Ca = \mu V/\gamma_{LV}$) and PLGA volume fraction (ϕ) of the polymer solution[8, 20] during dip-coating process, $t = k\phi WCa^{1/3}$. Here μ is the viscosity of the polymer solution, V is the dip-coating velocity, W is the

diameter of the wettable domain and k is proportionality constant. Figure 4.6d shows variation in thickness of 10 μm and 50 μm PLGA particles upon varying the PLGA concentration in the polymer solution during dip-coating. Note that variation in polymer concentration varies both ϕ and μ. Multi-layered PEL coating thickness can be tuned by varying the number of cycles of (PAH-PSS) bilayer depositions. Figure 4.6e shows the variation of PEL thickness with increase in number of bilayers deposited on top of PLGA particles of diameter 50 μm and 10 μm.

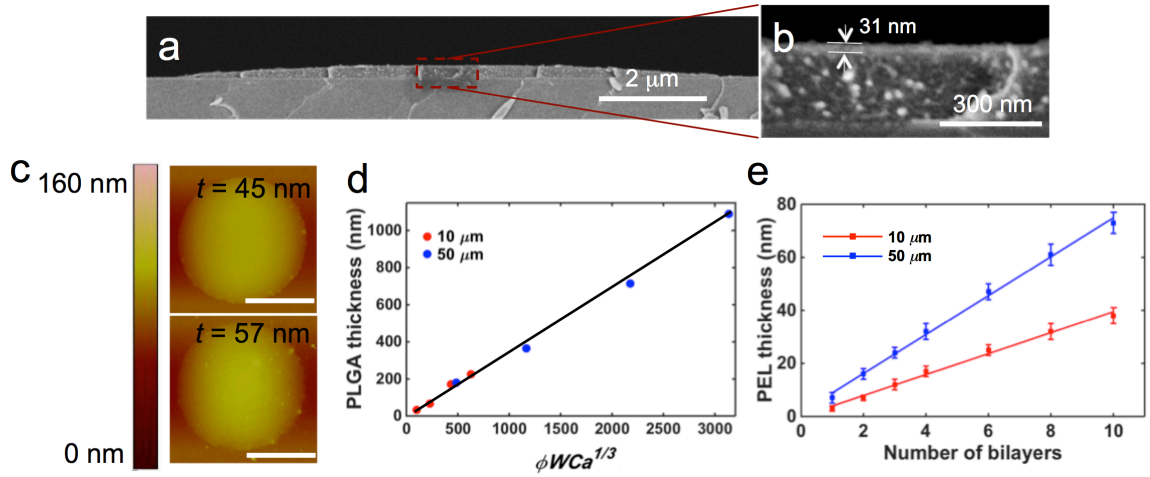

Figure 4.6 Control over the thickness of PLGA and PEL layers. **(**a) SEM cross-section image of PLGA-$(PAH\text{-}PSS)_8$ particle of 10 μm in diameter. (b) Higher magnification SEM image of the red dotted region indicated in a. The image shows deposition of PEL multilayered thin film on top of PLGA. (c) AFM height images of PLGA particle and PLGA-$(PAH\text{-}PSS)_3$ particle. (d) Plot showing variation in PLGA thickness of 10 μm and 50 μm particles with increase in PLGA concentration (increases both ϕ and μ) of the polymer solution during dip coating. (e) Plot showing variation in thickness of polyelectrolyte multilayers with increase in number of PAH-PSS bilayers deposition on top of PLGA particles of diameter 10 μm and 50 μm.

4.4. Conclusions

In conclusion, we have demonstrated that WETS methodology can serve as a rapid and inexpensive route for large-scale fabrication of multilayered PEL coated polymeric particles, with precise control over the composition, surface charge, shape and size of the particles. This ability to fine tune design parameters of multi-layered particles is very useful in optimizing and designing ideal drug carriers for combinatorial therapies and theranostics applications.

4.5. References

1. Yan, Y., Bjonmalm, M. & Caruso, F. Assembly of Layer-by-Layer Particles and Their Interactions with Biological Systems. *Chem Mater* **26**, 452-460 (2014).
2. Shimoni, O., Yan, Y., Wang, Y.J. & Caruso, F. Shape-Dependent Cellular Processing of Polyelectrolyte Capsules. *Acs Nano* **7**, 522-530 (2013).
3. Mitragotri, S. & Stayton, P. Organic nanoparticles for drug delivery and imaging. *MRS Bulletin* **39**, 219-223 (2014).
4. Caldorera-Moore, M., Guimard, N., Shi, L. & Roy, K. Designer nanoparticles: incorporating size, shape and triggered release into nanoscale drug carriers. *Expert Opin Drug Del* **7**, 479-495 (2010).
5. Perry, J.L., Herlihy, K.P., Napier, M.E. & Desimone, J.M. PRINT: A Novel Platform Toward Shape and Size Specific Nanoparticle Theranostics. *Accounts Chem Res* **44**, 990-998 (2011).
6. Dreaden, E.C. et al. Bimodal Tumor-Targeting from Microenvironment Responsive Hyaluronan Layer-by-Layer (LbL) Nanoparticles. *Acs Nano* **8**, 8374-8382 (2014).
7. Morton, S.W., Poon, Z.Y. & Hammond, P.T. The architecture and biological performance of drug-loaded LbL nanoparticles. *Biomaterials* **34**, 5328-5335 (2013).
8. Kobaku, S.P.R. et al. Wettability Engendered Templated Self-assembly (WETS) for Fabricating Multiphasic Particles. *Acs Applied Materials & Interfaces* **7**, 4075-4080 (2015).
9. Elbakry, A. et al. Layer-by-Layer Assembled Gold Nanoparticles for siRNA Delivery. *Nano Lett* **9**, 2059-2064 (2009).
10. Deng, Z.J. et al. Layer-by-Layer Nanoparticles for Systemic Codelivery of an Anticancer Drug and siRNA for Potential Triple-Negative Breast Cancer Treatment. *Acs Nano* **7**, 9571-9584 (2013).
11. Whitehead, K.A., Langer, R. & Anderson, D.G. Knocking down barriers: advances in siRNA delivery (vol 8, pg 129, 2009). *Nat Rev Drug Discov* **9**, 412-412 (2010).
12. Poon, Z., Lee, J.B., Morton, S.W. & Hammond, P.T. Controlling in Vivo Stability and Biodistribution in Electrostatically Assembled Nanoparticles for Systemic Delivery. *Nano Lett* **11**, 2096-2103 (2011).
13. Zahr, A.S., de Villiers, M. & Pishko, M.V. Encapsulation of drug nanoparticles in self-assembled macromolecular nanoshells. *Langmuir* **21**, 403-410 (2005).
14. Morton, S.W. et al. Scalable Manufacture of Built-to-Order Nanomedicine: Spray-Assisted Layer-by-Layer Functionalization of PRINT Nanoparticles. *Advanced Materials* **25**, 4707-4713 (2013).
15. Qi, A.S. et al. Template-free Synthesis and Encapsulation Technique for Layer-by-Layer Polymer Nanocarrier Fabrication. *Acs Nano* **5**, 9583-9591 (2011).
16. Voigt, A. et al. Membrane filtration for microencapsulation and microcapsules fabrication by layer-by-layer polyelectrolyte adsorption. *Ind Eng Chem Res* **38**, 4037-4043 (1999).

17. Kantak, C., Beyer, S., Yobas, L., Bansal, T. & Trau, D. A 'microfluidic pinball' for on-chip generation of Layer-by-Layer polyelectrolyte microcapsules. *Lab Chip* **11**, 1030-1035 (2011).
18. Richardson, J.J. et al. Preparation of Nano- and Microcapsules by Electrophoretic Polymer Assembly. *Angew Chem Int Edit* **52**, 6455-6458 (2013).
19. Priest, C. et al. Microfluidic polymer multilayer adsorption on liquid crystal droplets for microcapsule synthesis. *Lab Chip* **8**, 2182-2187 (2008).
20. Darhuber, A.A., Troian, S.M., Davis, J.M., Miller, S.M. & Wagner, S. Selective dip-coating of chemically micropatterned surfaces. *J Appl Phys* **88**, 5119-5126 (2000).

CHAPTER 5

Dynamic shape and size reconfigurations in multi-phasic particles

5.1. Introduction

In past two decades, numerous strategies have been developed in an attempt to mimic nature's ability to precisely tune shape, size, and composition of the nanoparticles in response to changes in environment[1-6]. Synthetic nanoparticles with stimuli responsive properties are expected to have significant impact on various applications including drug delivery[4, 5, 7], biosensors[6], self-assembly of superstructures[8, 9] etc. In case of nanoparticle drug carriers, the particles journey is very complex and requires different physiological properties at different stages of the particle journey. For example, previous reports indicate that non-spherical drug carriers are better suited for targeted delivery of drugs to the diseased sites, while spherical particles are internalized faster by the diseased cells compared to non-spherical or elongated particles[4, 5, 7]. Similarly, different sizes[5, 10] and surface chemistries[11-13] are preferred at different stages of the drug carrier journey. These variations in requirements for the design parameters of the nanoparticles at various stages of an application, necessitates the need to develop polymer particle systems that can dynamically change their shape, size and composition[5].

As reported recently, one way to switch shape of the polymeric particles, is to increase the local temperature of the polymer particles above glass transition temperature of the polymer, using stimuli such as heat, pH or ultra-sonication[4, 6]. This simple approach to switch the shape and size of the particles can be useful in developing biomimetic actuators, sensors and artificial camouflage systems[4, 6, 14]. In addition, nanoparticle drug carriers with dynamic shape and size change properties have shown to improve cellular internalization kinetics and timely elimination of drug carriers[4, 5, 7].

However, except for a few reports, most of stimuli responsive polymer particles studies have been focused on single-phase systems. But in nature, most stimuli responsive systems are multi-phasic systems. Utilizing multi-phasic particles broadens the number of reconfigurations, in terms of number of shapes, sizes and surface chemistries, a particle can assume in response to stimulus. So, in this work, we fabricated a range of different multi-phasic particles and studied their shape shifting and size-switching process in response to increase in temperature of the surrounding liquid medium. We have further developed mathematical relationships that predict the exact change in geometry and dimensions of the multi-phasic particles upon providing the stimulus.

5.2. Experimental Procedure

5.2.1. Materials

Heptadecafluoro-1,1,2,2-tetrahydrodecyl)trichlorosilane (HDFTS) was purchased from Gelest Inc. Polymers: polyvinylacetate (PVAc, with a weight average molecular weight of $M_w \approx$ 25 kDa), poly(*D,L*-lactide-co-glycolide) (PLGA, $M_w \approx$ 24-38 kDa, lactide:glycolide 50:50, acid terminated), polystyrene (PS with a weight average

molecular weight of $M_w \approx$ 1.2 kDa and $M_w \approx$ 45 kDa), polymethylmethacrylate (PMMA, $M_w \approx$ 25 kDa), polycaprolactone (PCap, $M_w \approx$ 55 kDa) fluorescent dyes: rhodamine B, fluorescein isothiocyanate isomer I (FITC), 4', poly[tris(2,5-bis(hexyloxy)-1,4-henylenevinylene)-*alt*-(1,3- phenylenevinylene)] (PTDPV, blue fluorescent dye) and solvents: ethanol, chloroform, were purchased from Sigma-Aldrich. Silicon wafers were obtained from the cleanroom (Lurie Nanofabrication Facility) at the University of Michigan.

5.2.2. Templates fabrication

A ~5 nm thin film of titanium dioxide (TiO_2) was deposited on to silicon wafers through e-beam evaporation. To make the TiO_2 surface non-wettable, the surface was exposed to HDFTS silane vapors at 100°C for 30 minutes. Next, the silanised TiO_2 surfaces were exposed to deep ultraviolet radiation (UV, 254 nm) for 90-120 minutes through a quartz photomask with desired patterns. The exposed TiO_2 domains through the photomask switched from non-wettable (low surface energy) to wettable (high surface energy). This gave us non-wettable templates with wettable domains possessing any desired geometry.

5.2.3. Shape-shifting procedure

For shape-shifting, first multi-phasic particles were fabricated using WETS technique (discussed in chapter 3 and 4). Then the particles were transferred to water medium and the particle-water dispersion is heated above the glass transition temperature (T_g) of the polymers comprising the particle. In case of particles that have T_g higher than 100°c (such as PMMA, high molecular weight PS etc.) we used glycerol-water mixtures as the liquid medium for shape-shifting experiments.

5.2.4. Characterization techniques

5.2.4.1. Contact angle measurements

The contact angle measurements were conducted using a Ramé-Hart 200-F1 goniometer. All contact angles reported in this work were measured by advancing or receding a small volume of liquid (~ 2 μL) onto the surface using a 2 mL micrometer syringe (Gilmont). At least three measurements were performed on each substrate. Typical error in measurements was ±2º.

5.2.4.2. Microscopy

Tapping-mode atomic force microscopy (AFM) was conducted using a Veeco Innova instrument. Veeco TESPA tips and Hi Res C probes were used for imaging. The surfaces were imaged using a Hitachi SU8000 ultra-high resolution scanning electron microscope (SEM) at 5 kV and an Olympus BX 51 fluorescent microscope. The multi-phasic particles were visualized using a FCLSM (Nikon A1 Confocal). Three different lasers, 405 nm laser, 488 nm Argon laser, and 533 nm Helium-Neon green (HeNeG) laser, were used to excite the dyes DAPI, FITC, and Rhodomine B respectively.

5.3. Results and discussion

5.3.1. Fabrication and shape-shifting of multi-phasic particles

In this work to study shape and size switching of multi-phasic particles, we have utilized the WETS technique[15] to fabricate multi-phasic particles of different non-spherical shapes, sizes and chemistries (type of polymers and number of polymeric phases). In the WETS technique, we first fabricated WETS templates similar to procedures described in chapter 3. As shown in Figure 5.1, WETS templates are then dip-coated with a polymer solution, the solution preferentially wets and self-assembles within

the patterned wettable domains. Upon evaporation of the solvent, the polymer deposits within the patterned high surface energy domains, conforming to the shape and size of the domains. Similarly, multiple polymers can be sequentially deposited one on top of another within the wettable domains by dip-coating the templates in their respective polymer solutions. Finally particles were released from template by dissolving first dip-coated polymer release layer in water (Figure 5.1). Further, for shape shifting of the multiphasic particles, we increased temperature of the multi-phasic particles and water dispersion above the glass transition temperature of the polymers comprising the particles.

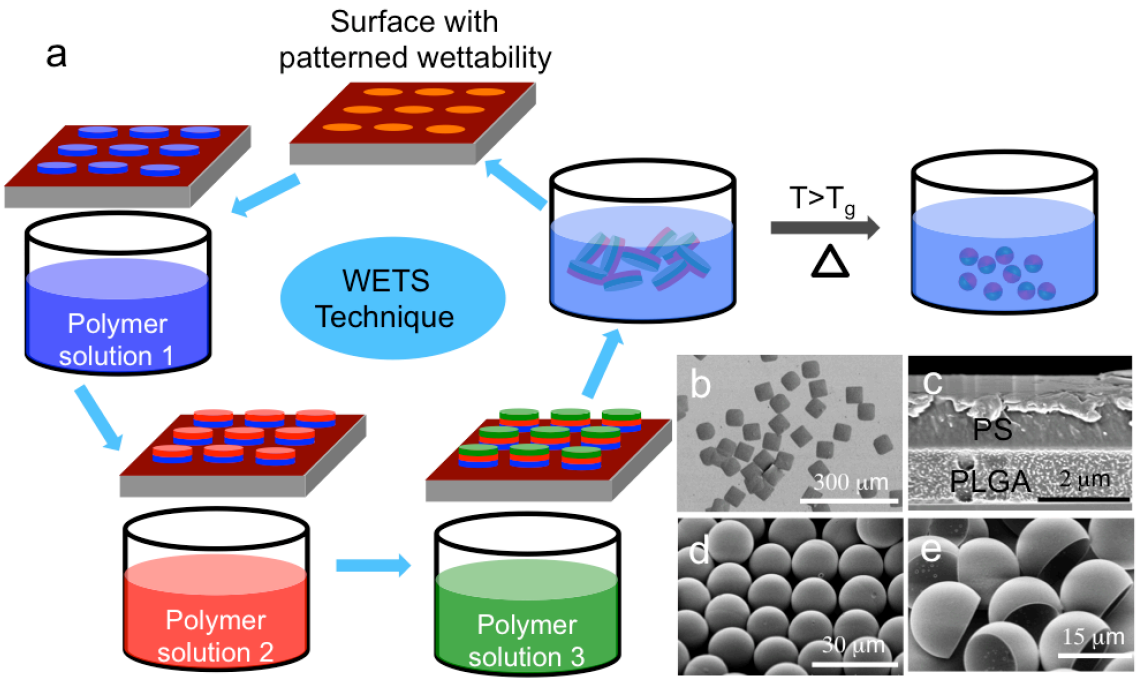

Figure 5.1. Shape-shifting process of multi-phasic particles fabricated using WETS technique. a) Schematic showing the shape-shifting process. b) PS-PLGA biphasic particles fabricated using WETS technique. c) Cross-section SEM image of the particles shown in b. d) PS-PLGA spherical particles after shape-shifting of the corresponding WETS particles. e) PLGA compartments after selective dissolution of PS compartments from the particles shown in d.

5.3.2. Driving factors for shape-shifting of multi-phasic particles

When the temperature of single phase polymer particles (of any shape) is increased beyond it's glass transition temperature in an immiscible liquid medium, the particles switch into spherical shapes. Switching of the particles shape is driven by minimization of interfacial free energy of the polymer-liquid interface ($\gamma_{P,L}$). Here, increase in temperature acts as a stimulus and provides mobility to polymer chains to reconfigure themselves in to shapes with minimum polymer-liquid interfacial area. While for single-phasic particles, spherical shape is always the configuration with minimum interfacial energy, multi-phasic particles can have many different configurations in terms of both external shape and internal structure of different polymeric phases comprising the particle. The stable configuration is dictated by the minimization of the sum of interfacial surface energies of multiple interfaces present in the system.

Figure 5.1b-1e show shape shifting of biphasic disc shaped WETS particles (composed of polystyrene and polylacticglycolide (PLGA) polymers) into monodisperse spherical particles. To understand the internal structure of the shape-shifted particles, we have preferentially dissolved polystyrene phase in cyclohexane leaving only PLGA compartments of the particles unaffected. Figure 5.1e shows the structure of PLGA compartment within PS-PLGA shape-shifted particles. Figure 5.1e clearly indicates that the PLGA phase partially encapsulates the polystyrene phase. This behavior can be correlated to higher PS-water interfacial surface energy ($\gamma_{PS,W}$) compared to $\gamma_{PLGA,W}$. Since $\gamma_{PS,W} > \gamma_{PLGA,W}$, the biphasic particles tend to minimize the interfacial area between PS and water. Similar behavior has been observed for all of the multi-phasic polymer particles investigated in this work. Figure 5.2 and Table 5.1 clearly indicate that the

polymeric phase with higher polymer-liquid interfacial energy $\gamma_{P,L}$ always encapsulates the polymer phase with lower $\gamma_{P,L}$.

Table 5.1 lists different multi-phasic particles fabricated in this work for shape-shifting studies. The table also shows the comparison between γ_{PL} and internal structure of the shape-shifted particles.

Table 5.1. Correlation between polymer-liquid interfacial energies and configuration of shape-shifted particles.

Initial WETS particles		Shape-shifted particles	
Polymer 1, γ_{P1L}	Polymer 2, γ_{P2L}	Outer phase	Inner phase
PLGA, 1	PS, 26	PLGA	PS
PVAc, 4	PS, 26	PVAc	PS
PMMA, 10	PS, 26	PMMA	PS
PLGA, 1	PMMA, 10	PLGA	PMMA
PCap, 14	PS, 26	PCap	PS
PLGA, 1	PVAc, 4	PLGA	PVAc

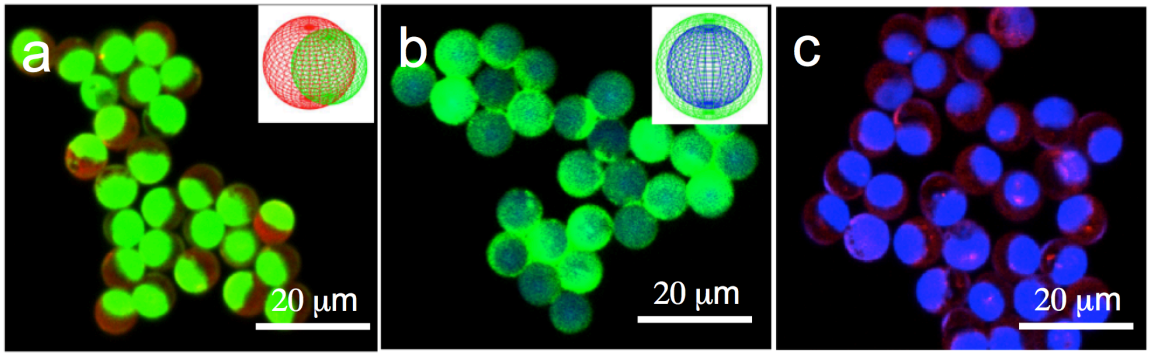

Figure 5.2. Shape-shifted biphasic particles. a-c) confocal microscopy images of shape-shifted PMMA (dyed green) - PLGA(dyed red) (a), PMMA (dyed green) – PS (dyed blue) (b), PLGA (dyed red) – PS (dyed blue). The insets in a and b show the corresponding theoretically predicted configurations.

In addition to partially encapsulated particles, we found that some biphasic particles, such as PS-PMMA particles and PLGA-PVAc particles shape-shifted into core-shell type particles. Here polymers with low $\gamma_{P,L}$ ($\gamma_{PMMA,W}$ =10, $\gamma_{PLGA,W}$ =1) were completely encapsulating the polymers with high $\gamma_{P,L}$ ($\gamma_{PS,W}$ =26, $\gamma_{PVAc,W}$ =4) leading to core-shell particles. The final configuration of shape-shifted particles (partially encapsulated or core-shell particles) is determined by the minimization of total surface free energy ($E = \gamma_{P1,L}A_{P1,L} + \gamma_{P1,P2}A_{P1,P2} + \gamma_{P2,L}A_{P2,L}$). Figure 5.2 shows the confocal microcopy images of different shape-shifted particles and the insets show the corresponding simulated images. We have obtained the simulated images by calculating the conformation for which *E* is minimum, as discussed in following section 5.3.3.

5.3.3. Relationships to predict configuration of shape-shifted biphasic particles

To understand the correlation between the shape-shifted configurations and interfacial surface energies, we have developed the following conditions by calculating the difference in surface free energy between the three different particle configurations:

(Equation 5.1) $\gamma_{P1P2} < \gamma_{P2L} - \gamma_{P1L}$ ($\gamma_{P1} < \gamma_{P2}$) for core-shell configuration

(Equation 5.2) $\gamma_{P1P2} > \gamma_{P2L} - \gamma_{P1L}$ and $\gamma_{P1P2} < \gamma_{P1L} + \gamma_{P2L}$ for partially encapsulated configuration

(Equation 5.3) $\gamma_{P1P2} > \gamma_{P1L} + \gamma_{P2L}$ for completely phase separated configuration

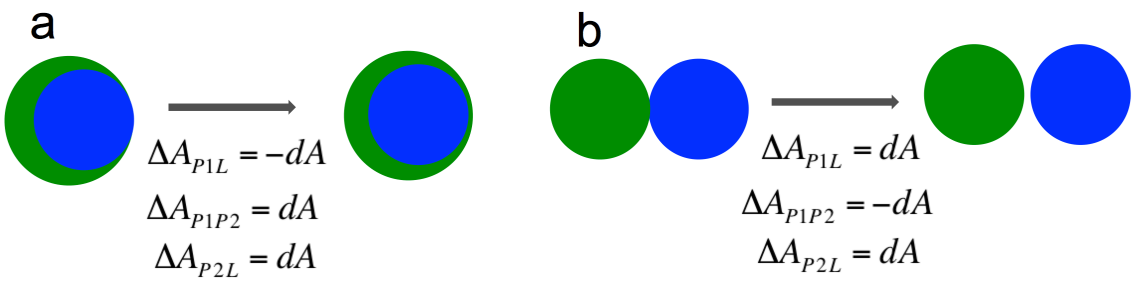

Figure 5.3. Schematics showing models of the particle configurations used to derive conditions for predicting stable configuration a) partially encapsulated and core-shell configurations b) partially encapsulated and completely phase separated configurations.

To derive condition for core-shell structures, we calculated the difference in surface free energy between the partially encapsulated configuration and core-shell configuration shown in Figure 5.3a. As we aim to derive the border condition here, it is convenient to assume that the difference in $A_{P1,P2}$ between the two conformations is very small $\Delta A_{P1,P2} = dA$. Consequently $\Delta A_{P1,L}$ and $\Delta A_{P2,L}$ are dA and $-dA$ respectively. Now, the the difference in surface free energy between the two conformations can be calculated as:

(Equation 5.4) $E_{CS} - E_{PE} = \gamma_{P1L} dA + \gamma_{P1P2} dA - \gamma_{P2L} dA$

Here, the subscripts PE and CS correspond to partially encapsulated and core-shell configurations respectively. The condition for the stable core-shell configuration can be given as:

(Equation 5.5) $E_{CS} - E_{PE} = \gamma_{P1L} dA + \gamma_{P1P2} dA - \gamma_{P2L} dA < 0$

From this equation, we obtain the condition ($\gamma_{P1P2} < \gamma_{P2L} - \gamma_{P1L}$) shown in equation 5.1 for stable core-shell configuration.

Similarly by comparing the surface free energy for the two configurations shown in Figure 5.3b, we can obtain the following expression for stable completely phase separated (CP) configuration:

(Equation 5.6) $E_{CP} - E_{PE} = \gamma_{P1L}dA - \gamma_{P1P2}dA + \gamma_{P2L}dA < 0$

From this equation, we can obtain the condition ($\gamma_{P1P2} > \gamma_{P1L} + \gamma_{P2L}$) shown in equation 5.3 for stable completely phase separated configuration.

Now, the condition for stable partially encapsulated structure can be obtained from the following expressions:

(Equation 5.7) $E_{CS} - E_{PE} = \gamma_{P1L}dA + \gamma_{P1P2}dA - \gamma_{P2L}dA > 0$

(Equation 5.8) $E_{CP} - E_{PE} = \gamma_{P1L}dA - \gamma_{P1P2}dA + \gamma_{P2L}dA > 0$

These equations result in the conditions ($\gamma_{P1P2} > \gamma_{P2L} - \gamma_{P1L}$ and $\gamma_{P1P2} < \gamma_{P1L} + \gamma_{P2L}$) for stable PE configuration.

Further, we have also verified these conditions, by plotting the variation in E with the increase in extent of encapsulation of phase $P2$ (high $\gamma_{P,L}$) in $P1$ (low $\gamma_{P,L}$). We expressed the extent of encapsulation in terms of the ratio h/D_2 (as indicated in Figure 5.4b). Here h is the height of the spherical cap of phase $P2$ encapsulated within phase $P1$ and D_2 is the diameter of the $P2$ phase compartment. In the plots, h/D_2 at which E is minimum, corresponds to the stable configuration of the multi-phasic particles upon shape-shifting. We obtained the E vs h/D_2 plots (Figure 5.4c-4e) for different combinations of γ_{P1P2}, γ_{P1L} and γ_{P2L} and found that the stable configuration predicted by E_{min} always matches with the configurations given by the conditions in the equations 5.1 to 5.3.

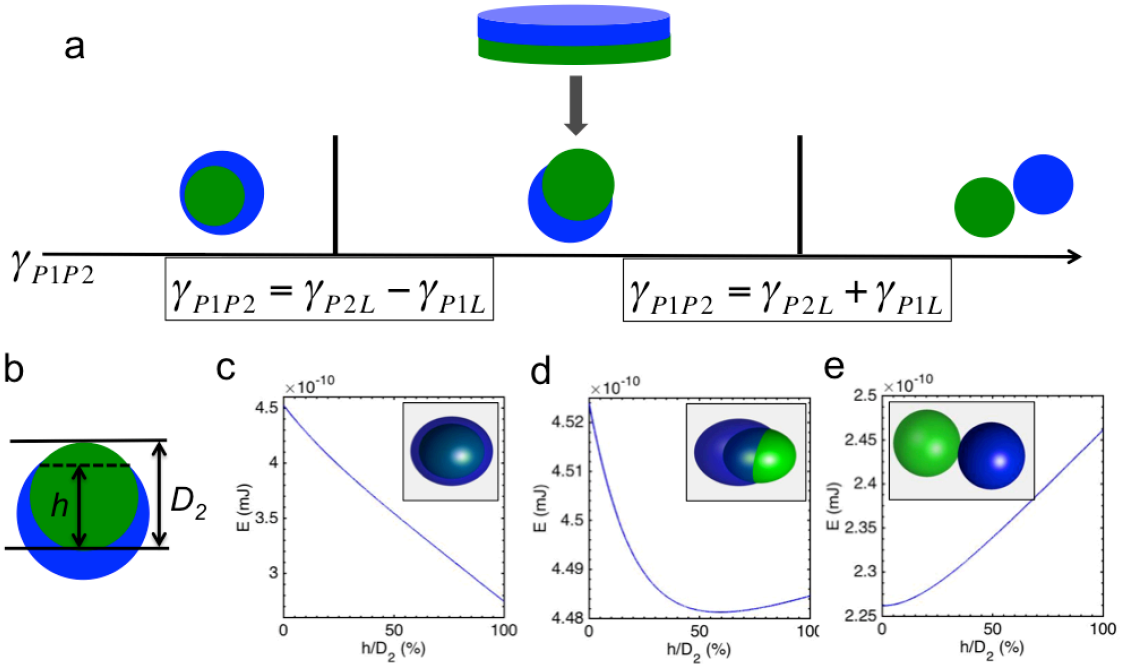

Figure 5.4. Theoretical models predicting configurations of shape-shifted WETS particles. a) Schematics showing three possible shape reconfigurations upon shape-shifting of WETS particles. b) Model particle geometry considered for the E vs h/D_2 plots. c-e) E vs h/D_2 plots showing the minimum free energy states for the biphasic particles with different combinations of interfacial surface energies. c corresponds to $\gamma_{P1P2} < \gamma_{P2L} - \gamma_{P1L}$, d corresponds to $\gamma_{P1P2} > \gamma_{P2L} - \gamma_{P1L}$ and $\gamma_{P1P2} < \gamma_{P1L} + \gamma_{P2L}$ and e corresponds to $\gamma_{P1P2} > \gamma_{P1L} + \gamma_{P2L}$.

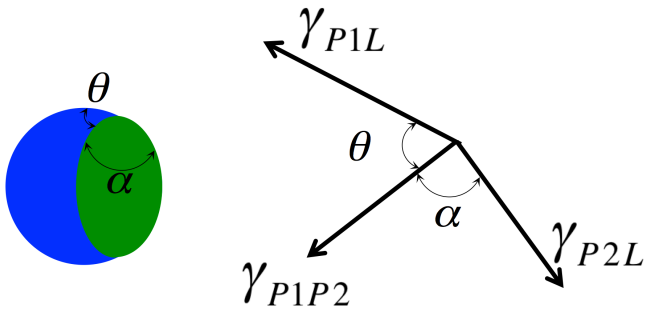

Figure 5.5. Schematic showing interfacial surface tension vectors

Further, we have observed experimentally that the encapsulated phase $P2$ doesn't have a perfect spherical shape, but it instead takes a lens shape of a finite angle α. This effect is expected, as all the phases (polymers and surrounding liquid) in contact are in

liquid state at the shape-shifting temperatures. It is possible to estimate the lens angle of phase $P2$ and the contact angle between $P1P2$ and $P1L$ interface by balancing the interfacial surface tension vectors (as shown in Figure 5.5) at the three phase contact line. This results in the following expressions:

$$\cos\theta = \frac{\gamma_{P2L}^2 - \gamma_{P1P2}^2 - \gamma_{P1L}^2}{2\gamma_{P1P2}\gamma_{P1L}}$$

$$\cos\alpha = \frac{\gamma_{P1L}^2 - \gamma_{P1P2}^2 - \gamma_{P2L}^2}{2\gamma_{P1P2}\gamma_{P2L}}$$

Note that at the boundary conditions of $\alpha = 0°$ (completely phase separated) and $\alpha = 180°$ (core-shell) corresponds to the limiting conditions given by the equations 5.1-5.3.

5.3.4. Shape-shifting of multiphasic particles of different compositions

Figure 5.6a-6c shows both partial encapsulated and core-shell particles at different compositions of $P1$ and $P2$. We see from these results, type of particle configuration remain constant across different compositions of the particles.

We have also shape-shifted tri-phasic particles composed of PLGA, PS and PVAc polymeric phases (see Figure 5.6d-6f). To understand the internal structure of these particles, we preferentially dissolved the PS in cyclohexane without affecting PVAc and PLGA phases (Figure 5.6e). Further we have also dissolved the PVAc in ethanol without affecting PS and PLGA phases (Figure 5.6f). These images clearly demonstrate the internal structure of the shape-shifted triphasic particles.

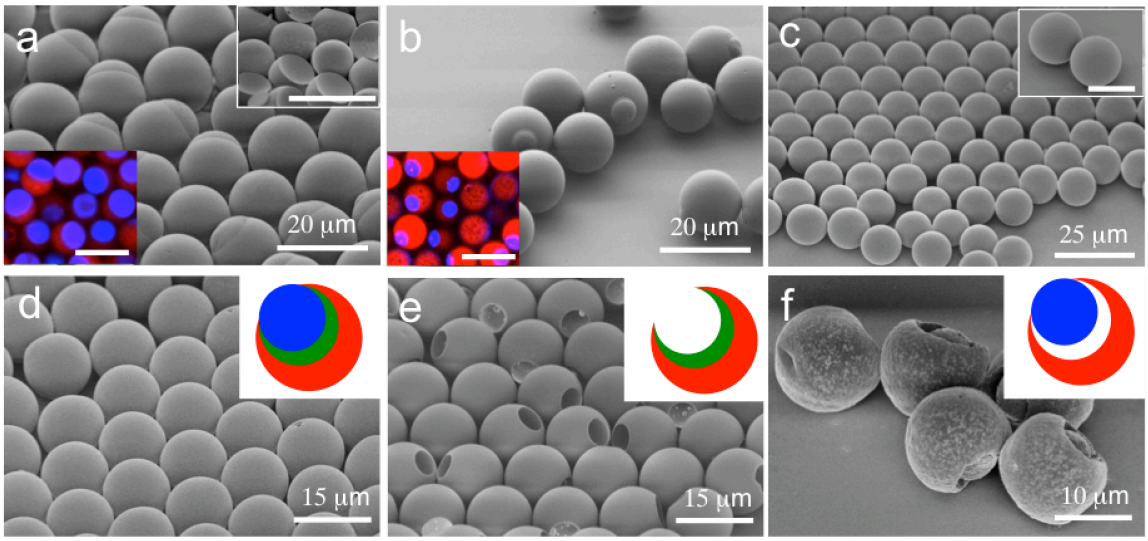

Figure 5.6. Shape-shifted particles of different compositions. Shape-shifted biphasic particles composed of a) 80 volume percent (vol%) PLGA and 20 vol% PS b) 20 vol% PLGA and 80 vol% PS c) 50 vol% PMMA and 50 vol% PS. The bottom insets in a and b show corresponding confocal microscopy images. PLGA is dyed red and PS is dyed blue. Top insets in a and c show SEM images of the particles after selective PS dissolution from the particles shown in a and c respectively. Top inset in c shows that cyclohexane doesn't affect the particle shape. This indicates PS is completely encapsulated within PMMA shell. The scale bars in a and b represent is 20 μm and in c represent 10 μm.

5.3.5. Shape-shifting of multiphasic particles of different sizes and shapes

One of the main advantages of using WETS technique for the fabrication of shape-switching multi-phasic particles is that, this technique allows us to fabricate multi-phasic particles from a wide range of polymers and in different sizes and shapes. Figure 5.7a and 5.7b shows the shape shifting of PS-PLGA bi-phasic particles of different sizes. The size of the shape-shifted particles can be easily estimated by equating the volume of the shape-shifted particles with the initial volume of the disc-shaped particles. Further, the size of the shape-shifted particles can be tuned by either varying the thickness or the diameter of the initial disc shaped particles. The ability to reconfigure the particle shape and size has significant importance for drug delivery applications. For example, nanoparticle drug carriers of non-spherical shapes have shown to accumulate better at the

targeted tumor tissues due to marginal effect. But at the same time, previous reports indicate that the internalization of non-spherical particles by tumor cells is very slow compared to their spherical counter parts[4, 5]. Therefore, non-spherical particles that have an ability to reconfigure their shape into spherical shapes at the tumor tissues can have huge impact on the targeting efficiency of nanoparticle drug carriers.

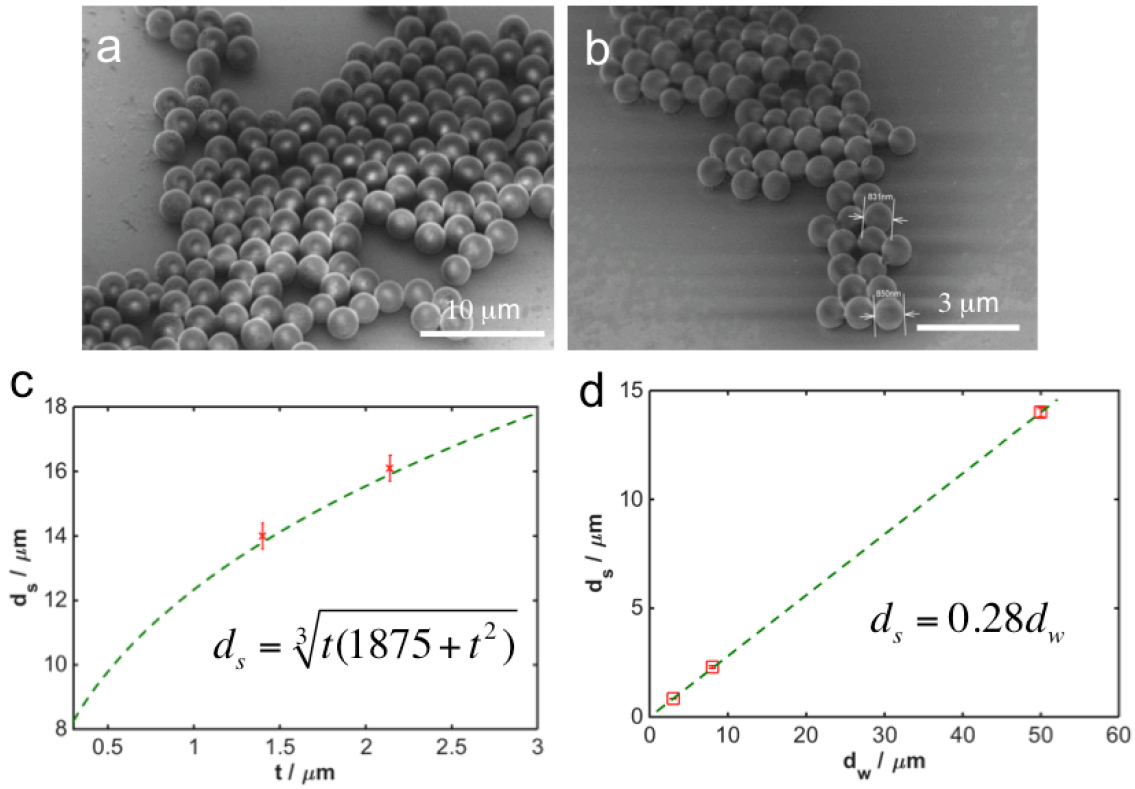

Figure 5.7. Shape-shifting of biphasic particles of different sizes. Shape-shifted PS-PLGA biphasic particles with average diameter of a) 2.5 μm and b) 840 nm. Plots showing the control over the size of the shape-shifted particles by varying c) thickness and d) diameter of the disc shaped WETS particles before shape-shifting.

In figure 5.8, we demonstrate the ability of WETS particles of different shapes to reconfigure themselves in to different shapes based on the temperature-time profile. Note that, in addition to change in shape and size, the shape-shifting process of WETS particles also involves the change in surface composition and modulus of the particles.

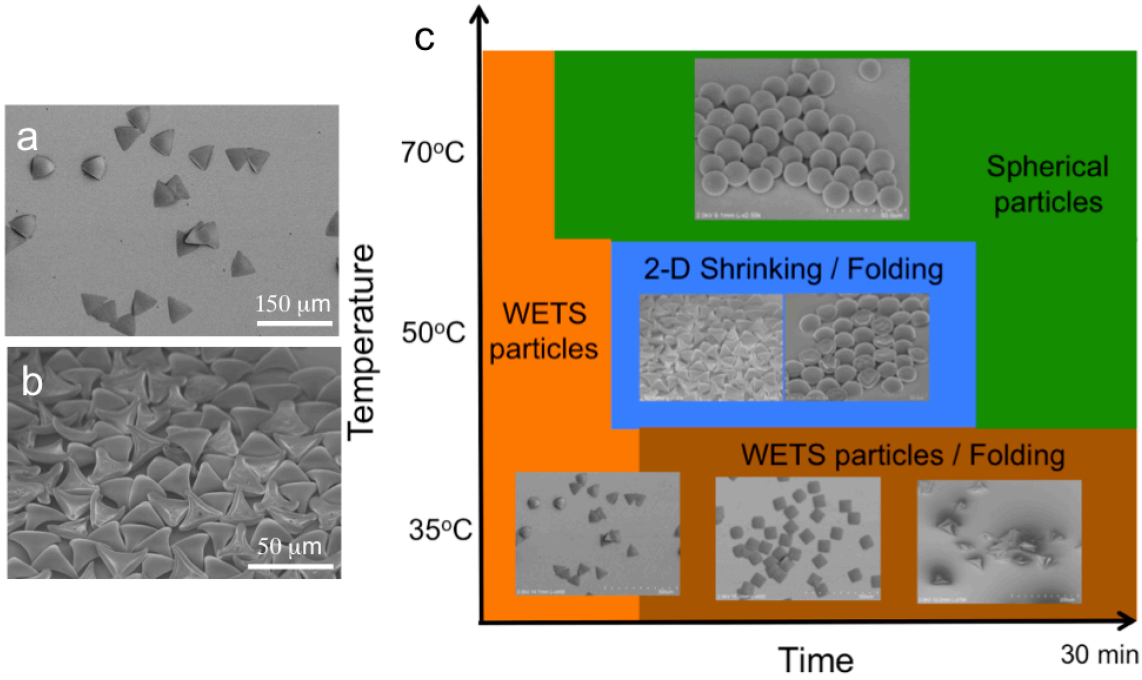

Figure 5.8. Shape-shifting of biphasic particles of different shapes. a) Triangle shaped PS-PLGA biphasic WETS particles b) Particles shown in a after shape-shifting at 50 °c for a brief period c) phase diagram showing the reconfiguration of the WETS particles upon exposure to different temperature-time schedules.

5.4. Conclusions

In conclusion, we have demonstrated the shape-shifting of a wide range of multi-phasic particles of different compositions, sizes and shapes. We have also developed mathematical relations that predict the configuration of multi-phasic particles upon shape shifting. In addition to the applications of the reconfigurable particles discussed in this work, these results will also help us better understand and mimic various actuating and sensing mechanisms available in nature.

5.5. References

1. Yoshida, M. & Lahann, J. Smart nanomaterials. *Acs Nano* **2**, 1101-1107 (2008).
2. Stuart, M.A.C. et al. Emerging applications of stimuli-responsive polymer materials. *Nat Mater* **9**, 101-113 (2010).
3. Lv, S. et al. Designed biomaterials to mimic the mechanical properties of muscles. *Nature* **465**, 69-73 (2010).
4. Yoo, J.W. & Mitragotri, S. Polymer particles that switch shape in response to a stimulus. *P Natl Acad Sci USA* **107**, 11205-11210 (2010).
5. Yoo, J.W., Doshi, N. & Mitragotri, S. Adaptive micro and nanoparticles: Temporal control over carrier properties to facilitate drug delivery. *Adv Drug Deliver Rev* **63**, 1247-1256 (2011).
6. Lee, K.J. et al. Spontaneous shape reconfigurations in multicompartmental microcylinders. *P Natl Acad Sci USA* **109**, 16057-16062 (2012).
7. Yoo, J.W., Irvine, D.J., Discher, D.E. & Mitragotri, S. Bio-inspired, bioengineered and biomimetic drug delivery carriers. *Nat Rev Drug Discov* **10**, 521-535 (2011).
8. Sacanna, S. & Pine, D.J. Shape-anisotropic colloids: Building blocks for complex assemblies. *Curr Opin Colloid In* **16**, 96-105 (2011).
9. Chen, Q., Bae, S.C. & Granick, S. Directed self-assembly of a colloidal kagome lattice. *Nature* **469**, 381-384 (2011).
10. Chen, W., Meng, F.H., Cheng, R. & Zhong, Z.Y. pH-Sensitive degradable polymersomes for triggered release of anticancer drugs: A comparative study with micelles. *J Control Release* **142**, 40-46 (2010).
11. Storm, G., Belliot, S.O., Daemen, T. & Lasic, D.D. Surface Modification of Nanoparticles to Oppose Uptake by the Mononuclear Phagocyte System. *Adv Drug Deliver Rev* **17**, 31-48 (1995).
12. Song, L.Y. et al. Characterization of the inhibitory effect of PEG-lipid conjugates on the intracellular delivery of plasmid and antisense DNA mediated by cationic lipid liposomes. *Bba-Biomembranes* **1558**, 1-13 (2002).
13. Hong, R.L. et al. Direct comparison of liposomal doxorubicin with or without polyethylene glycol coating in C-26 tumor-bearing mice: Is surface coating with polyethylene glycol beneficial? *Clin Cancer Res* **5**, 3645-3652 (1999).
14. Klinger, D. et al. A Facile Synthesis of Dynamic, Shape-Changing Polymer Particles. *Angew Chem Int Edit* **53**, 7018-7022 (2014).
15. Kobaku, S.P.R. et al. Wettability Engendered Templated Self-assembly (WETS) for Fabricating Multiphasic Particles. *Acs Applied Materials & Interfaces* **7**, 4075-4080 (2015).

CHAPTER 6

Summary and Future Outlook

6.1. Thesis Summary

My thesis work was focused on designing surfaces with patterned wettability and utilizing the patterned surfaces for different applications. As part of this work, we first developed patterned surfaces that are universal to almost all liquids and then utilized the patterned surfaces for applications like microchannels/microreactors, surfaces for enhanced heat transfer properties, polymer and particle arrays etc. We have also developed a facile fabrication methodology for the fabrication of multi-phasic particles using the patterned surfaces as templates.

The majority of patterned surfaces developed previously exhibit wettability contrast only with high surface tension liquids such as water, thereby limiting the applications of such surfaces mostly to surfactant-free aqueous systems. In order to expand the application range to non-aqueous systems, especially to low surface tension liquids such as oils, alcohols and organic solvents, it is crucial to develop patterned superomniphobic-superomniphilic surfaces. In the first part of my thesis work, we developed a simple, fast and practical methodology to fabricate patterned

superomniphobic-superomniphilic surfaces that exhibit a stark contrast in wettability, for a wide range of polar and non-polar liquids. To fabricate these unique surfaces, we first fabricated superomniphobic surfaces that repel almost all liquids. Next, the superomniphobic surfaces were patterned with superomniphilic domains in desired geometries and dimensions. Using these surfaces, we demonstrated the site-selective self-assembly of a low surface tension liquid like heptane within the patterned superomniphilic domains upon dipping and spraying the liquid. We also demonstrated the site-selective condensation and boiling of different low surface tension liquids, which is crucial when designing surfaces with enhanced phase-change heat-transfer properties. We further demonstrated the site-selective self-assembly of both polymers and microparticles within the patterned domains upon spraying polymer solutions and particle dispersions, respectively.

In the second part of my work, we developed smooth, patterned surfaces that can engender the self-assembly of a wide range of polymer solutions within the patterned wettable domains. Utilizing these patterned surfaces as templates, we developed a novel methodology termed WETS (Wettability Engendered Templated Self-assembly) to fabricate multi-phasic particles of different shapes and sizes. Using the WETS technique, we have fabricated a wide variety of monodisperse, multi-phasic particles in complex shapes, and sizes as small as 25 nm, while maintaining precise control over the thickness, composition, and modulus of each particle phase. We have also fabricated a range of multi-phasic, amphiphilic particles that are anisotropic in both geometry and chemistry, and we have utilized such particles as building blocks for 2-D self-assembled structures. We have further demonstrated the utility of the WETS technique in developing multi-

functional nanoparticles and cargo carriers that are of significant importance in developing drug carriers with controlled release kinetics, increased circulation half-life, and enhanced targeting efficacy.

We also extended the WETS technique to fabricate charged, biocompatible, multi-layered polyelectrolyte (PEL) coated polymeric particles (Polymer-PEL) in different shapes and sizes. Such particles are capable of incorporating a broad range of therapeutics such as small molecule drugs, proteins, and nucleic acids within the polyelectrolyte nanolayers, in addition to the drugs or diagnostic agents encapsulated within the core nanoparticle. Further, PEL assembly on nanoparticle drug carriers can improve the systemic circulation lifetime of the drug carriers, reduce off-target drug delivery, and also allow us to control the cellular internalization kinetics.

In the final part of my work, we have demonstrated stimuli responsive behavior of multi-phasic WETS particles that can dynamically reconfigure their shape, size, and surface composition in response to an increase in temperature of the surrounding medium. As a part of this work, we have also developed mathematical relations that predict the shape-shifted configuration of the multiphasic particles in response to the stimulus.

6.2. Future Outlook and Applications

6.2.1. Multiphasic nanoparticles for drug-delivery

There has recently been significant interest in fabricating nanoparticles for a range of drug-delivery applications.[1-3] These applications stem from the fact that nanoparticles have many advantages as drug carrier over free drugs, including encapsulation, reduced off-target toxicity and targeted delivery (based on the nanoparticles size and shape)[2] and

sustained circulation in the blood stream (as many nanoparticles escape renal clearance).[3] For example, it has been shown that sub 100 nm particles when injected intradermally avoid entrapment within the tissue, and can be efficiently transported to the lymph nodes (critical for generating an immunity response).[4] Further, it has also been shown that the size[3, 5] and shape[3] of the nanoparticles are critical in determining whether a particular particle is able to pass the cell membrane. Thus, for a range of biomedical applications, it is critical to fabricate monodisperse nanoparticles with precisely controlled size, shape, and composition for both the active and passive targeting of cells.[2, 3]

In addition, combinatorial therapy aimed at inducing synergism, would require the encapsulation and release of multiple drugs at diseased sites, ideally with independently controlled release kinetics[6-8]. To address this challenge, nanoparticle drug-carriers should have multiple compartments that can encapsulate and deliver different drugs simultaneously[6-8].

As demonstrated in Chapter 3-5, the WETS technique can be used to fabricate multiphasic nanoparticles from various biocompatible (such as poly lactic-co-glycolic acid and polycaprolactone) polymers in different shapes and sizes. These particles can be encapsulated with various drugs including standard chemotherapeutics (such as Doxorubicin, Fluorouracil, Cisplatin, Topotecan, Gemcitabine), as well as novel cancer stem-cell targeting drugs (BMP2/4 inhibitor Noggin[9], STAT3 inhibitor static[10], metformin[11, 12], repertaxin[13], tocilizumab[14], disulfiram[15], mullerian inhibitory substance[16]). Thus, WETS particles combined with the wide library of drugs available will allow for a systematic study of the behavior of various nanoparticles (including both monophasic and multiphasic particles) as drug carriers, resulting in systematic design

parameters / criteria for ideal drug carriers. These studies may include the test for the effectiveness of nanoparticles in encapsulating various drug molecules, the correlation between design parameters (shape, size and composition) of nanoparticles and drug delivery properties including circulation or sustained release, and the effectiveness in targeting and killing of cancer cells both in vitro and in vivo.

6.2.2. Patterned surfaces for enhanced boiling heat transfer properties

We have shown (Section 2.1.4) that the patterned superomniphobic-superomniphilic surfaces can improve the boiling heat transfer characteristics of a surface with both high and low surface tension liquids[17]. The boiling heat transfer properties of the patterned surfaces are expected to be dependent on the geometry and dimensions of superomniphilic patterns and also on the areal fractions of superomniphobic and superomniphilic regions[18]. So, in order to develop patterned surfaces with optimum boiling heat transfer properties, it is necessary to systematically design different patterned surfaces and study their boiling performance through quantitative measurements. The boiling heat transfer performance is expressed in terms of critical heat flux (CHF) and heat transfer coefficient (HTC) values. The CHF is the highest heat flux that can be exchanged before the nucleated vapor bubbles merge into a continuous vapor film that insulates the surface from the liquid. The HTC is the ratio between the heat flux and the temperature difference between the hot surface and the liquid[19]. In case of the patterned surfaces developed in our work, we expect that the superomniphilic regions would facilitate high CHF values while the superomniphobic regions would facilitate high HTC values. So, the correlation between the design of the patterned surfaces with HTC and

CHF values through quantitative measurements would enable the development of patterned surfaces with optimum boiling heat transfer properties for a given application.

6.3. References

1. Morton, S.W. et al. Scalable Manufacture of Built-to-Order Nanomedicine: Spray-Assisted Layer-by-Layer Functionalization of PRINT Nanoparticles. *Advanced Materials*, **25,** 4707-4713 (2013).
2. Hamidi, M., Azadi, A. & Rafiei, P. Hydrogel nanoparticles in drug delivery. *Advanced Drug Delivery Reviews* **60**, 1638-1649 (2008).
3. Hubbell, J.A. & Chilkoti, A. Nanomaterials for Drug Delivery. *Science* **337**, 303-305 (2012).
4. Baish, J.W. et al. Scaling rules for diffusive drug delivery in tumor and normal tissues. *Proceedings of the National Academy of Sciences* **108**, 1799-1803 (2011).
5. Gao, W., Liu, W., Christensen, T., Zalutsky, M.R. & Chilkoti, A. In situ growth of a PEG-like polymer from the C¬†terminus of an intein fusion protein improves pharmacokinetics and tumor accumulation. *Proceedings of the National Academy of Sciences* **107**, 16432-16437 (2010).
6. Mitragotri, S. & Stayton, P. Organic nanoparticles for drug delivery and imaging. *MRS Bulletin* **39**, 219-223 (2014).
7. Dreaden, E.C. et al. Bimodal Tumor-Targeting from Microenvironment Responsive Hyaluronan Layer-by-Layer (LbL) Nanoparticles. *Acs Nano* **8**, 8374-8382 (2014).
8. Morton, S.W., Poon, Z.Y. & Hammond, P.T. The architecture and biological performance of drug-loaded LbL nanoparticles. *Biomaterials* **34**, 5328-5335 (2013).
9. McLean, K. et al. Human ovarian carcinoma-associated mesenchymal stem cells regulate cancer stem cells and tumorigenesis via altered BMP production. *J Clin Invest* **121**, 3206-3219 (2011).
10. Schust, J., Sperl, B., Hollis, A., Mayer, T.U. & Berg, T. Stattic: a small-molecule inhibitor of STAT3 activation and dimerization. *Chem Biol* **13**, 1235-1242 (2006).
11. Wu, B. et al. Metformin inhibits the development and metastasis of ovarian cancer. *Oncol Rep* (2012).
12. Song, C.W. et al. Metformin kills and radiosensitizes cancer cells and preferentially kills cancer stem cells. *Sci Rep* **2**, 362 (2012).
13. Ginestier, C. et al. CXCR1 blockade selectively targets human breast cancer stem cells in vitro and in xenografts. *J Clin Invest* **120**, 485-497 (2010).

14. Shinriki, S. et al. Humanized anti-interleukin-6 receptor antibody suppresses tumor angiogenesis and in vivo growth of human oral squamous cell carcinoma. *Clin Cancer Res* **15**, 5426-5434 (2009).

15. Yip, N.C. et al. Disulfiram modulated ROS-MAPK and NFkappaB pathways and targeted breast cancer cells with cancer stem cell-like properties. *Br J Cancer* **104**, 1564-1574 (2011).

16. Wei, X. et al. Mullerian inhibiting substance preferentially inhibits stem/progenitors in human ovarian cancer cell lines compared with chemotherapeutics. *Proc Natl Acad Sci U S A* **107**, 18874-18879 (2010).

17. Kobaku, S.P.R., Kota, A.K., Lee, D.H., Mabry, J.M. & Tuteja, A. Patterned Superomniphobic-Superomniphilic Surfaces: Templates for Site-Selective Self-Assembly. *Angewandte Chemie-International Edition* **51**, 10109-10113 (2012).

18. Betz, A.R., Jenkins, J.R., Kim, C.J., Attinger, D. & Ieee in 2011 Ieee 24th International Conference on Micro Electro Mechanical Systems 1193-1196 (Ieee, New York; 2011).

19. Attinger, D. et al. Surface engineering for phase change heat transfer: A review. *MRS Energy & Sustainability - A Review Journal* **1**, null-null (2014).